Relativistic Reflection around Black Holes: Theory and Observation

Relativstische Reflektion in unmittelbarer Nähe Schwarzer Löcher: Theorie und Beobachtung

Der Naturwissenschaftlichen Fakultät
der Friedrich Alexander-Universität
Erlangen-Nürnberg

zur

Erlangung des Doktorgrades Dr. rer. nat.

vorgelegt von

Thomas Dauser
aus Eichstätt

FRIEDRICH-ALEXANDER
UNIVERSITÄT
ERLANGEN-NÜRNBERG
NATURWISSENSCHAFTLICHE
FAKULTÄT

ERLANGEN CENTRE
FOR ASTROPARTICLE
PHYSICS

Als Dissertation genehmigt
von der Naturwissenschaftlichen Fakultät
der Friedrich-Alexander Universität Erlangen-Nürnberg

Tag der mündlichen Prüfung: 22.10.2014

Vorsitzender des Promotionsorgans: Prof. Dr. J. Barth
Gutachter: Prof. Dr. J. Wilms
Prof. Dr. G. Matt

DEUTSCHE ZUSAMMENFASSUNG

Reflektion von Röntgenstrahlung in unmittelbarer Nähe schwarzer Löcher wird stark von relativistischen Effekten beeinflusst. Diese sogenannte “relativstische Reflektion” entsteht, wenn hochenergetische Röntgenphotonen an den innersten Regionen der Akkretionsscheibe reflektiert werden. Parameter des schwarzen Lochs, wie der Spin oder die Emissionsregion der primären Röntgenstrahlung, sind deshalb in der relativistischen Verschmierung des Reflektionsspektrums kodiert. Solche Erscheinungen wurden schon in einigen Quellen beobachtet. Gründliche Studien ermöglichten in einigen Objekten (z.B. NGC 1365) sogar eine zuverlässliche Abschätzung des Spins des schwarzen Lochs. Die meisten dieser Messungen wurden jedoch mit empirischen Modellen durchgeführt, in denen keine physikalisch motivierte Akkretionsgeometrie angenommen wurde. Das Hauptziel dieser Dissertation besteht darin einen physikalischeren Zugang zur Modellierung von relativistischer Reflektion zu untersuchen und ihn auf gemessene Beobachtungsdaten anzuwenden.

Vorherige Beobachtungsergebnisse zeigen, dass die beobachteten Spektren auch erklärt werden können wenn man eine “Lamp Post” Akkretionsgeometrie annimmt. In dieser Geometrie wird die Akkretionsscheibe von einer Quellen bestrahlt, die sich über dem schwarzen Loch auf dessen Rotationssachse befindet. Die Beobachtungen haben außerdem gezeigt, dass die Bestrahlung der Scheibe sehr stark auf die innersten Regionen fokusiert ist. Dies wird in der Lamp Post Geometrie automatisch verhergesagt. Diese Ergebnisse werden als Startpunkt genommen, um ein Modell zu konstruieren, welches die relativistsche Reflektion in der Lamp Post Geometrie verhersagt. Durch die Anwendung dieses Modells auf Spektren des galaktischen schwarzen Lochs Cygnus X-1 und des super-massiven schwarzen Lochs 1H0707−495, kann in dieser Arbeit gezeigt werden, dass die Lamp Post Akkretionsgeometrie konsistente Ergebnisse im Bezug zu vorherigen Veröffentlichungen ergibt. Außerdem ergibt die detailierte Analyse dieser zwei Objekte in beiden Fällen ein schnell rotierendes schwarzes Loch. Diese Ergebnisse stimmen sehr gut mit verherigen Messungen überein. Im Allgemeinen rechtfertigt die Tatsache, dass mehrere Spektren dieser Objekte konsistent mit relativistischer Reflektion beschrieben werden können, außerdem auch die verwendeten Modelle. Es wird gezeigt, dass weiterführende theoretische Untersuchungen der Lamp Post Geometrie zu allgemeinen Aussagen über das System des schwarzen Lochs führen können. Auf der Basis von grundlegenden Beobachtungserkentnissen ist es mir damit möglich direkte Konsequenzen für die Akkretionsgeomtrie abzuleiten. Konkret konnte ich zeigen, dass nur kompakte, primäre Strahlungsquellen, die sich sehr nahe am schwarzen Loch befinden, die beobachteten, stark verbreiterten Emissionslinien erzeugen können. Allerdings bedeutet dieses Ergebnis auch, dass nur der Spin von schnell rotierenden schwarzen Löchern eindeutig durch spektrale Analyse bestimmt werden kann. Ein niedrigerer Spin und eine weiter vom schwarzen Loch entfernte Röntgenquelle erzeugt sehr ähnliche und schmale Emissionslinien, welche mit aktellen Röntgenteleskopen nicht unterschieden werden können. Die Geometrie des Systems kann jedoch auch anderweitig durch die Vermessung des Echos der Röntgenstrahlung bestimmt werden. Dies wurde bereits erfolgreich an einer kleineren Auswahl von Objekten durchgeführt.

Ein großer Teil dieser Dissertation widmet sich der Erstellung eines physiklischeren Modells zur Vorhersage der relativistischen Reflektion. Durch die direkte Verbindung des Reflektionsmodell `xillver` mit dem relativistschen Modell `relline` zum neuen `relxill` Modell wird eine wichtige Verbesserung in Richtung eines physikalischeren Modells vorgestellt. In diesem Ansatz wird zum

ersten Mal in einem relativistischen Modell die Winkelabhängigkeit der reflektierten Strahlung berücksichtigt. Es wird gezeigt, dass dies im Vergleich zu vorherigen Modellen, welche eine winkelgemittelte Reflektion verwenden, einen großen Einfluss auf die Ergebnisse bei der spetralen Analyse hat. Während der Spin zum Beispiel größtenteils unbeinflusst davon ist, zeigen die Simulationen, dass die Eisenhäufigkeit in manchen Quellen um bis zu einem Faktor 2 überschätzt worden sein konnte. Außerdem zeigt die direkte Verwendung des Modells in der Analyse der aktiven Galaxie Ark 120, dass die Unsicherheiten bei der Bestimmung des Spins und der Inklination mit dem neuen Modell signifikant kleiner sind. Zusätzlich wurde der "Reflektionsanteil" als neuer Parameter eingeführt, welcher als der Quotient zwischen dem reflektierten und dem direkt beobachteten Fluss definiert ist. Durch theoretische Überlegungen und unter Verwendung der Lamp Post Akkretionsgeometrie kann für einen gegebenen Spin ein maximaler Wert dieses Reflektionsanteils berechnet werden. Die Anwendung dieser Einschränkung in einer realistischen Simulation zeigt, dass dieses Modell zu einem viel besser bestimmten Wert des Spins führt und gleichzeitig auch unphysikalische Lösungen vermeidet. Besonders die Kombination aus einem niedrigen Spin und einem hohen Reflektionsanteil kann als unphysikalisch angesehen werden, da die Berechnung konkret zeigen, dass nur für einen hohen Spin ($a > 0.6$) ein hoher Reflektionsanteil ($R > 1.5$) erwartet wird. Durch die aufgezeigten Vorteile einer korrekten Behandlung der Winkelabhängigkeit der reflektierten Strahlung und der Berücksichtigung des maximalen Reflektionsanteils, könnte das `relxill` Modell ein neues Standardwerkzeug zur Analyse von relativistischer Reflektion werden. Außerdem wird ein erweitertes physikaliches Modell skizziert, welches selbstkonsistent aus der Bestrahlung den erwarteten Ionisationgradient in der Akkretionsscheibe und das damit verbundene reflektierte Spektrum vorhersagt. Ein solches Modell würde es prinzipiell ermöglichen den Verlauf der Dichte in der Akkretionsscheibe direkt zu bestimmen.

ABSTRACT

Reflection of X-ray radiation that takes place in the immediate vicinity of the black hole is strongly affected by special and general relativistic effects. This so-called "relativistic reflection" is produced when high energetic X-ray photons are reflected at the innermost parts of the accretion disk. Therefore parameters of the black hole system such as the spin of the black hole or the location of the irradiating source of primary X-rays is encoded in the relativistic smearing of these reflection features. Such features have been observed in several objects. Thorough studies also led to reliable estimates of the black hole spin value for some of these objects (e.g., NGC 1365). However, these results were mainly obtained by using empirical models instead of directly using an explicit accretion geometry. The main aim of this thesis is to present a more physical approach to model the relativistic reflection and apply it to observational data.

Previous observational results show that the observed spectra can also be explained by assuming a lamp post accretion geometry, meaning that the accretion disk is irradiated by a source located on the rotational axis of the black hole. The empirical irradiation profile is usually observed to be very steep at the inner parts, which is directly explained by the lamp post geometry. These results are used as a starting point to construct a model, which predicts relativistic reflection in the lamp post geometry. Applying this model to the Galactic black hole binary Cygnus X-1 and the super-massive black hole 1H0707−495, the obtained results presented in this thesis evidently show that the lamp post geometry produces results consistent with previous publications. The detailed analysis of these two objects yields a rapidly spinning black hole in both cases, very well in agreement with previous measurements. Generally, the ability to consistently describe multiple spectra of both objects with relativistic reflection adds further confidence in the chosen approach. Additional theoretical investigations of the lamp post geometry lead to general statements about the black hole system. I find that from basic observational facts implications for the accretion geometry can be drawn. Namely, I could show that only compact irradiating sources that are close to the black hole produce the observed broad reflection features and allow for a reliable spin estimate. However, this result also implies that only the spin of a rapidly rotating black hole can be determined unambiguously by spectral fitting. It is shown that a low spin and a more distant primary source yield very similar, narrow reflection features, which can not be distinguished by current X-ray telescopes. Disentangling the geometry and the spin determination can be done by X-ray reverberation measurement techniques, which have already been successfully applied to a small number of sources.

A major part of this thesis is devoted to construct a more physical model for relativistic reflection. By directly combining the reflection code `xillver` with the relativistic smearing kernel `relline` into the new `relxill` model, an important improvement in physical modeling is presented. By this approach the angular distribution of the reflected radiation is taken into account for the first time. It is shown that this has a major impact on the results obtained by model fitting, compared to the previous approach of using an angle averaged reflection. While parameters such as the spin are found to be insensitive by this, the iron abundance might have been over estimated in some cases by up to a factor of 2. Applying this new model to data of the AGN Ark 120 yields significantly smaller uncertainties than in the angle averaged approach. Additionally, the reflection fraction is introduced as a new model parameter. It depicts the ratio between the flux reflected on the accretion disk and the flux directly reaching infinity. Using theoretical considerations, a max-

imal value of the reflection fraction is calculated by employing the lamp post geometry. Applying this constraint in a realistic simulation shows that this approach leads to a much better estimate of the spin value and also removes unphysical solutions. Especially the combination of a low spin and high reflection fraction is found to be unphysical, as the presented calculations show that only for large spin ($a > 0.6$), a high reflection fraction ($R > 1.5$) is possible. In summary, due to the advantages from the proper treatment of the angular dependence and the constraints emerging from the reflection fraction, the new `relxill` model is prone to be the new standard tool for modeling relativistic reflection. Finally, a sketch of an even more physically motivated model is given, which now includes a self-consistently calculated ionization gradient in the disk. Further indications are given that this method would in principle allow to fit for the density profile of the accretion disk.

CONTENTS

CHAPTER 1

INTRODUCTION TO BLACK HOLE PHYSICS

The general idea of a *black hole* is that of an object where "things" can enter, but never escape. Since Einstein (1905) showed that nothing can be faster than the speed of light, not even light is allowed to escape. By solving the Einstein (1916) field equation for a point mass, Schwarzschild (1916) showed that such objects could in principle exist. Still, strong hints of their existence had not been obtained until Murdin & Webster (1971) and Webster & Murdin (1972) precisely measured the mass of the Cygnus X-1 binary system. Nowadays, several 100000 black holes are known and their existence is generally accepted. As this thesis is mainly concerned about the innermost regions around the black hole, this general view is highly supported by the consistency of the obtained results.

1.1. BLACK HOLES AND ACCRETION

Astrophysical Black Holes exist mainly exist in two different populations. The *Galactic Black Holes* (GBHs) of only a few to tens of solar masses reside in galaxies and are created by Supernova explosions of massive stars. For more details on these objects, the reader may consult the thesis of Hanke (2011) and Fürst (2011) and references therein. *Super-massive black holes* (SMBHs) are found in the centers of galaxies and have masses of $10^{6\cdots9}\,M_\odot$. More information on these objects can also be found in Böck (2012) and Müller (2014) and in the corresponding references. In the greater context with the surrounding material, these objects are also referred to as *Active Galactic Nuclei* (AGN). Both of these type of objects are typically surrounded by an *accretion disk*, a disk built up from in-falling matter (see, e.g., Abramowicz & Fragile, 2013, for a recent review). This matter comes either from a companion star in the case of a GBH or is accreted by the SMBH from surrounding gas of the host galaxy. Moreover, in many of these systems powerful jets of material ejected at relativistic speeds are observed (see, e.g., Perley et al., 1984; Mirabel & Rodríguez, 1994). Figure 1.1 shows artistic renderings of a GBH and an AGN, i.e., both types of objects in which astrophysical black holes are generally found.

Regardless of their mass, black holes are powerful engines causing a huge amount of energy released over the complete electromagnetic spectrum (see, e.g., Krolik, 1999). First of all, the accretion disk heats up, reaching up to 10^8 Kelvin at the inner edge of the disk (see, e.g., Shakura & Sunyaev, 1973). These high temperatures lead to thermal emission of X-ray photons. Hence, a study of the innermost regions around the black hole, which is the aim of this thesis, requires analyzing X-ray spectra. In addition to this thermal contribution, usually at X-ray energies a strong power law component is observed. The origin of this component is not uniquely determined yet, and does not necessarily need to be the same in all objects harboring a black hole. In the most

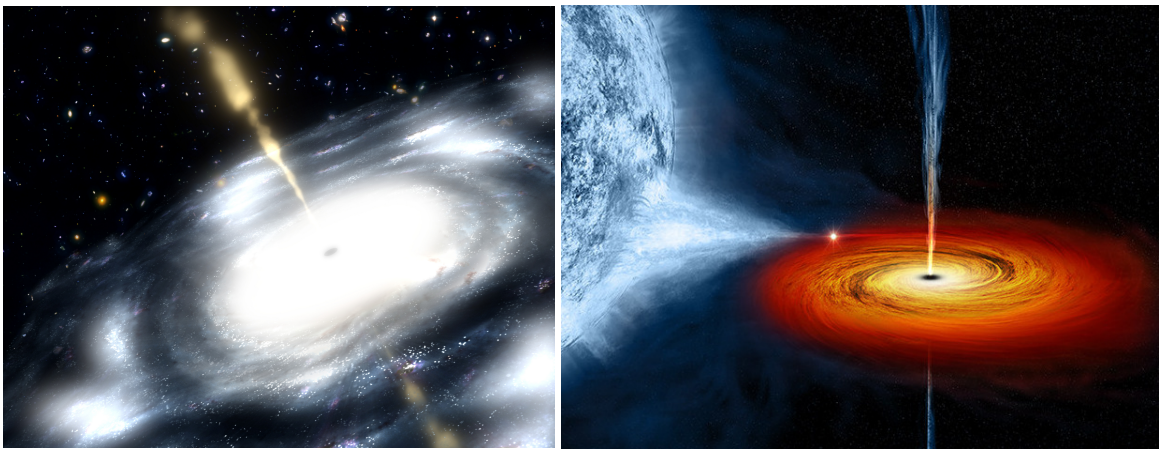

Fig. 1.1.: *Artistic drawings of an Active Galactic Nuclei (left, Credits: NASA/JPL-Caltech) and a Galactic Black Hole fed by its binary companion (right, Credits: NASA/CXC/M.Weiss). Despite a difference of usually more than a million in mass and size, both objects exhibit very similar properties due to the simplicity of the central black hole. In both images, an accretion disk built of in-falling matter forms around the black hole. Along the rotational axis, powerful jets are sometimes ejected.*

simple picture, this component comes from inverse-Compton up-scattering of softer disk photons in a hot corona located above the inner regions of the disk (see, e.g., Shakura & Sunyaev, 1973; Haardt, 1993; Dove et al., 1997). However, self-synchrotron Comptonization from the base of a jet can also explain the observed X-ray spectra (see, e.g., Matt et al., 1992; Markoff et al., 2005). The major differences and possible methods to entangle these geometries is a major part of this thesis and will be treated in much larger detail in Chapter 2. Reynolds & Nowak (2003) present a very detailed review of black holes and accretion, especially focusing on relativistic reflection in such systems.

1.2. Black Holes and their Spin

Certainly the most interesting parameter of the black hole is its spin, which is one of the two parameters that ultimately defines a black hole[1]. The mass can be more easily determined by measuring the motion of objects (see, e.g., Orosz et al., 2011) or by gravitational lensing (see Bartelmann, 2010, for a review). The spin, on the other hand, has only very little direct effect on the motion of more distant particles. Actually, as first noted by Laor (1991), only at the innermost gravitational radii ($r_g = GM/c^2$) differences of the spin become important (see, e.g., Dauser et al., 2010).

But regardless of the challenge of measuring the second parameter defining the black hole, the astrophysical importance of the black hole spin is much larger. Regarding the highly debated formation of powerful jets seen in GBHs and AGN, the spin plays a key role. In many models that try to simulate this formation, mechanisms (e.g., the Blandford & Znajek, 1977, mechanism) connect the jet and its power to the black hole spin. As explained by Garofalo et al. (2010), this connection

[1] Theoretically, a black hole can also have a third parameter, namely a charge. However, the universe is believed to be neutral and therefore astrophysical black holes are not charged (see, e.g., the discussion in Orito & Yoshimura, 1985). In the unlikely event that a black hole would gather a significant amount of charge, it would be quickly neutralized again by vacuum polarization (Reynolds & Nowak, 2003)

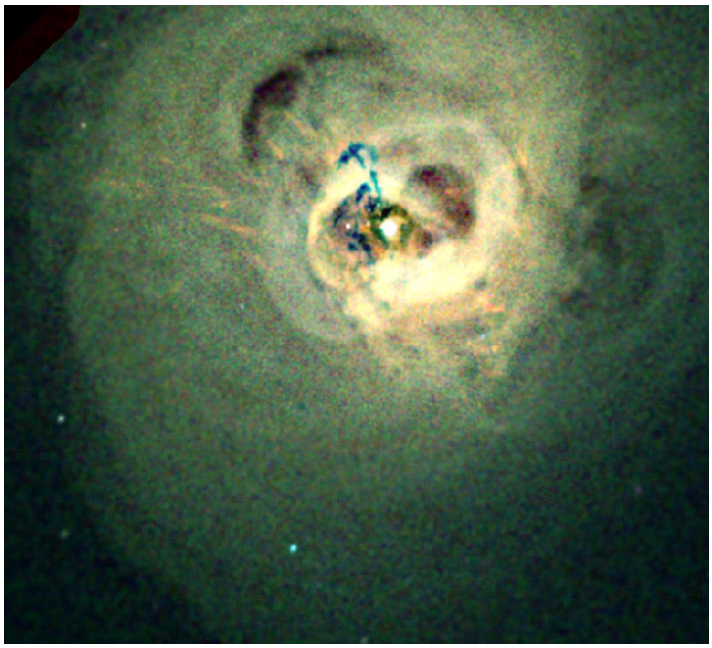

Fig. 1.2: *An image of the Perseus cluster taken with the Chandra X-ray satellite (Fabian et al., 2003). The cavities seen in the cluster, i.e., the black regions in the image, are created by powerful jets along the rotational axis of the black holes. As several cavities of different orientation exist, a merger must have changed the alignment of the black hole's spin.*

triggered a vast amount of studies (see, e.g., Blandford, 1990; Wilson & Colbert, 1995; Moderski et al., 1998, and references therein). The results led to the well known "spin paradigm", meaning that large jet power is associated with rapidly rotating black holes in most models. Contrary to that Garofalo et al. (2010) suggest that the most powerful jets are launched from highly negatively rotating black holes (see also Garofalo, 2009). Knowing simultaneously the jet power and the spin of several objects would yield crucial constraints for jet models.

Despite its much smaller mass, the black hole also plays a key role for the general evolution of galaxies, suggesting that both objects are coupled in their cosmological evolution (see, e.g., Bardeen, 1970; Marconi & Hunt, 2003; Bluck et al., 2011; Kormendy & Ho, 2013). The spin of the black hole is a tracer of the complete evolution process. Its spin is a snapshot, produced by accreting angular momentum over the whole lifetime of the galaxy. Hence, depending on how galaxies form and evolve, we would expect different distributions of spin values. Without much interaction in-between the galaxies, a steady growth is expected. Such an evolution would lead to a continuous spin-up of matter, meaning that this distribution would peak at high spin (see, e.g., Wang et al., 2006). However, more recent observations of cavities in galaxy clusters suggest that mergers of galaxies play an important role for the evolution of galaxies (see, e.g., Fabian et al., 2003, Fig. 1.2). Still, as we only see a snapshot of the evolution the rate and strength of the mergers is unknown. Depending on the actual values of these parameters, galaxy models including mergers predict different distributions of black hole spin in AGN. Frequent and small merger events lead to chaotic accretion, resulting mainly in non-spin black holes as over the time material of very different angular momenta gets accreted (e.g., Hughes & Blandford, 2003; King et al., 2008). However, using different starting values and larger merger sizes, Volonteri et al. (2005) show that a spin-up to maximal spin by mergers is possible as well. In summary, different assumptions on the initial conditions and properties of the mergers produce completely different spin distributions. Knowing only a rough estimate of this distribution would already allow us to distinguish between galaxy evolution models.

1.3. Determining the Spin: Relativistic Reflection from the Accretion Disk

As the hard X-ray source is located very close to the black hole (see Sect. 1.1), distortions originating from relativistic effects are expected (Fabian et al., 1989). Depending on the spin of the black hole, these distortions will transform narrow emission lines to broad, skew-symmetric features. This broadening is only apparent, however, if most of the radiation originates from the innermost regions of the accretion disk (Laor, 1991). Due to a combination of abundances and fluorescent yield, the neutral Fe Kα line at 6.4 keV is typically the strongest fluorescent emission line seen in AGN and GBH spectra. First hints that the fluorescent iron line originates from reflection of X-ray radiation at a dense accretion disk were obtained by Barr et al. (1985) for Cygnus X-1 and in AGN by Nandra et al. (1989) and Pounds et al. (1990). The broadening effect of this iron line due to the vicinity of the reflector to the black hole was already predicted by a number of studies (see, e.g., Fabian et al., 1989; Stella, 1990; Matt et al., 1991, 1992), while the data was still not able to constrain these models (Mushotzky et al., 1993). Note while Fabian et al. (1989) concluded that relativistic effects produced the broad line seen in Cygnus X-1, only first hints of a broad line in AGN were evident at that time. For example Weaver et al. (1992) detected a strong broadening in the iron line region and already noted that "the parameters [...] for the broad component are consistent with its being produced in an accretion disk [...].". Soon the evidence for such a broadening in AGN became more compelling in several objects such as MCG−6-30-15 (Fabian et al., 1994), IC4329A, or NGC 5548 (Mushotzky et al., 1995). Finally, Tanaka et al. (1995) analyzed a long *ASCA* observation of MCG−6-30-15 and concluded that the skew-symmetric broad emission line present in the spectrum originates from reflection only a few gravitational radii away from the central black hole. Further studies have revealed that a large number of AGN (Guainazzi et al., 2006; Nandra et al., 2007; Longinotti et al., 2008; Patrick et al., 2011), such as, e.g., MCG−6-30-15 (Wilms et al., 2001; Fabian & Vaughan, 2003; Marinucci et al., 2014), 1H0707−495 (Fabian et al., 2009; Dauser et al., 2012), or NGC 1365, (Risaliti et al., 2013), Galactic Black Holes , such as Cyg X-1 (Fabian et al., 1989; Duro et al., 2011; Tomsick et al., 2014), GRS 1915+10 (Miller et al., 2013b), or GX 339−4 (Miller et al., 2008; Reis et al., 2008), and neutron stars (e.g., Serpens X-1; Miller et al., 2013a).

From the theoretical side, various models have been proposed to describe the shape of the relativistically smeared features (Fabian et al., 1989; Laor, 1991; Dovčiak et al., 2004; Brenneman & Reynolds, 2006; Dauser et al., 2010). All these models predict the relativistic line profile for a narrow line emitted in the rest frame of the accretion disk. Depending on the parameters of the system, such as for example the spin, the irradiation of the disk, or the inclination to the system the relativistic distortion then leads to different line shapes. Due to the gravitational redshift and the motion of the emitting particles in the disk, these lines are always broadened. Figure 1.3 shows the relativistic line shapes for several combinations of parameters. It is immediately evident that depending on the parameter combinations there is a huge variety of different line shapes. Hence, modeling relativistic reflection has a very large diagnostic potential. Generally, a higher spin leads to broader reflection features, as can be seen in Fig. 1.3c. This is due to the fact that for larger values of spin the accretion disk extends closer to the black hole and therefore more highly redshifted photons from these innermost parts are emitted (see Chapter 2 and Dauser, 2010, for more details). But also other parameters such as the inclination angle or the emissivity profile, which is the irradiating intensity impinging on the disk, lead to significant differences in shape. Therefore, properly measuring the relativistic reflection features allows us to determine a large variety of important parameters of the black hole system at the innermost regions. However, due to this large variety, solely fitting the shape of a single emission line often does not yield a uniquely determined

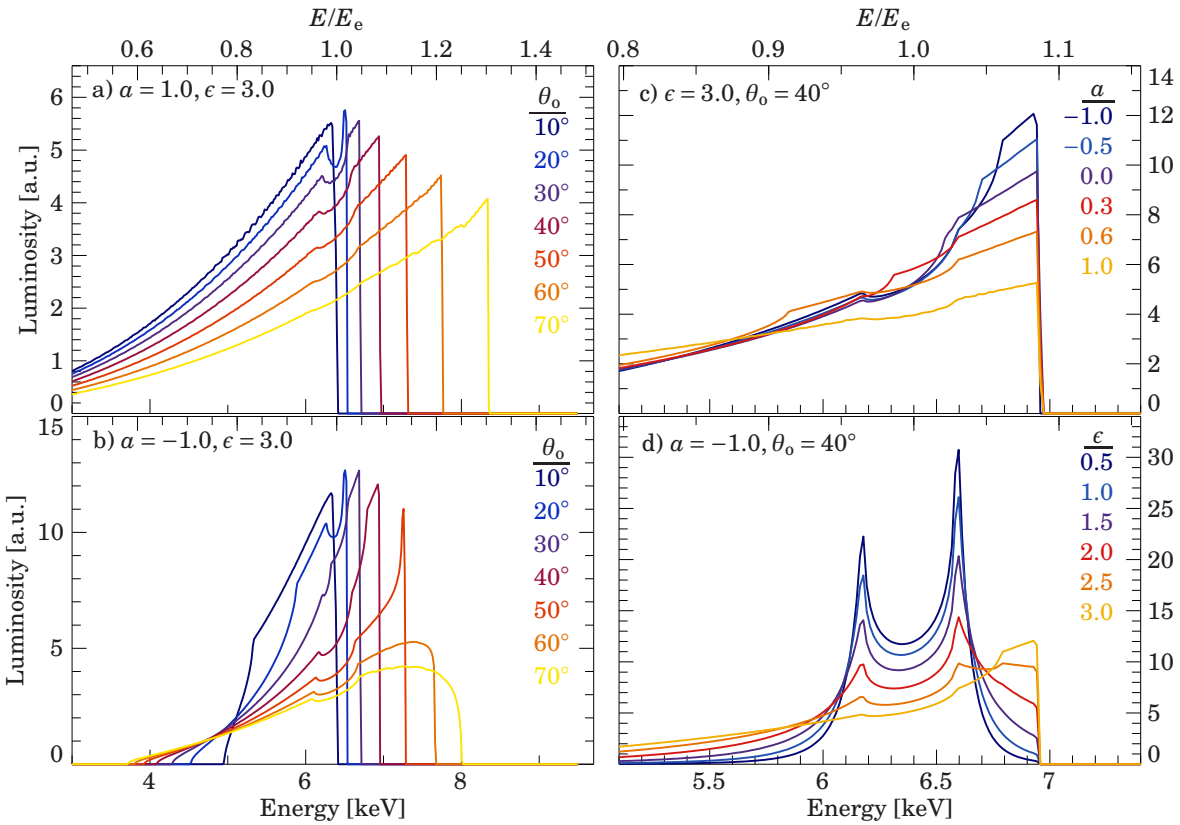

Fig. 1.3.: *Compilation of relativistically broadened lines for different values of spin a, inclination angle θ, and emissivity index ϵ. The latter is connected to the irradiating intensity via $I \propto r^{-\epsilon}$. The presented line shapes are calculated with the* `relline` *model (Dauser et al., 2010).*

set of parameters.

As can be seen in a number of recent publications (see, e.g., Zoghbi et al., 2010; Duro et al., 2011; Fabian et al., 2012b; Dauser et al., 2012; Risaliti et al., 2013), the current quality of X-ray data allows for a more self-consistent approach, which leads to better constrained parameters. It follows the idea of modeling the complete X-ray reflection, taking into account the ionization of the accretion disk with reflection models such as `reflionx` (Ross et al., 1999; Ross & Fabian, 2005; Ross & Fabian, 2007) or `xillver` (García & Kallman, 2010; García et al., 2011, 2013). This reflection spectrum is then relativistically smeared to account for the relativistic effects acting on the complete spectrum. This is generally done by the same models that also predict the single line profiles, which then act as a convolution model. Ideally, data from multiple detectors is used in order to maximize the energy range that is affected by relativistic reflection. This efficiently reduces the ambiguities generally ubiquitous when modeling relativistic reflection, as will be shown in the analysis section in Chapter 3.

Figure 1.4 shows ionized reflection spectra for different ionizations of the accretion disk. The ionization is parametrized by the *ionization parameter* ξ, which is defined as the incident flux F divided by the density of the disk n, namely

$$\xi = \frac{4\pi F}{n} \tag{1.1}$$

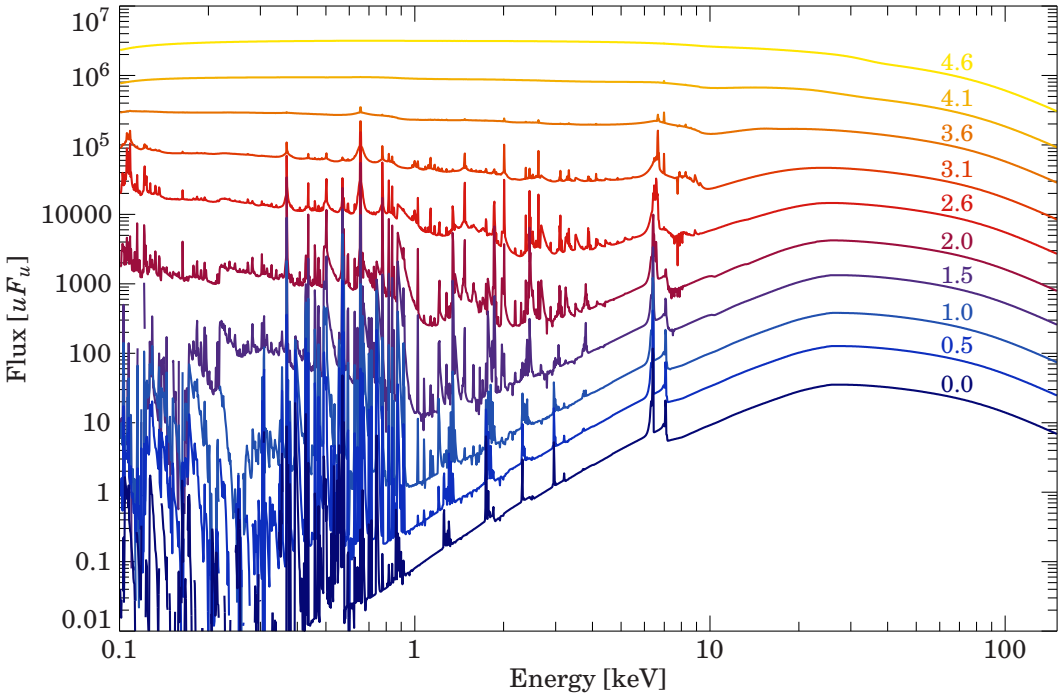

Fig. 1.4.: *Reflection spectra calculated with the* `xillver` *model (García & Kallman, 2010; García et al., 2011, 2013) for different values of the ionization parameter* ξ*, assuming a constant density of the accretion disk (*$n = 10^{-15}\,\mathrm{cm}^{-3}$*). The values in the plots specify* $\log\xi$ *for each curve, from a neutral disk (*$\log\xi = 0$*) to a completely ionized disk (*$\log\xi = 4.6$*). Note that the spectra are not renormalized, but instead the flux scales linearly with the ionization parameter for constant density (see definition in Eq. 1.1).*

(Tarter et al., 1969)[2]. A low value implies that the disk is almost neutral ($\xi \sim 1$). As can be seen in the figure, this leads to a strong Fe Kα line at 6.4 keV and a large forest of emission an absorption lines at lower energies. For increasing ionization parameter, the number and strength of these lines generally decreases, leading to what is called a highly ionized disk for $\xi = 10^3$. For even larger values of ionization ($\xi = 10^4$), the disk is fully ionized. This means that the disk acts almost as a mirror and therefore the spectrum exhibits no line features and the input spectrum is recovered (see García et al., 2013, for a more detailed description). It is notable that the most prominent feature, the iron Kα line at roughly 6.4 keV, strongly changes in shape and flux for different ionizations ξ. Bearing in mind the large variety of line shapes due to the relativistic distortion (Fig. 1.3), a proper modeling of the complete reflection spectrum is therefore essential for a reliable determination of the relativistic parameters. Moreover, it is evident that the general shape of the broader spectrum, e.g., the so-called Compton hump between 20-50 keV, also depends on the ionization. Hence, with a broader covering with X-ray detectors (as has been done, e.g., by Duro et al., 2011; Risaliti et al., 2013) the ionization state of the disk can be determined.

Tab. 1.1.: *Compilation of spin measurements, taken from the review by Reynolds (2013), where sources were selected according to well defined quality standards. References and more detailed information for the single measurements can also be found in this review. The value of NGC 1365 is from Risaliti et al. (2013).*

SMBH name	Spin a
1H0419−577	> 0.89
1H0707−495	> 0.97
Ark120	$0.64^{+0.19}_{-0.11}$
Ark564	$0.96^{+0.01}_{-0.11}$
Fairall 9	$0.52^{+0.19}_{-0.15}$
IRAS 00521−7054	> 0.84
IRAS 13224−3809	> 0.987
RBS1124	> 0.97
MCG−6-30-15	> 0.98
Mrk79	0.7 ± 0.1
Mrk110	> 0.89
Mrk335	$0.83^{+0.09}_{-0.13}$
Mrk359	$0.66^{+0.30}_{-0.54}$
Mrk841	> 0.52
Mrk1018	$0.58^{+0.36}_{-0.74}$
NGC1365	$0.97^{+0.01}_{-0.04}$
NGC3783	> 0.88
NGC4051	> 0.99
Swift J0501.9-3239	> 0.99
Swift J2127.4+5654	0.6 ± 0.2
Tons180	$0.92^{+0.03}_{-0.11}$

GBH name	Spin a
4U 1543–475	0.3 ± 0.1
Cygnus X-1	> 0.95
GX339–4	0.94 ± 0.02
GRS1915+105	> 0.97
GRO J1655–40	> 0.9
LMC X 1	> 0.55
MAXI J1836–194	0.88 ± 0.03
SAX J1711.6–3808	$0.6^{+0.2}_{-0.4}$
Swift J1753.5–0127	$0.76^{+0.11}_{-0.15}$
XTE J1550–564	$0.33 - 0.77$
XTE J1650–500	0.79 ± 0.01
XTE J1652–453	0.45 ± 0.02
XTE J1752–223	0.52 ± 0.11
XTE J1908+094	0.75 ± 0.09

1.4. Current Spin Measurements

In order to be able to answer the important questions about jet formation and galaxy formation mentioned in Sect. 1.2, we would need a reliable sample of spin estimates. Table 1.1 lists reliable spin measurements for GBHs and SMBHs. The measurements are mainly taken from Reynolds (2013), as this selection focuses only on reliable spin estimates. Reliable in this case implies that all fits use a complete, ionized reflection spectrum convolved with a relativistic smearing kernel and that most of the radiation comes from the innermost regions of the accretion disk. Moreover parameters like the iron abundance and the inclination were allowed to vary in all cases (see Reynolds, 2013, for more details). In the case of GBHs, Reynolds (2013) also quotes numerous spin measurements from the continuum method. This method analyzes the relativistic distortion of the thermal accretion disk spectrum in order to estimate the spin (see, e.g., Zhang et al., 1997; Li et al., 2005). However, due to the much lower temperatures of AGN accretion disks, this method is only applicable to GBH systems. In general there is a very good agreement between this method and the reflection method this work focuses on, adding further confidence in the reliability of the

[2] Note that the ionization can also be parametrized differently, e.g., by the parameter U (see, e.g., Krolik et al., 1981; Krolik, 1999).

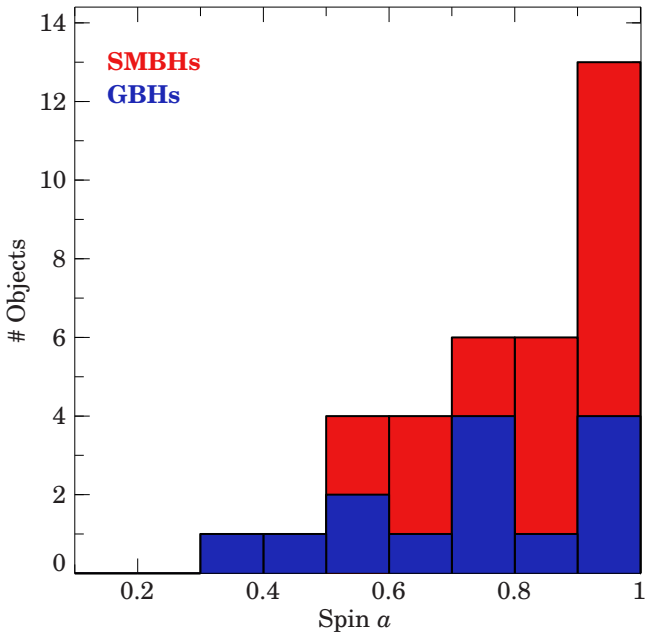

Fig. 1.5: *Visualization of the measured spin values of GBHs and SMBHs displayed in Table 1.1. A strong trend towards rapidly rotating black holes is evident for both objects. This figure is similar to the one displayed in Dauser (2010), however, note the huge improvement in the last years in number and quality of spin measurements.*

measured spin values of GBHs. This compilation is, however, not at all thought to be a complete summary of all measurements fulfilling these criteria, but rather representing the current state of the observations. This selection of reliable spin estimates does not exhibit any negatively rotating black holes, as no data of any object have yet required negative spin to be described. Reliable measurements of spin in GBHs start above values of $a = 0.3$. In the case of SMBHs, no confirmed measurement below $a = 0.5$ is present in our sample. In general, mainly large values of spin were found.

Plotting the values depicted in Table 1.1 in a diagram allows to visualize the current status even better. Figure 1.5 shows the number of sources exhibiting certain spin, separated in GBHs (blue) and SMBHs (red). Clearly, rapidly spinning black holes are measured by far the most often: More than 1/3 of the sources have a spin of $a > 0.9$. Towards lower values of spin, this distribution drops quickly. Taken alone, the GBH distribution is not as peaked towards high spin as the SMBH distribution.[3] However, the absolute numbers in this diagram are too small to allow us to draw any conclusions. In general, however, an interpretation of such a distribution is highly doubtful. First of all, Brenneman et al. (2011) discuss a general observational bias towards detecting higher spin for any flux limited sample. It comes from the fact that in standard accretion disk theory black holes with a higher spin exhibit a larger radiative efficiency and are therefore easier to detect. In general, there are methods to be able to correct for this selection effect, still allowing us to draw conclusions about the actual spin distribution (Brenneman et al., 2011). However, as the spin strongly influences the shape and strength of the relativistic reflection features, large spectral differences arise even for an equal flux of the source. These different effects will be explicitly analyzed in Sect. 2.7.3. Within this thesis I will try to to quantify the apparent biases and caveats, in order be able to analyze how a reliable distribution of spin values, which can be used to interpret and constrain galaxy evolution and jet formation, can be constructed.

[3] Clearly, no equal or similar distribution for GBHs and SMBHs would be expected, as the origin of these objects and their spin is completely different (see Sect. 1.1).

1.5. THE AIM OF THIS THESIS

The current X-ray observatories like *XMM-Newton*, *Chandra*, *Suzaku*, and now also *NuSTAR*, currently provide us with a wealth high resolution X-ray data well suitable for measuring relativistic reflection. Having already established a light-bending code for modeling the relativistic smearing (Dauser, 2010), the ultimate goal of this thesis is to provide a more physical predication of the relativistic reflection and to apply this new model to specifically selected high quality data.

Chapter 2 (Dauser et al., 2013, following) presents the extension of the relativistic reflection model, by including irradiation from the base of the jet, which is motivated from previous observations (Markoff et al., 2005). Instead of assuming an empirical emissivity profile, this geometry is characterized by a physical parameter, namely the height of this source above the black hole. Moreover an analysis of more physical sources of radiation, such as elongated sources or sources moving at high speeds is conducted. Finally the detailed treatment allows to put detailed constraints on the detectability of relativistic reflection depending on the spin and the geometry of the irradiating source. In Chapter 3 this newly built model is then applied to two different objects: Four observations of the Galactic black hole Cygnus X-1 (following Duro et al., 2014) as well as two large observations of 1H0707−495 (following Dauser et al., 2012) are analyzed in detail in order to test the consistency of the interpretation of the data in terms of relativistic reflection and compared to previous observations with different models. Moreover, these data are a good test case in order to see if we are able to constrain the accretion geometry with the new model. Finally, Chapter 4 presents the new `relxill` model. This approach directly combines the most relevant reflection model (`xillver`) with the relativistic model developed previously (Chapter 2). This combination allows for the first time to take into account the angular dependency of the reflected radiation. Section 4.2 (following the work done in García et al., 2014) analyzes the implications for spin measurements arising from this improved and more physical model. Moreover the "reflection fraction", which is the ratio between the reflected and the emitted flux is also a new physical parameter of the `relxill` model. Again, similar to the angular dependence, Sect. 4.3 (following Dauser et al., 2014) studies the implications for measuring the spin and the geometry of the system taking additional, physical constraints from the reflection fraction into account. Finally, the conclusions and the outlook for further studies is given in Chapter 5.

CHAPTER 2

IRRADIATING THE ACCRETION DISK BY A JET

The irradiation of the accretion disk in the jet base geometry and its implications for spin measurements have been thoroughly examined in the Dauser et al. (2013) paper. Therefore this chapter is an extended update of the paper, following it closely and in larger parts in verbatim.

2.1. THE JET BASE GEOMETRY

As already outlined in Sect. 1.3, a primary source of radiation has to exist in order to produce the observed relativistic reflection and also the underlying power law continuum. Initial assumptions were that the primary source consists of a hot corona around the inner regions of the disk, as Comptonization of soft disk photons in such a corona naturally produces a power law spectrum which fits the observations (Haardt, 1993; Dove et al., 1997). Under the assumption that the intensity of the hard radiation scattered back onto the disk by the corona is proportional to the local disk emissivity, the irradiation of the accretion disk would be $I(r) \propto r^{-3}$ for the outer parts, and gradually flatten towards the inner edge of the disk for a standard Shakura & Sunyaev (1973) disk.

With the advent of high signal to noise data from satellites such as *XMM-Newton*, however, measurements showed a disagreement with the Fe Kα line profiles predicted by this coronal geometry. For many sources, the data favored disk emissivities that are much steeper in the inner parts of the accretion disk (see, e.g., Wilms et al., 2001; Miller et al., 2002; Fabian et al., 2002; Fabian et al., 2004, 2012a; Brenneman & Reynolds, 2006; Ponti et al., 2010; Brenneman et al., 2011; Gallo et al., 2011; Dauser et al., 2012; Risaliti et al., 2013). Variability studies of the broad iron lines posed additional problems for standard corona models. In such studies, the time variability of the continuum flux, i.e., the primary hard X-ray radiation, is compared to the flux in the lines, which are produced by the reflected radiation. This approach allows to probe the connection between the primary and the reflected radiation. In a coronal geometry, one expects a positive correlation between the strength of the relativistically distorted reflection spectrum and the primary continuum (Martocchia & Matt, 1996). This is in contrast to what is observed: For example, measurements of MCG−6-30-15 (Fabian & Vaughan, 2003; Miniutti et al., 2003) revealed large variations of the direct radiation, while the reflected component remained constant. Figure 2.1 shows explicitly this example.

As shown by Martocchia et al. (2002), Fabian & Vaughan (2003), Miniutti et al. (2003), and Vaughan & Fabian (2004) for the case of MCG−6-30-15, in a geometry in which the illuminating continuum is assumed to be emitted from a source on the rotational axis at height h above the black hole,

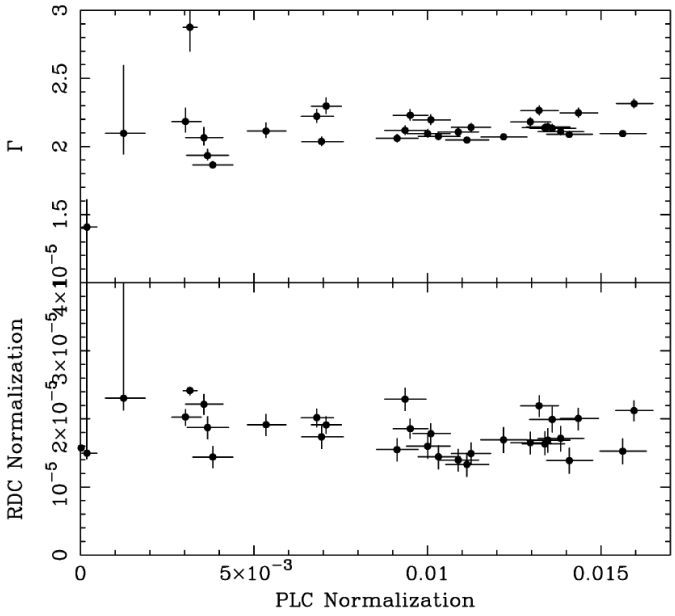

Fig. 2.1: *The photon index (Γ, upper panel) and the reflection strength (RDC, lower panel) plotted for varying primary flux normalization (PLC) in the case of MCG−6-30-15. Note that both parameters are constant, while the direct flux varies by a large amount. This figure is taken from Fabian & Vaughan (2003).*

strong light bending yields properties of the reflected radiation that are consistent with the observations. Such a setup is generally called "lamp post" geometry (Matt et al., 1991; Martocchia & Matt, 1996). In contrast to the standard corona, the primary source is located on the rotational axis of the black hole (see schematic drawing in Fig. 2.2). In general, data and predicted line shapes show very good agreement with the lamp post geometry (see Wilkins & Fabian, 2011; Duro et al., 2011; Dauser et al., 2012). The lamp post model also explains the observed connection between the luminosity and the reflection strength: For a primary source very close to the black hole, most of the photons are focused on the accretion disk, producing a strong reflection component. Therefore less photons are left over to contribute to the continuum component, which is directly emitted towards the observer (Miniutti & Fabian, 2004). For an increasing height of the hard X-ray source this effect gets weaker and thus more photons can escape, which strengthens the continuum radiation and, depending on the flux state of the X-ray source, weakens the reflected flux (Miniutti & Fabian, 2004; Miniutti, 2006). The effect of the lamp post geometry on the ratio in flux between reflected and directed radiation, the so-called "reflection fraction", is investigated in detail in Sect. 4.3.

As a good physical explanation of this hard X-ray source on the rotation axis is the base of a jet (Markoff & Nowak, 2004), we call this geometry also the "jet base geometry". This interpretation is highly supported by the earlier work of Ghisellini et al. (2004), where it is shown that all AGN are capable of forming jets. This is achieved by inventing the concept of "aborted" jets for radio-quite quasars and Seyferts, which are produced when the velocity of the outflowing material is smaller than the escape speed. Such a jet extends only a small distance from the black hole, producing only a negligible amount of radio flux while at the same time it strongly irradiates the inner accretion disk in X-rays, which produces the observed, highly relativistic reflection (Ghisellini et al., 2004). This interpretation is encouraged by works showing that direct and reprocessed emission from such a jet base is equally capable in describing the observed X-ray spectrum as a corona above the accretion disk and also yields a self-consistent explanation of the full radio through X-ray spectrum of many compact sources (Markoff et al., 2005; Maitra et al., 2009). In addition a direct connection between the X-rays and the radio can explain the correlation between observed radio and X-ray

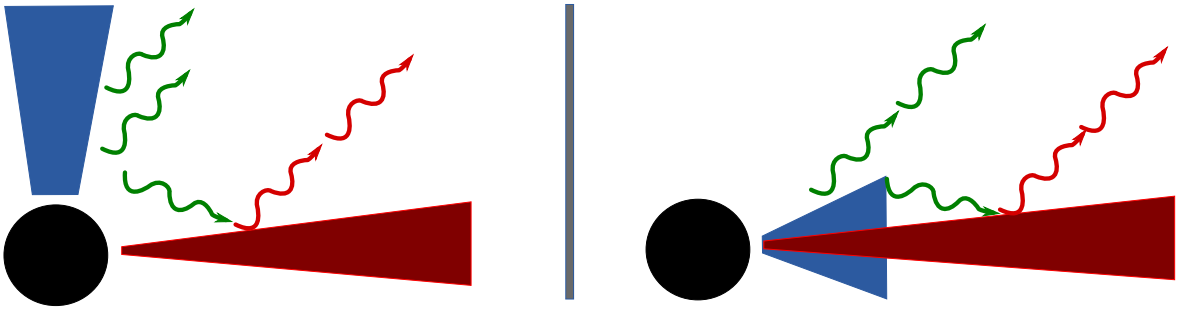

Fig. 2.2.: *A schematic comparison of the different primary sources (blue) causing the observed reflected radiation (red): The lamp post geometry, where the source is located on the rotational axis of the black hole (left) and the standard coronal geometry (right). Part of the primary photons (green) emitted from the primary sources are reflected on the accretion disk (drawn in red).*

flares of Microquasars such as GX 339−4 (Corbel et al., 2000) or Cyg X-1 (Wilms et al., 2007). A similar kind of connection is also indicated in some measurements of AGN like 3C 120 (Marscher et al., 2002) or 3C 111 (Tombesi et al., 2012). Additionally, evidence of a direct influence of the jet on the black hole in Microquasars is growing recently. Namely, Narayan & McClintock (2012) observe a direct correlation between the jet power and the spin value from analyzing a small sample of sources.

2.2. Simulating Spacetime around a Rotating Black Hole

In order to be able to calculate the irradiation of the accretion disk, we need to be able to simulate photon and particle trajectories in the vicinity of a rotating black hole. The so-called *metric* describes spacetime and therefore also ultimately defines these trajectories. As we are concerned about a rotating black hole, i.e., a rotating point mass, we need the proper metric describing this scenario. In case of a rotating black hole, Kerr (1963) showed that it has to be of the form

$$\begin{aligned} \mathrm{d}s^2 = &-\left(1-\frac{2Mr}{\Sigma}\right)\mathrm{d}t^2 - \frac{4aMr\sin^2\theta}{\Sigma}\mathrm{d}t\mathrm{d}\varphi \\ &+\frac{\Sigma}{\Delta}\mathrm{d}r^2 + \Sigma\mathrm{d}\theta^2 + \left(r^2 + a^2\frac{2a^2Mr\sin^2\theta}{\Sigma}\right)\sin^2\theta\mathrm{d}\varphi^2 \quad , \end{aligned} \tag{2.1}$$

where $\Delta = r^2 - 2Mr + a^2$ and $\Sigma = r^2 + a^2\cos^2\theta$. M denotes the black hole mass and $a = J/M$ is the dimensionless spin parameter, defined as the ratio of the angular momentum J and the mass. Note that the metric is given in Boyer & Lindquist (1967) coordinates.

In principle, this definition implies that the spin takes values $0 \le a \le 1$. But as the spin of an astrophysical black hole is defined with respect to the accretion disk, *negatively spinning* black holes are also possible, extending the lower boundary to $a \ge -1$. However, as shown by Thorne (1974), the theoretical maximum value will never be reached, as thermal photons of the accretion disk with opposite angular momentum will be captured by the black hole. Thorne (1974) estimated the upper value to be $a_{\mathrm{max}} = 0.998$, which is also commonly used. Following Dauser et al. (2010), I assume that a retrograde system forms by flipping the accretion disk of a positively spinning system. Hence, the dimensionless spin parameter a of an astrophysical black hole is restricted to $-0.998 \le a \le 0.998$.

In the following all equations are given for $G \equiv M \equiv c \equiv 1$. From solely the metric (Eq. 2.1),

all photon and particle trajectories around the black hole can in principle be calculated. In the following the most important equations are summarized, following closely and in parts verbatim Dauser et al. (2010) and Dauser et al. (2013).[1] Note that a large part of these equations has first been calculated in a great publication by Bardeen et al. (1972). Moreover, Chandrasekhar (1983) extensively treats all possible solutions for trajectories around black holes.

2.2.1. The Equations of Motion

Using the conserved quantities of motion (Carter, 1968), i.e., the energy E, the angular momentum L, the rest mass μ of the particle, and

$$q = p_\theta^2 + \cos^2\theta \left[a^2(\mu^2 - p_t^2) + p_\varphi^2 / \sin^2\theta \right] \quad . \tag{2.2}$$

the general equations of motion are (Bardeen et al., 1972):

$$\Sigma \dot{t} = -a(aE\sin^2\theta - L) + (r^2 + a^2)\frac{T}{\Delta} \tag{2.3}$$

$$\Sigma \dot{r} = \pm\sqrt{V_r} \tag{2.4}$$

$$\Sigma \dot{\theta} = \pm\sqrt{V_\theta} \tag{2.5}$$

$$\Sigma \dot{\varphi} = -\left(aE - \frac{L}{\sin^2\theta} \right) + a\frac{T}{\Delta} \quad , \tag{2.6}$$

where

$$V_r = T^2 - \Delta\left(\mu^2 + r^2 + (L - aE)^2 + q\right), \tag{2.7}$$

$$V_\theta = q - \cos^2\theta\left(L^2/\sin^2\theta + a^2(\mu^2 - E^2)\right) \tag{2.8}$$

and

$$T = E(r^2 + a^2) - aL \quad . \tag{2.9}$$

The signs in Eq. 2.4 and Eq. 2.5 can be chosen independently and account for the direction of the photon. The upper sign means a movement with growing r/θ and the lower sign stands for the opposite behavior, respectively. Thus they can be chosen arbitrarily, but change when a turning point of the trajectory occurs.

2.2.2. The Accretion Disk

In order to describe the accretion disk, which produces relativistic reflection features, it is generally assumed that the disk is geometrically thin and optically thick (Bardeen et al., 1972). From the condition that the disk is stationary ($\dot{\theta} = 0$), located in the equatorial plan ($\theta = \pi/2$), and the requirement that particles orbit the black hole on circles, the accretion disk is only stable down to a certain radius of *marginal stability* r_{ms} (also called the *innermost stable circular orbit*, ISCO). It is given by

$$r_{\mathrm{ms}}(a) = \left(3 + Z_2 - \mathrm{sgn}(a)\sqrt{(3 - Z_1)(3 + Z_1 + 2Z_2)} \right) \quad , \tag{2.10}$$

where

$$Z_1 = 1 + (1 - a^2)^{1/3}\left[(1 + a)^{1/3} + (1 - a)^{1/3} \right] \quad \text{and} \quad Z_2 = \sqrt{3a^2 + Z_1^2} \quad . \tag{2.11}$$

[1] A more detailed derivation can be found in my Diploma thesis (Chap. 2, Dauser, 2010).

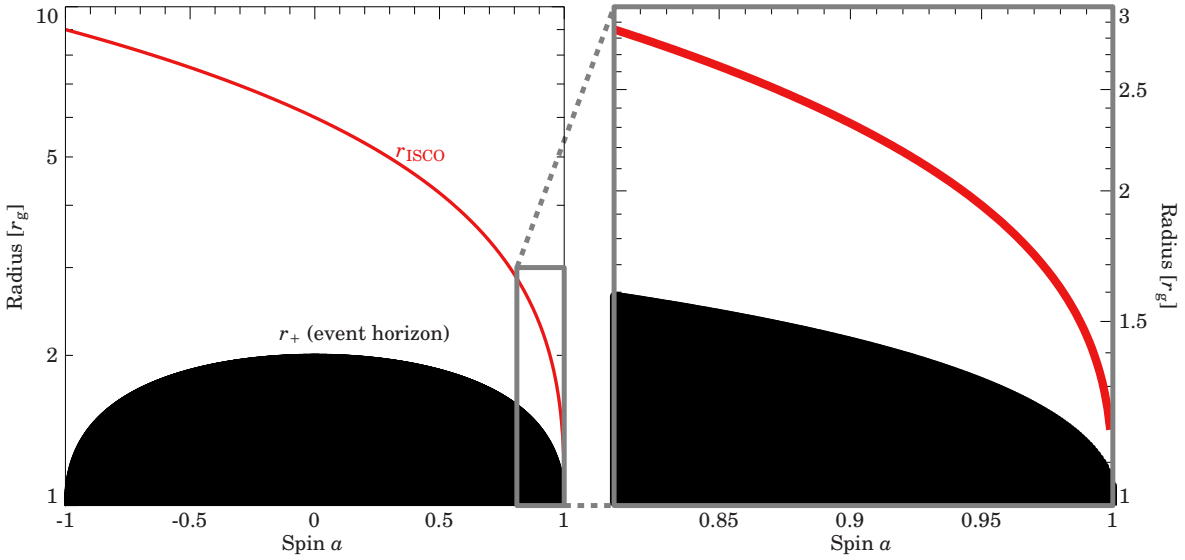

Fig. 2.3.: *The event horizon r_+ and the ISCO for different values of spin. The right panel shows a zoom for large values of spin.*

(Bardeen et al., 1972). Directly from the metric the *event horizon* r_+, which is by definition the size of the black hole, can also be calculated (see, e.g., Carroll, 2004; Dauser, 2010):

$$r_+ = 1 + \sqrt{1 - a^2} \quad . \tag{2.12}$$

The size of the black hole and the ISCO are displayed in Fig. 2.3. Note that in most cases we consider, the ISCO is the inner edge of the accretion disk. That means that the distance between the black and the red line can be directly seen as the gap between the black hole and accretion disk for the objects that are considered in the following. For the highest values of spin this gap becomes very small (see zoom in the right panel of Fig. 2.3).

2.2.3. Photon Trajectories

In order to calculate how a distant observer sees the accretion disk, we need to take general relativistic effects into account. Figure 2.4 shows a simulation of an accretion disk. The distortion originates from the light-bending, which affects photons that are emitted behind the black hole much stronger. Color encoded in the image the energy shift is given, which the photons experience on their way to the observer. The motion of the particles, as calculated in the previous section, is nicely visualized in this image: Due to the Doppler shift photons emitted from the part of the disk approaching the observer are blue-shifted (left part) and red-shifted for the receding part of the disk (right part). Additionally, very close to the black hole strong gravitational redshift strongly affects the emitted photons. In the following, I will briefly review the derivation of the photon trajectories and energy shifts (see Dauser, 2010, for more details). Note that similar calculations have been presented by numerous people (see, e.g., Fabian et al., 1989; Laor, 1991; Dovčiak et al., 2004; Brenneman & Reynolds, 2006).

For photons, i.e., massless particles ($\mu = 0$), the momentum p_μ reduces to

$$p_\mu = E\left(-1, \pm 1/\Delta\sqrt{V_r}, \pm\sqrt{V_\theta}, \lambda\right)^{\rm T} \quad , \tag{2.13}$$

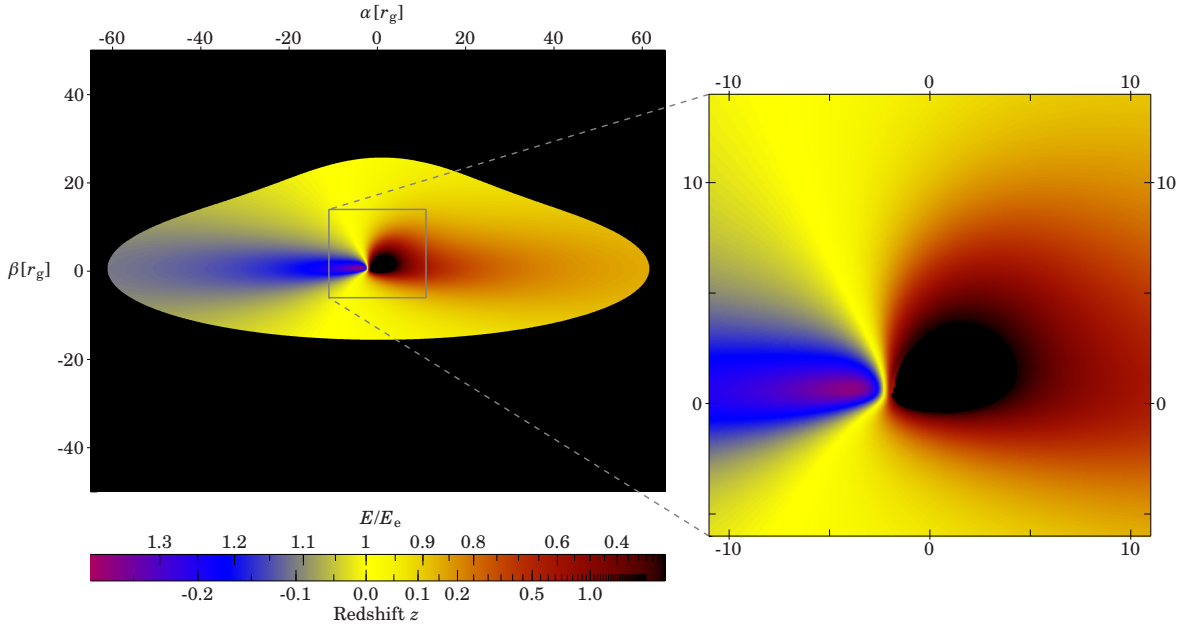

Fig. 2.4.: *Image of an accretion disk observed under an inclination angle of* $\theta = 75°$*.* α *and* β *are sky coordinates, which are defined to be the projection on the sky perpendicular to the line of sight (Cunningham & Bardeen, 1973). Color-encoded is the energy shift the photon experiences from the point of emission in the rest-frame of the disk* (E_e) *to the observer* (E)*.*

where E is the energy of the photon in flat space (see, e.g., Bardeen et al., 1972; Chandrasekhar, 1983; Dauser et al., 2010, for a more detailed derivation). Using the equations of motion (Eq. 2.3-2.6), the general photon trajectory from the point of emission (r_1, θ_1) to the end point (r_2, θ_2) can be calculated by solving

$$\int_{r_1}^{r_2} \frac{\mathrm{d}r}{\sqrt{V_r}} = \int_{\theta_1}^{\theta_2} \frac{\mathrm{d}\theta}{\sqrt{V_\theta}} \quad . \tag{2.14}$$

(Carter, 1968). Note that this equation is only valid for a stationary and axis-symmetric system, which will always be given in the following. Trajectories with turning points are calculated by splitting the integration at these points, taking into account the change in sign in front of $\sqrt{V_r}$ and $\sqrt{V_\theta}$ (see Eq. 2.4 and Eq. 2.5) (see Speith et al., 1995; Dauser et al., 2010).

From the Accretion Disk to the Observer

In this thesis two different kinds of photon trajectories are used. The common relativistic reflection code requires the simulation of trajectories from the emission point r_e on the accretion disk to the observer which sees the system under a certain inclination angle[2] θ. The integration has to be performed from $(r_e, \pi/2)$ to (∞, θ_o) in this case. For all results presented in the following, the numerical code presented in Dauser et al. (2010) was used, which is based on the original code of Speith et al. (1995). I implemented the full functionality of properly predicting the relativistically smeared flux from an accretion disk in the `relline` model code. More details can be found in Dauser et al. (2010) and Dauser (2010).

[2]The inclination angle is the angle under which the system is observed with respect to the normal of the accretion disk.

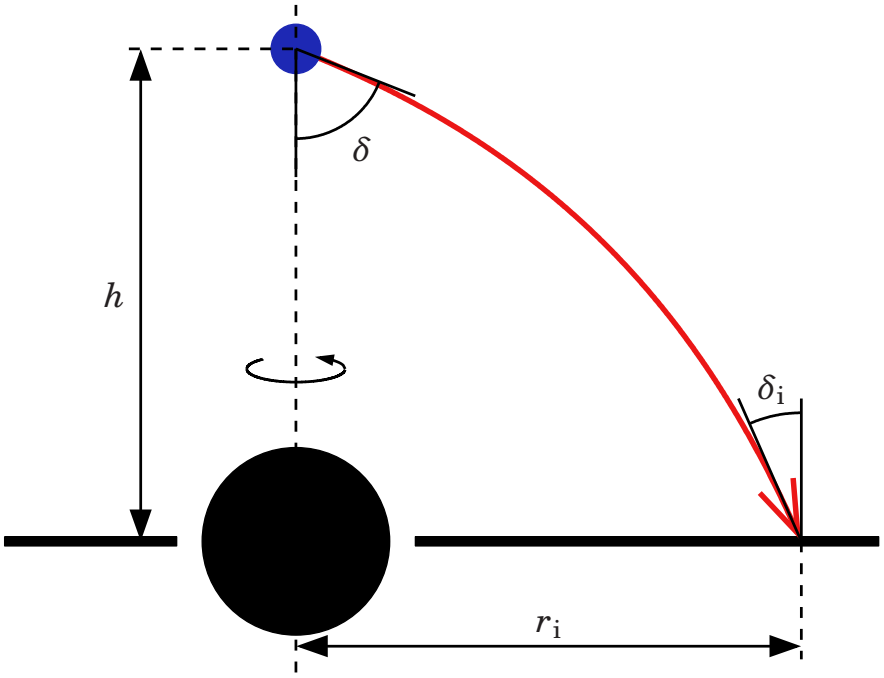

Fig. 2.5: *Schematic drawing of the lamp post geometry. Figure adapted from Dauser et al. (2013).*

From the Lamp Post Source to the Accretion Disk

In the following, a major focus will be put on the irradiation of the accretion disk in the lamp post geometry. A *lamp post* source is defined as a point-like source, which is located directly on the rotational axis of the black hole (Martocchia & Matt, 1996). A schematic drawing is presented in Fig. 2.5. In this case we want to trace photons from the primary source at height h to the incident point on the accretion disk $r_{\rm i}$, i.e., integrating Eq. 2.14 from $(h,0)$ to $(r_{\rm i},\pi/2)$. As has been presented in Dauser et al. (2013), the location on the rotational axis greatly simplifies the integral equation: One can show that p_θ does only take a real value if $\lambda = 0$. Therefore Eq. 2.13 simplifies to

$$p_\mu = E(-1,\ \pm\sqrt{V_r}/\Delta,\ \pm E|q|,\ 0) \quad . \tag{2.15}$$

and the Carter (1968) constant (Eq. 2.2) is directly linked to the the emission angle δ with

$$q = \sin\delta\sqrt{\frac{h^2-2h+a^2}{h^2+a^2}} \quad . \quad . \tag{2.16}$$

Hence, solely by specifying the emission angle δ, the photon trajectory is uniquely defined. The numerical calculation of these trajectories is again based on the Speith et al. (1995) routines, as presented in Dauser et al. (2013).

2.3. Simulating Relativistic Reflection in the Jet Base Geometry

As has been outlined in Sect. 2.1, the difference in relativistic reflection from the jet base geometry to the coronal geometry arises from the different assumptions that are made for the physical processes that are responsible for irradiating the accretion disk. Coronal models (see, e.g., Laor, 1991;

Dovčiak et al., 2004; Brenneman & Reynolds, 2006) assume that the intensity emitted from the accretion disk (the so-called "emissivity") is parametrized as a power law $r^{-\epsilon}$ with index ϵ, where r is the distance to the black hole. The standard behavior is $\epsilon = 3$, which is proportional to the energy release in a standard Shakura & Sunyaev (1973) disk. However, in the jet base geometry we can now exactly predict the irradiation of the accretion disk. By applying the ray-tracing techniques presented in the previous section, we are able to calculate the proper irradiation of the accretion disk by a lamp post source. The radial dependency of this irradiation is equal to the reflected radiation, which was previously modeled by a power law. In the following we will concentrate on a simplified geometry by assuming a point-like, photon emitting primary source at height h above the black hole (see Fig. 2.5). This source irradiates a thin, but optically thick accretion disk, as calculated in Sect. 2.2.2.

Relativistic photon trajectories in the lamp post geometry were first investigated by Matt et al. (1991) and used by Martocchia & Matt (1996) in order to explain the very large equivalent width of the iron Kα line in some AGN. A more detailed discussion of effects in this geometry was presented by Martocchia et al. (2000), including a discussion of the influence of the black hole's spin on the overall spectra. Fukumura & Kazanas (2007) provided a more detailed treatment of the emissivity for arbitrary spin and anisotropic emission of the primary source. Off-axis sources were first investigated by Ruszkowski (2000). Wilkins & Fabian (2012) presented a ray tracing method working on Graphics Processing Units (GPUs), which can calculate irradiation profiles for almost arbitrary geometries of the primary sources, now also including sources extended along and perpendicular to the rotational axis. While the latter approach allows arbitrary primary source geometries, it requires a much larger effort in terms of computational time for calculating the trajectories. Note that in the code presented below, it is assumed that the source is located on the rotational axis of the black hole. This approach is essential to be able to calculate the irradiation for many different parameter combinations, which is necessary to create a model for fitting observational data.

2.3.1. Illumination of the Accretion Disk

In order to calculate the incident intensity on the accretion disk, we first have to consider the geometric effects intrinsic to the lamp post setup. Without any relativistic effects the intensity impinging on the accretion disk for an isotropic primary emitter is given by

$$I_{\mathrm{i}}(r,h) \propto \frac{\cos\delta_{\mathrm{i}}}{r^2+h^2} = \frac{h}{\left(r^2+h^2\right)^{3/2}} \quad . \tag{2.17}$$

This means that already for flat space time the irradiated intensity strongly depends on the radius.

Due to the strong gravity the photon trajectories will be significantly bent, i.e., in our setup the photons will be "focused" onto the inner regions of the accretion disk (Fig. 2.5), modifying the radial intensity profile. Note that this focusing depends on both, the height, h, and the initial direction of the photon, parametrized by the angle between the system's axis of symmetry and the initial direction of the photon, δ.

Using the equations of the previous section I developed a ray-tracing code using similar techniques as those presented in Dauser et al. (2010). As has been motivated in the previous section, this code calculates photon trajectories from the point of emission (h,δ) at the primary source to the accretion disk, yielding the location (r,δ_{i}) where this specific photon hits the disk. Knowing where the isotropically emitted photons hit the accretion disk, we can derive the photon flux incident on its surface. As the photons are designed to be emitted at equally spaced angles δ, the distance Δr between these points is related to the incident intensity. Photons emitted in $[\delta,\delta+\Delta\delta]$

are distributed on a ring on the accretion disk with an area of $A(r,\Delta r)$. The proper area of such a ring at radius r with thickness Δr is given by

$$A(r,\Delta r) = 2\pi r \cdot \sqrt{\frac{r^4 + a^2 r^2 + 2a^2 r}{r^2 - 2r + a^2}}\Delta r \tag{2.18}$$

in the observer's frame of rest (Wilkins & Fabian, 2012). In order to calculate the irradiation in the rest frame of the accretion disk, we have to take into account its rotation at relativistic speed. The area of the ring will therefore be contracted. Using the Keplerian velocity profile deduced from the Kerr metric (Bardeen et al., 1972), the disk's Lorentz factor is

$$\gamma^{(\phi)} = \frac{\sqrt{r^2 - 2r + a^2}(r^{3/2} + a)}{r^{1/4}\sqrt{r\sqrt{r} + 2a - 3\sqrt{r}}\sqrt{r^3 + a^2 r + 2a^2}} \tag{2.19}$$

(Bardeen et al., 1972, see also Wilkins & Fabian 2011, 2012). Taking into account that the photons are emitted at equally spaced angles, we finally find that for isotropic emission the geometric contribution to the incident intensity has to be

$$I_{\mathrm{i}}^{\mathrm{geo}} = \frac{\sin\delta}{A(r,\Delta r)\gamma^{(\phi)}} \quad . \tag{2.20}$$

Because of the relative motion of the emitter and the accretion disk, as well as because of general relativistic effects (e.g., gravitational redshift), the irradiated spectrum will be shifted in energy (Fukumura & Kazanas, 2007). Using the initial four-momentum at the primary source

$$u_{\mathrm{h}}^{\mu} = (u_{\mathrm{h}}^{t}, 0, 0, 0) \tag{2.21}$$

and the corresponding four-momentum on the accretion disk

$$u_{\mathrm{d}}^{\mu} = u_{\mathrm{d}}^{t}(1, 0, 0, \Omega) \tag{2.22}$$

together with the photon's momentum (equation 2.15), the energy shift is

$$g_{\mathrm{lp}} = \frac{E_{\mathrm{i}}}{E_{\mathrm{e}}} = \frac{p_\mu u_{\mathrm{d}}^{\mu}}{p_\nu u_{\mathrm{h}}^{\nu}} = \frac{\left(r_{\mathrm{i}}\sqrt{r_{\mathrm{i}}} + a\right)\sqrt{h^2 - 2h + a^2}}{\sqrt{r_{\mathrm{i}}}\sqrt{r_{\mathrm{i}}^2 - 3r_{\mathrm{i}} + 2a\sqrt{r_{\mathrm{i}}}}\sqrt{h^2 + a^2}} \tag{2.23}$$

The components of the four-velocities are calculated from the normalizing condition $u_\mu u^\mu = -1$ (see, e.g., Bardeen et al., 1972).

As the number of photons is conserved we can write

$$N_{\mathrm{e}}^{(\mathrm{ph})}\Delta t_{\mathrm{e}}\Delta E_{\mathrm{e}} = \text{const.} = N_{\mathrm{i}}^{(\mathrm{ph})}\Delta t_{\mathrm{i}}\Delta E_{\mathrm{i}} \quad , \tag{2.24}$$

where $N_{\mathrm{e}}^{(\mathrm{ph})}$ ($N_{\mathrm{i}}^{(\mathrm{ph})}$) is the emitted (incident) photon flux. Assuming a power law shape of the emitted radiation

$$N_{\mathrm{e}}^{\mathrm{ph}} = E_{\mathrm{e}}^{-\Gamma} \quad , \tag{2.25}$$

the photon flux on the accretion disk is given by

$$N_{\mathrm{i}}^{\mathrm{ph}}(r_{\mathrm{i}}, a) = E_{\mathrm{i}}^{-\Gamma} \cdot g_{\mathrm{lp}}(r_{\mathrm{i}}, a)^{\Gamma} \quad , \tag{2.26}$$

as $\Delta E_e/\Delta E_i = 1/g_{lp}$ and $\Delta t_e/\Delta t_i = g_{lp}$. Due to the relativistic energy shift, the incident photon flux now also depends on where the photon hits the accretion disk (r_i) and which spin the black hole has. Using this result, we can finally calculate the incident flux on the accretion disk

$$F_i(r_i, h) = I_i^{geo} \cdot g_{lp}^{\Gamma} = \frac{\sin\delta\, g_{lp}^{\Gamma}}{A(r, \Delta r)\gamma^{(\phi)}} \quad . \tag{2.27}$$

This is in agreement with the results obtained by Fukumura & Kazanas (2007)[3].

In order to understand the influence of the different relativistic parameters on the incident intensity, Fig. 2.6 shows the single components of equation (2.27). A similar discussion of these components is also given by Wilkins & Fabian (2012). We assume that the primary source is an isotropic emitter. All effects are strongest for small radii and will therefore be most important for high spin, where the accretion disk extends to very low radii. First, length contraction reduces the area of the ring as seen from the primary source. In the rest frame of the accretion disk, this "contraction" implies an effectively larger area and therefore the incident flux decreases with increasing v^{ϕ} proportional to the inverse Lorentz factor $1/\gamma^{(\phi)}$ (Fig. 2.6a). When compared to flat space time, the area of the disk close to the black hole is additionally enhanced in the Kerr metric (Fig. 2.6b). Interestingly, this effect is almost independent of the spin of the black hole[4]. However, compared to the effect induced by the energy shift (equation 2.23), the change in area is only a minor effect. Depending on the power law index, Γ, i.e., the spectral shape of the irradiating photons is the strongest factor influencing the reflection spectrum. For a source on the rotational axis of the black hole the change in irradiated flux can be as large as a factor of 100 (Fig. 2.6c), depending strongly on the steepness of the primary spectrum. This amplification factor depends on the height of the emitting source (it becomes larger for increasing height) and decreases for larger radii. Especially for low h light bending focuses photons towards the disk and additionally enhances the irradiation of the inner regions. The dashed lines in Fig. 2.6d show how $1/\Delta r$ decreases in flat space just due to geometrical reasons following equation (2.17). The fully relativistic treatment (solid lines) reveals a focusing of the photons towards the black hole. But compared to the "effectively enhanced" irradiation of the inner parts due to the energy shift (Fig. 2.6c), the relativistic focusing is only a minor effect. In summary, the power law index, Γ, has the strongest influence on the irradiation profile at small radii, while the height of the emitting source mostly affects the outer parts of the disk.[5]

Finally, Fig. 2.6e combines all effects and shows the incident flux in the rest frame of the accretion disk. In general this plot confirms our overall understanding of the lamp post geometry: Sources at low height strongly irradiate the inner parts but almost not the outer parts. For an increasing height of the source more and more photons hit the outer parts of the accretion disk and an increasing region of more constant irradiation at roughly $h/2$ is created.

In order to check our simulation for consistency, a thorough check against the calculations of Fukumura & Kazanas (2007) was done and we could validate the result from Fig. 2.6e at high precision. The same is true for the stationary point source solution of Wilkins & Fabian (2012). This comparison is shown in Fig. 2.7. In general, especially the right panel reveals that the shape of the emissivity profile is very similar in all simulations. Moreover, all observations are found to converge to r^{-3}, as predicted from the non-relativistic case (Eq. 2.17). Also the steepening at the

[3] Note that Fukumura & Kazanas (2007) use the spectral index α, whereas we use the photon index Γ. Both quantities are related by $\Gamma = \alpha + 1$.

[4] deviations are less than 0.2%

[5] Note that this means that the "focusing" of the photons on the inner parts of the accretion is not responsible for the steep emissivity profile in the lamp post geometry, as is commonly claimed. Rather, it is the strong energy shift due to the deep gravitational potential well and boosting which is responsible for this effect.

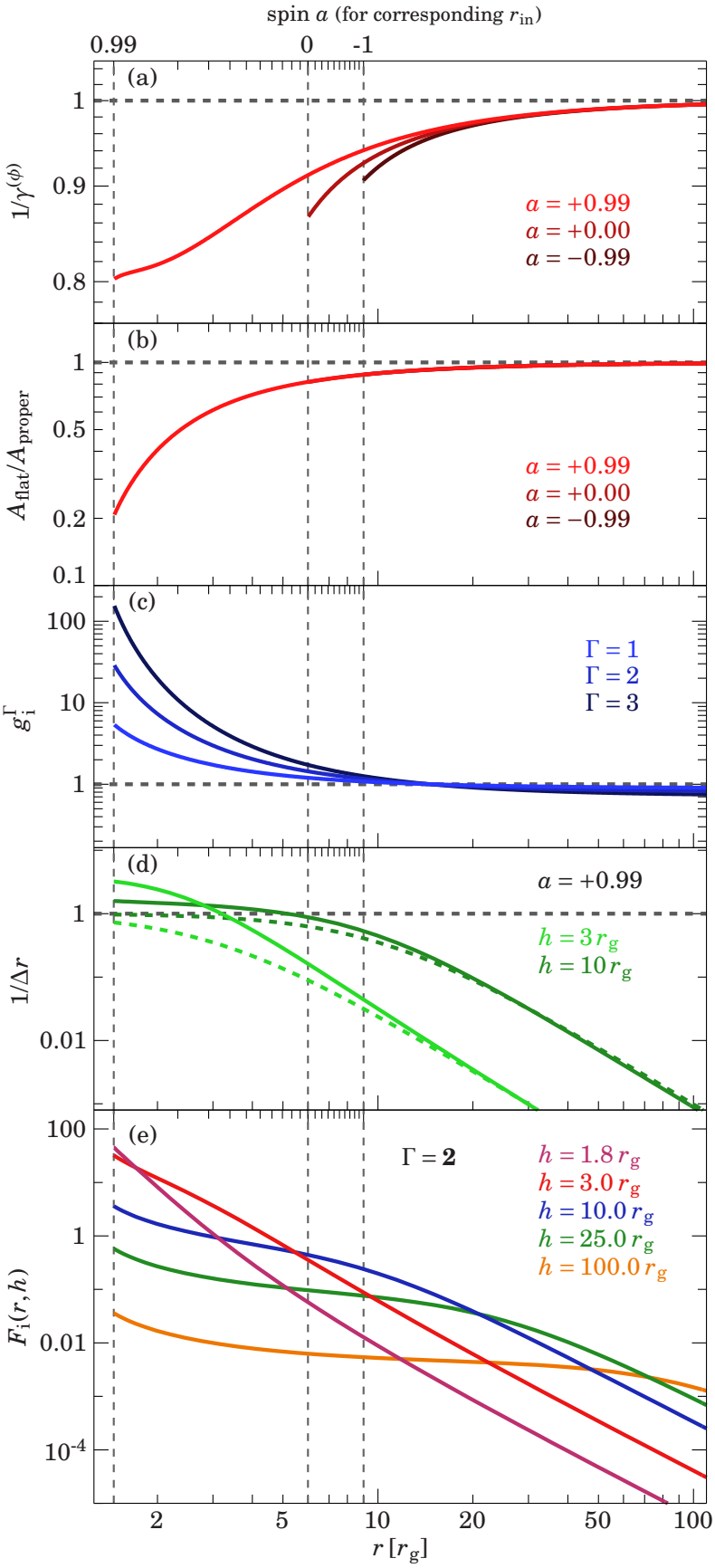

Fig. 2.6: *Relativistic factors which influence the incident flux on the accretion disk compared to the emitted intensity at the primary source (see Eq. 2.27). If not stated in the figure explicitly we use $a = 0.99$ and assume that the primary source is an isotropic emitter. The vertical dashed lines indicate the location of the innermost stable circular orbit (ISCO) for certain values of spin. (a) The inverse beaming factor (red), which determines the influence of length contraction (see equation 2.19) on the incident flux. (b) The impact of the proper area. (c) Geometric intensity distribution on the accretion disk for the relativistic (solid) and Newtonian case (dashed). (d) Energy shift, which the photon experiences when traveling from the primary source to the accretion disk, taken to the power of Γ (blue). (e) Combined irradiating flux on the accretion disk for a primary source at different heights but equal luminosity. Figure taken from Dauser et al. (2013).*

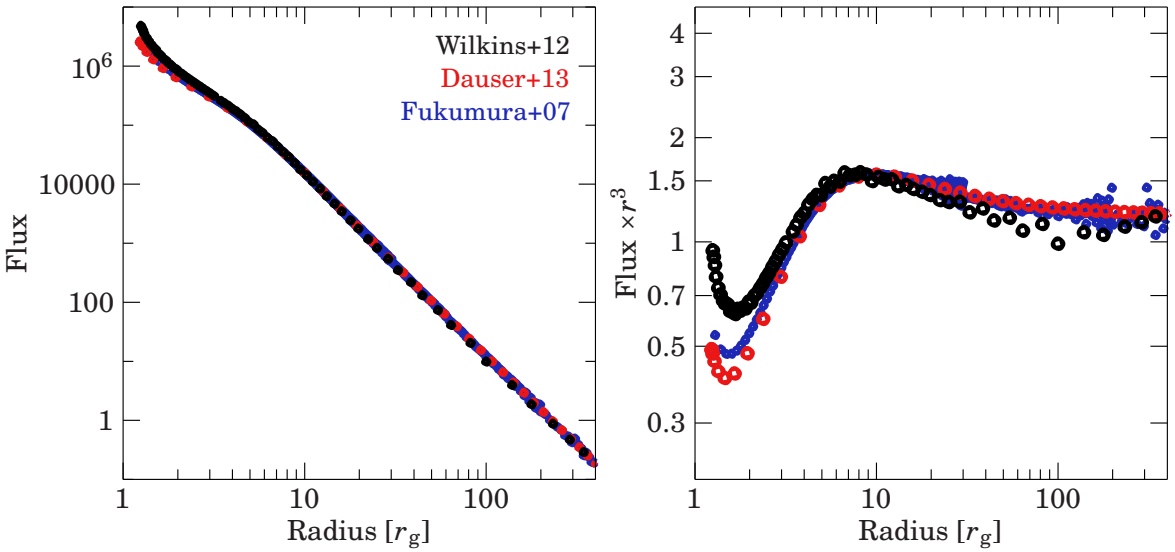

Fig. 2.7.: *Comparison of the emissivity profiles for different numerical simulations: Wilkins & Fabian (2012) (black), Fukumura & Kazanas (2007) (blue), and the code presented here (red, Dauser et al., 2013). In the right panel the flux is multiplied by a factor of r^3, visualizing the differences much better as the flux should be $\propto r^{-3}$ for large r. The source height was assumed to be $h = 5r_g$, and the spin $a = 0.998$.*

innermost radii, i.e., the slope of the curves, is very similar. However, while the simulation presented here (Dauser et al., 2013) is always in good agreement with Fukumura & Kazanas (2007), the simulation of Wilkins & Fabian (2012) differs by a larger amount for lower radii. Finally, the precision of the new lamp post code can also be nicely visualized in this comparison: While both other codes show numerical scattering in the predicted flux for larger radii, no such features are visible in the case of the Dauser et al. (2013) code. And note that the time required to calculate this smooth line is only a fraction of the computation time of the other codes, especially compared to the computationally very expensive code of Wilkins & Fabian (2012).

2.4. Emissivity Profiles in the Lamp Post Geometry

Since for a simple accretion disk the local disk emissivity is roughly $\propto r^{-3}$, in the description of observations it is common to parametrize the disk emissivity profile through

$$F(r,h) \propto r^{-\epsilon} \tag{2.28}$$

where ϵ is called the emissivity index. Note that in this representation the information of the normalization of the emissivity profile is lost. But as usually the luminosity of the irradiating source is not known, this is not important for reflection studies. The presented calculations easily allow to determine the radius dependent emissivity index and thus phrase our results in a language that is directly comparable with observations.

Figure 2.8 shows the emissivity profile for different heights of the primary source. Regardless of the specific height, three different radial zones are visible in all profiles. Firstly, for large radii the index converges always towards its value in flat space ($\epsilon = 3$, see equation 2.17). The closer the emitting source is to the black hole, the faster ϵ converges towards this value.

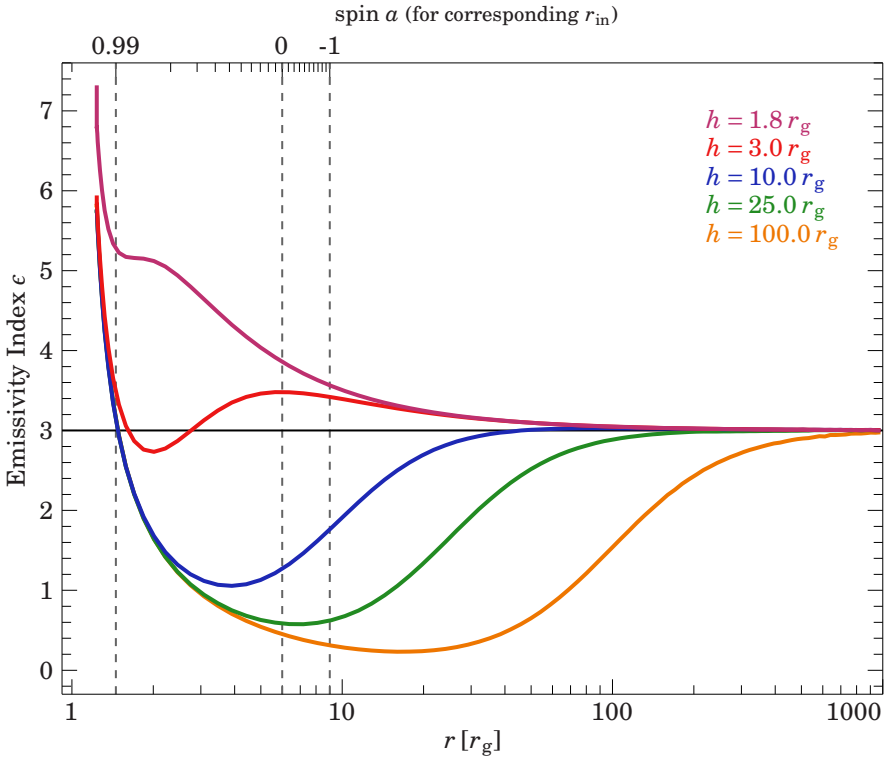

Fig. 2.8: *The emissivity index ϵ as defined in equation (2.28) of the radiation irradiating the accretion disk from a primary source at different heights h. Figure adapted from Dauser et al. (2013).*

The region closer than $2r_g$ from the black hole is characterized by a strong steepening of the emissivity profile towards the inner edge of the accretion disk. Except for an extremely low height, this steepening is almost independent of the height of the primary source[6]. A large emissivity at low radii, which is usually interpreted as "strong focusing of a low height emitter", is not directly related to the height of the primary source. Instead, the steepness almost solely depends on the relativistic boosting of the primary photons and especially on the steepness Γ of the primary spectrum (see Fig. 2.6c).

As has been mentioned in the introduction (Sect. 2.1), many sources are observed to have very steep emissivity indices, i.e., values of $\epsilon = 5$–10 are normal. Similar to the emissivity profile in Fig. 2.8, we can also derive the maximal possible emissivity index for a certain value of spin and steepness of the input spectrum. For a standard lamp post source at a height of at least $3r_g$, this information is plotted in Fig. 2.9. In this case, no large emissivities are expected if the black hole is not a maximal rotator, i.e., roughly for $a < 0.9$. If the input spectrum is hard ($\Gamma < 2.5$), the emissivity index is flatter than the standard index of $\epsilon = 3$. Even for highly rotating black holes the actual emissivity at the inner edge of the accretion disk is only steep if the incident spectrum is very soft ($\Gamma > 2.5$).

If we want to apply the information of Fig. 2.9 to a certain observation, we have to take into account that the emissivity is generally parametrized in form of a broken power law. In detail this means that below a certain "break radius" (r_{br}) one single emissivity index is used to describe the steep emissivity and above that it is usually fixed to the canonical r^{-3} behavior. Generally, break radii are found to be in the range of $3\,r_g$ (e.g., in 1H0707−495, Dauser et al., 2012) up to $6\,r_g$ (e.g., in NGC 3783, Brenneman et al., 2011)[7]. Hence, the emissivity index we measure in observations

[6] Clearly, the absolute flux for a certain luminosity is highest for a low emitter (see Fig. 2.6e), but we usually do not measure the absolute intensity, but only the emissivity index.

[7] Note that the value of the break radius is highly correlated with the emissivity index when trying to constrain both by

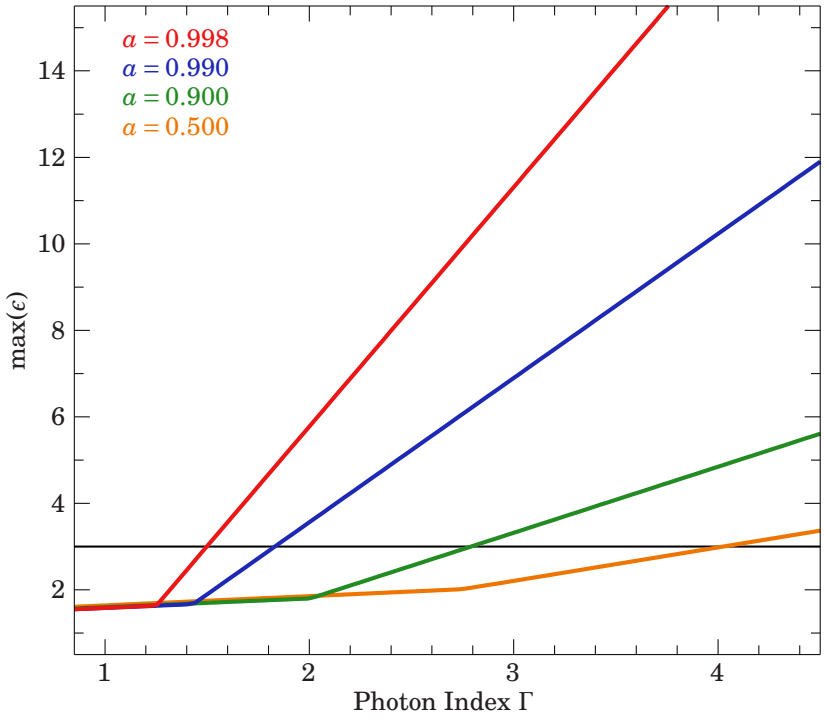

Fig. 2.9: *The maximum possible emissivity index at the inner regions of the disk ($r < 10r_g$) for a certain photon index Γ. The height of the source was chosen to be $h = 10r_g$. However, note that we showed in Fig. 2.8 that for $h > 3r_g$ the steepening at the inner edge of the disk is almost independent of the height. Figure taken from Dauser et al. (2013).*

accounts for the average steepness in the range of r_{in} to r_{br} and will therefore be lower than the maximal emissivity. Note that the emissivity indices found in many observations are close to or above the maximal allowed emissivity index as defined in Fig. 2.9. For example $\epsilon \approx 5$ for $\Gamma = 1.8$ in NGC 3783 (Brenneman et al., 2011), $\epsilon \approx 6$ for $\Gamma = 2$ in MCG−6-30-13 (Brenneman & Reynolds, 2006), $\epsilon > 6.8$ for $\Gamma = 1.37$ in Cygnus X-1 (Fabian et al., 2012a), or $\epsilon \approx 10$ for $\Gamma = 3.3$ in 1H0707−495 (Dauser et al., 2012). As the emissivity index obtained from these measurements is averaged over the innermost few r_g these emissivities can therefore not be properly explained solely by the lamp post geometry. Despite these issues, however, in some cases it is possible to use Fig. 2.9 to decide if a measured value for the emissivity index can reasonably be explained in the lamp post geometry. This method has been successfully applied by Duro et al. (2014) to find a unique and consistent solution to describe the reflection spectrum of Cygnus X-1 (see also Sect. 3.2).

2.5. The incident angle

The incident angle δ_i of the irradiated radiation is important for modeling the reflected spectrum, as it determines the typical interaction depth of the reflected photon and therefore strongly influences the limb-darkening of the reflected radiation (e.g., Svoboda et al., 2009). Constructing a normal vector on the disk, δ_i is given by

$$\cos\delta_i = \frac{p_\perp}{|p|} = \frac{(p_d)_\mu \left(n_d^{(\theta)}\right)^\mu}{(p_d)_\nu (u_d)^\nu}\bigg|_{\theta=\pi/2} = \frac{q}{r_i u_d^t(r_i, a)} \quad . \tag{2.29}$$

Figures 2.10a and b show δ_i for different heights of the primary source and assuming an isotropic primary emitter. For most disk radii the photons hit the disk at a shallow angle, except for a small

observation.

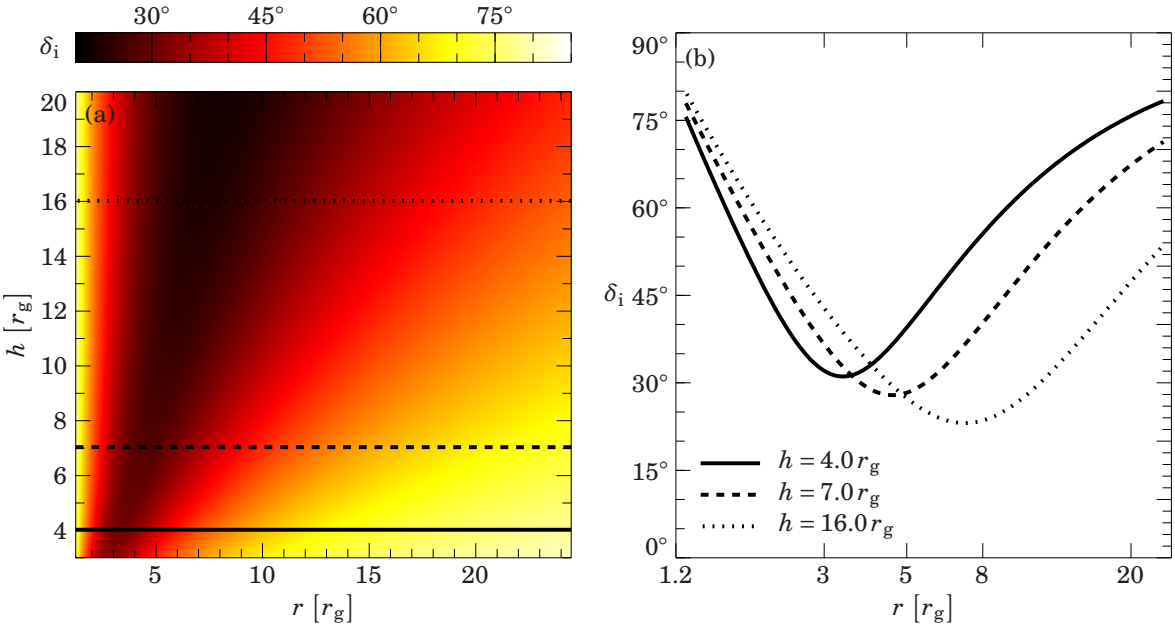

Fig. 2.10.: *(a) 2D image showing the incident angle δ_i of photons on the accretion disk. The spin of the black hole is $a = 0.998$. (b) incident angle for the three lines (solid, dashed, dotted) marked in subfigure (a). Figure adapted from Dauser et al. (2013).*

fraction of disk. The location and width of the steeper in-falling photons depend on the height of the primary source.

The effect of the incidence angle of the illumination in the reflected spectrum from an accretion disk has been discussed by García & Kallman (2010). In the calculation of reflection models, the boundary at the surface of the disk is defined by specifying the intensity of the radiation field that illuminates the atmosphere at a particular angle. Using their Eq. 19 and Eq. 37, this can be expressed as

$$I_{\mathrm{inc}} = \left(\frac{2n}{4\pi}\right)\frac{\xi}{\cos\delta_i}, \tag{2.30}$$

where n is the gas density (usually held fixed), and ξ is the ionization parameter that characterizes a particular reflection model (see Eq. 1.1 and Tarter et al., 1969). Consequently, for a given ionization parameter, varying the incidence angle varies the intensity of the radiation incident at the surface. This has interesting effects on the ionization balance calculations. If the photons reach the disk at an angle perpendicular to the disk's surface ($\delta_i = 0$), the intensity has its minimum value, but the radiation can penetrate into deeper regions of the atmosphere producing more heating. In contrast, for grazing incidence ($\delta_i = 90$) I_{inc} increases, resulting in a hotter atmosphere near the surface; but the radiation field thermalizes at smaller optical depths, which yields lower temperature in the deeper regions of the disk. Evidently, these changes in the ionization structure will also affect the shape and flux of the reflected spectrum (see Fig. 2.11). The narrow component of the emission lines are expected to be emitted relatively near the surface, where photons can easily escape without being absorbed or scattered. On the other hand, the broad component of the emission lines, and in particular the ones from high Z elements such as iron, are produced at larger optical depths ($\tau \sim 1$), and therefore are more likely to be affected by changes in the ionization structure of the slab.

However, García & Kallman (2010) showed that in a general sense, reflected spectra resulting

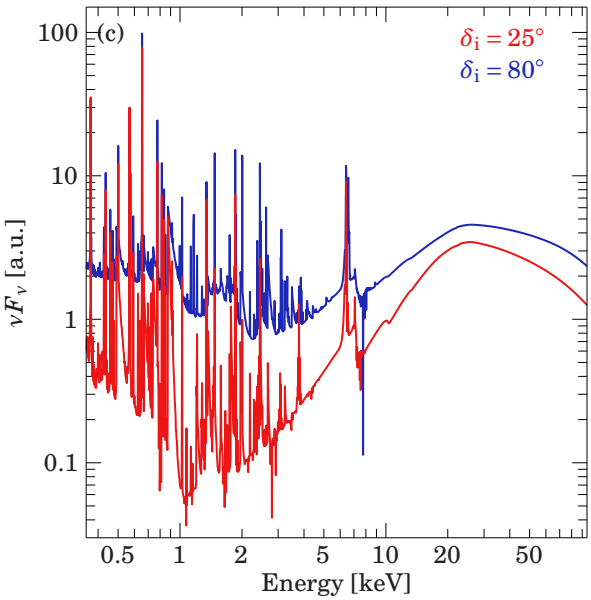

Fig. 2.11: *Sample reflection spectra for different incident angles $\delta_i = 25°$ (red) and 80° (blue) calculated with the* XILLVER *code (García & Kallman, 2010; García et al., 2011). Figure taken from Dauser et al. (2013).*

from models with large incidence angles tend to resemble models with higher illumination. This means that the changes introduced by the incidence angle can be mimicked by correcting the ionization parameter to account for the difference introduced in the illumination. The current analysis shows that below $7r_g$ the incidence angle can vary as much as $25-80$ degrees, equivalent to a change in the ionization parameter by more than a factor of 5. Figure 2.11 shows the reflected spectra for these two incidence angles predicted by the XILLVER code (García & Kallman, 2010; García et al., 2011) using the same ionization parameter. The effect of the incidence angle is evident.

2.6. An extended Ray-Tracing Code

So far we assumed that the emitting primary source is at rest with respect to the black hole. If the primary emitter is the base of the jet, however, then it is far more likely that the primary source is moving. Typical speeds at the jet base can already be relativistic (McKinney, 2006). Furthermore, if the irradiating source is a jet, then we need to relax our assumption of a point-like emitter and include the radial extent of the jet. As shown in the following section by taking into account both of these extensions, the line shape is significantly affected.

2.6.1. A Moving Jet Base

First investigations of a moving source irradiating the accretion disk and its implication for the Fe Kα were done by Reynolds & Fabian (1997). Beloborodov (1999) investigated the coupling between the moving primary source and the reflected radiation. Using general relativistic ray tracing techniques, Fukumura & Kazanas (2007) and Wilkins & Fabian (2012) calculated the illumination profile on the accretion disk.

It is assumed that the emitting primary point source is moving at a constant velocity $\beta = v/c$. The most prominent effect of a moving jet base compared to a jet base at rest is the Doppler boosting of radiation in the direction of the moving blob, i.e., away from the accretion disk. This boosting also means that the energy shift of the photon between primary source and accretion disk changes

with velocity. The 4-velocity is then given by

$$u_{\mathrm{h}}^{\mu} = u_{\mathrm{h}}^{t}\left(1, \frac{\mathrm{d}r}{\mathrm{d}t}, 0, 0\right) \tag{2.31}$$

The velocity β as seen by an observer at the same location in the locally non-rotating frame (LNRF) is connected to $\mathrm{d}r/\mathrm{d}t$ through

$$\beta = \frac{e_{\mu}^{(r)} u_{\mathrm{h}}^{\mu}}{e_{\nu}^{(t)} u_{\mathrm{h}}^{\nu}} = \frac{r^2 + a^2}{\Delta} \cdot \frac{\mathrm{d}r}{\mathrm{d}t} \quad , \tag{2.32}$$

where $e_{\mu}^{(\nu)}$ are the tetrad basis vectors for $\nu = t, r, \theta, \phi$ (see Bardeen et al., 1972).

In order to calculate the trajectory of a photon emitted at an angle δ' from the moving source, we transform from the moving frame to the stationary, locally non-rotating frame at the same location. This means that the photon is emitted at an angle δ in the stationary system according to

$$\cos\delta = \frac{\cos\delta' - \beta}{1 - \beta\cos\delta'} \quad , \tag{2.33}$$

depending on the velocity of the source. Following, e.g., Krolik (1999), it can be easily shown that this approach implies that the intensity observed in the stationary frame will be altered by a factor of

$$\mathscr{D}^2 \quad , \tag{2.34}$$

where $\mathscr{D}$ is the special relativistic Doppler factor, which is defined in our case as

$$\mathscr{D} = \frac{1}{\gamma(1 + \beta\cos\delta)} \quad , \tag{2.35}$$

with $\gamma = 1/\sqrt{1-\beta^2}$ being the Lorentz factor of the moving source. Using the transformed intensity, we can now can apply the stationary calculations from Sect. 2.3.1 to the new emission angle δ to obtain the irradiation of the accretion disk by a moving source.

Additionally, we have to calculate the proper energy shift between the accretion disk and the moving source, with the 4-velocity given by equation (2.31). Similarly to equation (2.23) this energy shift is given by

$$g_{\mathrm{lp}} = \frac{(p_{\mathrm{d}})_{\mu} u_{\mathrm{d}}^{\mu}}{(p_{\mathrm{h}})_{\nu} u_{\mathrm{h}}^{\nu}} = \frac{g_{\mathrm{lp}}(\beta = 0)}{\gamma\left(1 \mp \frac{\sqrt{(h^2+a^2)^2 - \Delta(q^2+a^2)}}{h^2+a^2}\beta\right)} \, . \tag{2.36}$$

Note that for large heights g_{lp} simplifies to its special relativistic limit, $g_{\mathrm{lp}} = \mathscr{D}\, g_{\mathrm{lp}}(\beta = 0)$. Using the results we already obtained for a stationary primary source (see Sect. 2.3.1), we can finally write down the total flux the accretion disk sees from a moving source:

$$F_{\mathrm{i}}(r_{\mathrm{i}}, h, \beta) = \frac{\mathscr{D}^2 F_{\mathrm{i}}(r_{\mathrm{i}}, h, \beta = 0)}{\left[\gamma\left(1 \mp \frac{\sqrt{(h^2+a^2)^2 - \Delta(q^2+a^2)}}{h^2+a^2}\beta\right)\right]^{\Gamma}} \quad . \tag{2.37}$$

Figure 2.12 shows the dependency of the emissivity index on the velocity of the jet base. In general the irradiating flux decreases significantly with increasing speed of the jet base, as the photons are boosted away from the black hole (Fig. 2.12a).

Comparing the shape of the emissivity profiles for a moving jet base (Fig. 2.12b), the intermediate region of the accretion disk (3–100r_{g}) experiences an increase of irradiation with increasing velocity of the jet base. On the other hand the emissivity profile of the very inner regions of the

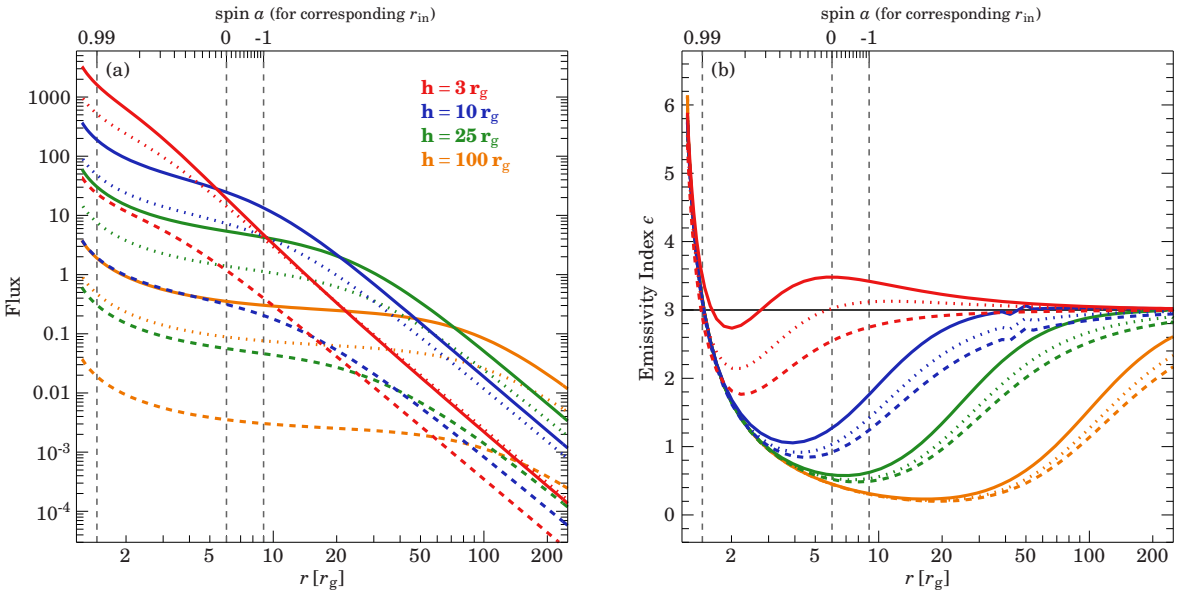

Fig. 2.12.: *(a) Irradiating flux and (b) Emissivity profiles similar to Fig. 2.8, which show the impact of a moving jet base with velocities $v = 0\,c$ (solid), $v = 0.5\,c$ (dotted), and $v = 0.9\,c$ (dashed). Figure taken from Dauser et al. (2013).*

accretion disk does not depend on the movement of the jet. For high spin ($a > 0.9$) the accretion disk extends down to these very small radii and due to the steep emissivity most of the reflected radiation comes from there. If the accretion disk only extends down to $6r_g$, as is the case for $a = 0$, the irradiation of the innermost regions can differ almost up to a factor of 2 in emissivity index depending on the velocity of the jet base.

2.6.2. Irradiation by an Elongated Jet

It is straightforward to extend the previous discussion of a moving jet base to the the case of an extended jet (see also Wilkins & Fabian, 2012). We simply describe the incident radiation for an elongated jet by many emitting points at different heights, weighted by the distance between these points. Emissivity profiles for the extended jet are shown in Fig. 2.13. In general, the shape of the emissivity profile in the case of an extended source does not differ significantly from that of a point-like source. Similar to the moving jet base (see Sect. 2.6.1), the irradiation of the inner regions of the accretion disk ($r < 2r_g$) only differs in normalization but not in shape (Fig. 2.13). However, the regions of the disk that are a little bit further outwards ($> 3r_g$) are affected at a much greater fraction by extending the emission region. But despite these large differences, the overall shape of the emissivity profile does not change, i.e., that the general properties analyzed in Sect. 2.4 are still valid in the case of elongated jets.

The influence of changing the location of the jet base while fixing the top height is depicted in Fig. 2.13a,b. Interestingly the emissivity profile is not very sensitive to the location of the jet base. On the other hand, fixing the jet base at a low value ($3r_g$) and then increasing the radial extent of the jet (Fig. 2.13c) strongly alters the emissivity profile. The more the top is away from the base, the larger the deviations become compared to the profile of the jet base (red, dashed line) and the more the irradiation resembles the one from the upper part of the jet. Comparing the extended profiles to the ones for a point-like primary source (dashed lines) reveals that the

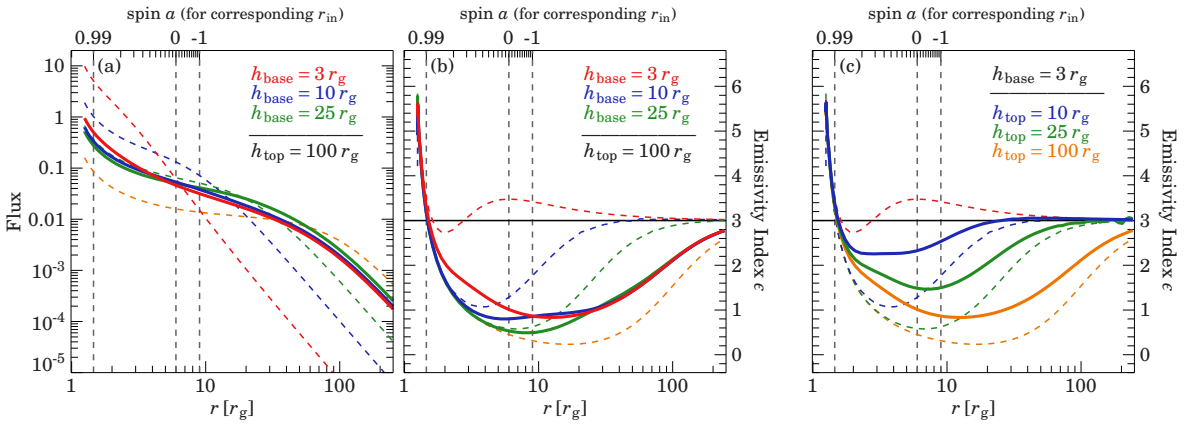

Fig. 2.13.: *Emissivity profiles similar to Fig. 2.8, which show the impact of an elongated jet compared to a point source. For comparison the dashed lines show the emissivity of a point-like emitting source with same colors as in Fig. 2.8, i.e., red, blue, green, and orange for $3r_g$, $10r_g$, $25r_g$, and $100r_g$, respectively. For varying the base of the emitting region the irradiating flux (a) and the emissivity profile (b) is shown. In (c) the top height of the jet is altered. Figure taken from Dauser et al. (2013).*

extended emission creates an irradiation pattern that could have similarly been produced by a point source at an intermediate height in between $h_{\rm base}$ and $h_{\rm top}$, too. This implies that if we measure an emissivity profile similar to one for a low source height (Fig. 2.13, dashed red line), the jet cannot be extended or there is no significant amount of radiation from the upper parts irradiating the disk. One way to explain the lack of photons is that the jet does not have a uniform velocity, but the jet base is at rest and from there on the particles are very efficiently accelerated (see McKinney, 2006) such that the radiation is beamed away from the accretion disk.

2.6.3. Jet with Constant Acceleration

Having analyzed the effect of a moving primary source and the profile of an extended jet, we are able to combine these effects to form a more realistic approach. It is likely that the actual base of the jet is stationary or has at least a velocity normal to the disk plane that is much less than the speed of light. Above the jet base the particles are efficiently accelerated (McKinney, 2006) to higher energies and in the end to very fast velocities seen, e.g., in Very Long Baseline Interferometry (VLBI) measurements (see, e.g., Cohen et al., 2007). In the following we will assume the simplest case by using a constant acceleration $\mathscr{A}$ of the particles. In this case the velocity evolves as (see, e.g., Torres Del Castillo & Pérez Sánchez, 2006)

$$\beta(t) = \frac{\mathscr{A}\, t}{\sqrt{c^2 + \mathscr{A}^2 t^2}} \quad , \tag{2.38}$$

where the time t is given by

$$t = \sqrt{\frac{x^2}{c^2} + 2\frac{x}{\mathscr{A}}} \tag{2.39}$$

for $x = h - h_{\rm base}$. Therefore the acceleration to reach a specific velocity β at height h is given by

$$\mathscr{A} = \frac{\gamma - 1}{h - h_{\rm base}} \quad , \tag{2.40}$$

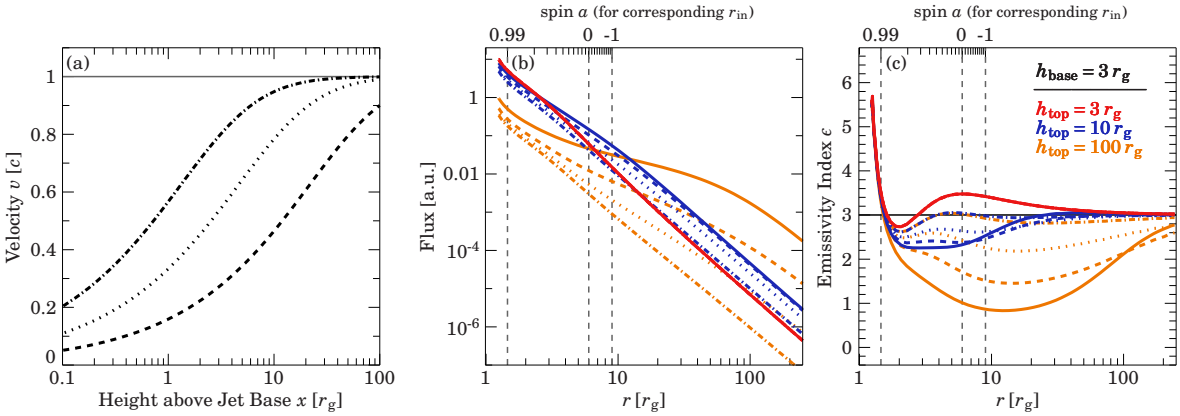

Fig. 2.14.: *(a) Velocity of the jet assuming a constant acceleration and the jet base at rest. The spin of the black hole is $a = 0.998$, and the power law index $\Gamma = 2$. The acceleration is parametrized by specifying the velocity v_{100} the jet has at $100\,r_g$ above the jet base. Lines are plotted for $v_{100} = 0.9\,c$ (dashed), $v_{100} = 0.99\,c$ (dotted), and $v_{100} = 0.999\,c$ (dashed-dotted). (b) and (c) Emissivity profiles for an extended jet with the constant acceleration shown in (a). Parameters are the same as in a). The solid line displays the emissivity profile for a stationary jet. Despite the different heights, each jet is assumed to have an equal luminosity. Figure taken from Dauser et al. (2013).*

where γ is the Lorentz factor. Figure 2.14a displays the velocity (equation 2.38) inside the jet for constant acceleration.

The irradiation of the accretion disk in this setup is shown in Fig. 2.14b. The effect of the accelerated movement shows up at larger radii by steepening the emissivity compared to the stationary jet and for all heights the profile gets more similar to a point source at the jet base. This result confirms the general picture that for a large acceleration the accretion disk sees only the lowest part of the jet, as most photons from of the upper part of the jet are strongly beamed away from the disk. This means that if we measure a localized, low height of the emitting source, it could also be the base of a strongly accelerating jet. Additionally, Fig. 2.14c reveals that the stronger the acceleration, the more the emissivity profiles resembles the canonical r^{-3} case for all but the innermost radii ($r > 2r_g$).

2.7. Application of the extended Lamp Post Calculations

2.7.1. relline_lp — a relativistic lamp post model

Using the approach mentioned in Sect. 2.3.1, the lamp post geometry was incorporated in the relline model (Dauser et al., 2010). This model was designed to be used with common data analysis tools such as xspec (Arnaud, 1996) or isis (Houck & Denicola, 2000) for modeling relativistic reflection. It can either predict a single line shape or it can be used as a convolution model smearing a complete reflection spectrum predicted by, e.g., the `reflionx` (Ross & Fabian, 2007) or `xillver` (García & Kallman, 2010) model. See Appendix A for a detailed description of the model and its parameters.

The calculations in the lamp post geometry are used to determine the proper irradiation profile and replace the artificial broken power law emissivity in the `relline` model. Besides the standard

point source in the lamp post geometry, we also included the extended geometries presented in Sect. 2.6, i.e., elongated and moving primary sources. As the information of the ray tracing is tabulated, the `relline_lp` model is evaluated very quickly and thus well suited for data modeling.

2.7.2. Influence of the lamp post parameters on the shape of the reflection features

With the `relline_lp` model it is possible to calculate the predicted line shapes of broad emission lines for the different parameters determining the setup in the lamp post geometry. Figure 2.15 shows that the line shape is very sensitive for certain parameter combinations and almost independent in other cases.

The line shape is highly sensitive to a change in height of the primary source (Fig. 2.15a and b). Especially when assuming a rapidly rotating black hole, the line shape dramatically changes from a really broad and red-shifted line to a narrow and double-peaked structure when increasing the height of the source (Fig. 2.15a). The same behavior can be observed for a negatively rotating black hole (Fig. 2.15b), but here differences are not as large as in the previous case. Broad lines seen from a configuration of a low primary source and a highly rotating black hole are also sensitive to the photon index Γ of the incident spectrum (Fig. 2.15c). In this case the line shape gets broader for a softer incident spectrum. When fixing the height of the irradiating source (Fig. 2.15d–f), for a low source height the shape is still sensitive to the spin (Fig. 2.15d). But already for a medium height of $25r_g$the line shapes virtually coincide for all possible values of black hole spin. In this case, even for a rapidly rotating black hole, the line shape does not depend on the steepness of incident spectrum (Fig. 2.15f).

Using the `relline_lp`-code, we are also able to compare line shapes for moving (Sect. 2.6.1), elongated (Sect. 2.6.2), and accelerating (Sect. 2.6.3) primary sources. A change in velocity only alters the line shape if the source is at low height and the black hole is rapidly rotating (Fig. 2.15g). Changing either of these to negatively rotating (Fig. 2.15h) or a larger source height (Fig. 2.15i), different velocities of the irradiating source only have a marginal effect on the line shape. Similarly, measuring the radial extent of the primary source is also not possible for all parameter combinations. Firstly, the restrictions of measuring a and Γ for larger heights, as seen in Fig. 2.15e and f, also apply here. Therefore we fix these two values at $a = 0.99$ and $\Gamma = 2.0$. Setting the base of the source at $3r_g$ and altering its height (Fig. 2.15j) does indeed result in great changes in the line shape. These changes are very similar to a change in height of a point-like primary source (see Fig. 2.15a). An elongated jet produces a reflection feature similar to a point-like source with an effective height. A similar behavior can be observed when changing the base of the primary source and leave the upper boundary constant at $100r_g$. However, as the large upper part now dominates the irradiation of the accretion disk, the profile is not very sensitive to the location of the base of the source. Finally, an accelerating jet (Fig. 2.15l) only influences the line shape if already relatively high velocities are obtained at a height of $100r_g$ ($v_{100} > 0.99c$), as in the upper part of the jet more and more photons are beamed away from the accretion disk due to the highly relativistic movement of the emitting medium. The line profiles for a strong acceleration thus resemble very closely the ones for a lower top of the emitting source (Fig. 2.15j), which means that in reality we will not be able to measure if the emitting source is accelerating without knowing the full geometry of such a primary source.

In some sources with a low mass accretion rate, the disk might be truncated further away from the black hole than the ISCO (see Esin et al. 1997 and, e.g., the observations by Markowitz & Reeves 2009; Svoboda et al. 2010). Generally, relativistic emission lines from such truncated disks are even narrower than for non or negatively spinning black holes. However, such lines can also

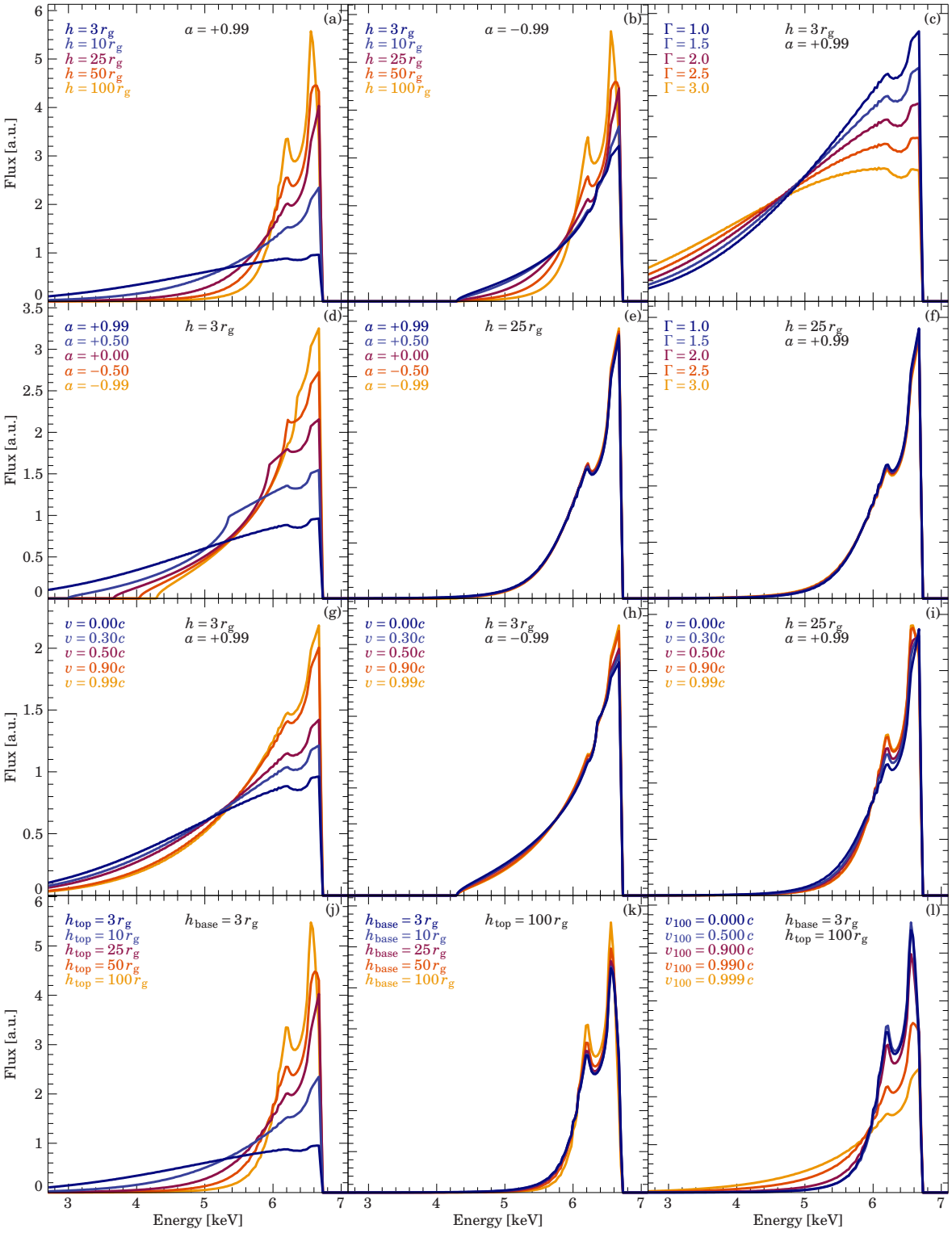

Fig. 2.15.: *Line Profiles of the* `relline_lp` *model for different parameters. If not stated differently we assume* $a = 0.99$ *and* $h = 3\,r_g$*. We fix the inclination at* $i = 30°$ *and the outer edge of the disk at* $r_{out} = 400 r_g$*. Note that we always assume that the inner edge of the accretion disk coincides with the ISCO. All profiles are normalized to have equal area, i.e., the number of photons producing each reflection feature is equal. This figure is taken from Dauser et al. (2013).*

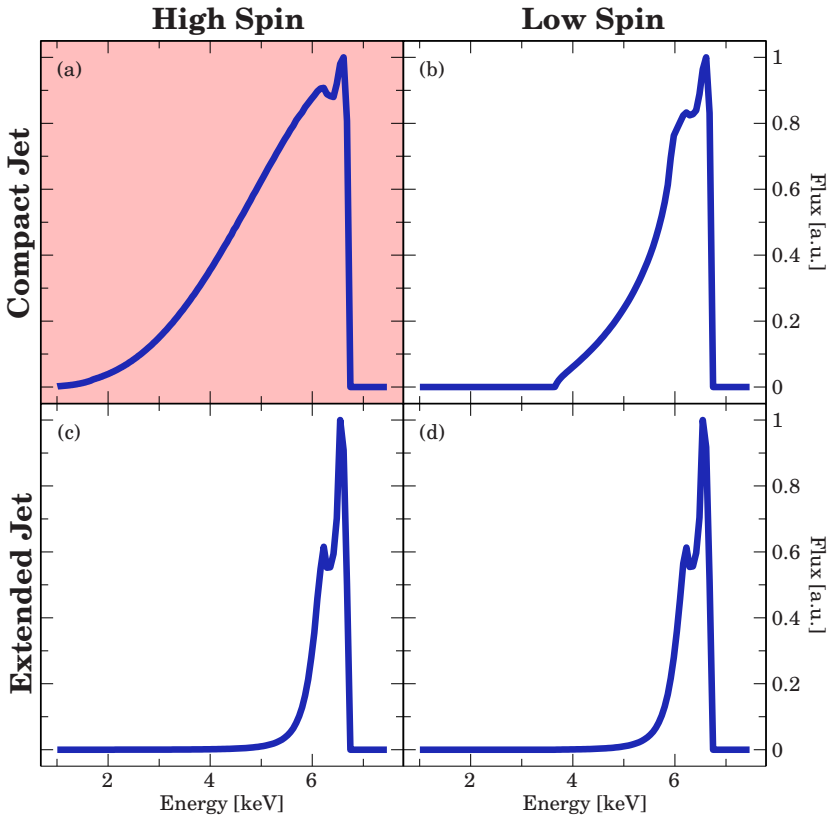

Fig. 2.16: *The line shape for combinations of high and low spin ($a = 0.99$ and $a = 0$) of the black hole and for irradiation by a compact jet (point source at $3r_g$) and an extended jet (from $3r_g$ to $100r_g$). Only for high spin and a compact, low jet the line will be observed as being broad (a, red field).*

be explained by the irradiation from an largely elevated (Chiang et al., 2012) or elongated source (Fig. 2.15k). Additionally, note that it will be shown in Sect. 4.3 that systems with a truncated disk are not able to produce show a strong reflection component.

Besides the spin, the inclination of the system has also a strong effect on the line shape (see, e.g., Dauser et al., 2010). As the inclination is mainly determined by defining the maximal extent of the line at the blue side (Fig. 2.15), the steep drop is always at the same location for a fixed inclination and can therefore be determined almost independently of the geometry.

In summary, Fig. 2.15 confirms that the relativistic reflection feature is sensitive to very different parameters in the lamp post geometry. However, as soon as the primary source is not very close to the black hole or is elongated in the radial direction, the dependency on parameters such as the spin of the black hole or the incident spectrum is not large.

2.7.3. Implications for Measuring the Spin of a Black Hole

If we are interested in measuring the spin of the black hole by analyzing the relativistic reflection, Fig. 2.15 and the discussion in the previous section help us to decide under which conditions we are capable in doing so. Generally, these conditions can be separated into two classes: Either the primary source is compact and very close to the black hole, or the irradiating emission comes from larger heights or an elongated structure. As has been shown in the previous section, the latter case, a large height of the primary source and an elongated structure, produces a very similar irradiation of the accretion disk and therefore we use following picture for this discussion: The base of the primary source is always located at $3r_g$ and simply the top height of the elongated structure is allowed to change. For simplicity we call it a “compact jet” if the top height of the source is close to $3r_g$ and “extended jet” for larger values of the top height.

As an example, Fig. 2.16 shows how a line profile for different spin would look like for a compact and extended jet. In the case of a compact jet the sensitivity on the spin is high (see Fig. 2.15d) and therefore we can clearly see the difference of a really broad line for high spin (Fig. 2.16a) compared to a much narrower line for low spin (Fig. 2.16b). If the irradiating source is elongated, the line profiles for high and low spin are very similar and especially really narrow (Fig. 2.16c,d). At first this underlines what was already discussed above in the context of Fig. 2.15: If we have an elongated source we will not be able to constrain the spin at all.

But the diagram in Fig. 2.16 reveals a much larger problem we have to deal with. Namely three of the four lines in the Figure will be detected as narrow lines and when fitted with any model simulating broad lines, will result in very low spin values. But this would be wrong in the case of Fig. 2.16c, where the black hole is rapidly rotating, but only the elongated structure renders the line profile narrow. Reversing the arguments, this implies that observations of a narrow line[8] do not allow to draw any conclusions about the spin of the black hole without knowing the exact geometry of the primary source. Hence, any black hole which was inferred to be slowly rotating due to its narrow reflection feature might very well be rapidly spinning if the accretion disk is irradiated by a source which is not compact or close to the black hole.

2.7.4. Simulated Observations with current Instruments

In order to quantify the argumentation of the previous section several simulations were performed, on how sensitive spin measurements can be depending on the geometry of the irradiating source. For this purpose the EPIC-pn camera (Strüder et al., 2001) of the *XMM-Newton* satellite (Jansen et al., 2001) was employed, a widely used instrument for measuring reflection features and determining the spin of a black hole (see, e.g., Wilms et al., 2001; Fabian et al., 2009; Duro et al., 2011). See also Chapter 3 for more information on X-ray data analysis with *XMM-Newton*.

Figure 2.17 shows 100 ksec observations of an iron Kα feature for different cases, namely of a compact primary source (Fig. 2.17a) and an elongated source (Fig. 2.17b), which might also be accelerating (Fig. 2.17c). Looking at the equivalent widths in the figure clearly reveals by what amount the line changes from a highly to a non-rotating black hole. For the canonical case, a compact primary source, there are large differences visible, already for a very common exposure time of 100 ksec. On the other hand, in the case of an elongated source (Fig. 2.17b), there is virtually no difference at all and even future instruments will not be able to deduce the spin in this case. If the elongated source is accelerating strongly (Fig. 2.17c), slight differences arise (see dashed lines) but still stay deeply hidden within the uncertainties of the measurement.

As illustrated in Sect. 2.7.3, the inability of measuring the spin for certain geometries is not the major problem. This approach assumes that we know the geometry of the primary source, which is generally not the case. Hence, the interesting question is, what spin value would we measure when we assume the "standard" geometry ($I \propto r^{-3}$) currently used? Table 2.1 summarizes the results of such an investigation: The data is simulated for a spin value of a_{bh}, which is then fitted by a different model, yielding the spin parameter a. As expected, simulating a compact source yields nicely consistent results of spin value when fitted by the standard geometry. Contrary to that the elongated source, which produces a very narrow line (see Fig. 2.17b), is always fitted by a very low spin, independent of the actual spin of the black hole. Especially for highly rotating black holes this solution is in great contrast to the original value and even for a 100 ksec observation with current instruments far outside the confidence limits. If the elongated source now strongly accelerates while emitting photons, the obtained spin values resemble more the true ones ($a = 0.5^{+0.2}_{-0.3}$ for

[8] narrow, but still broad in CCD resolution

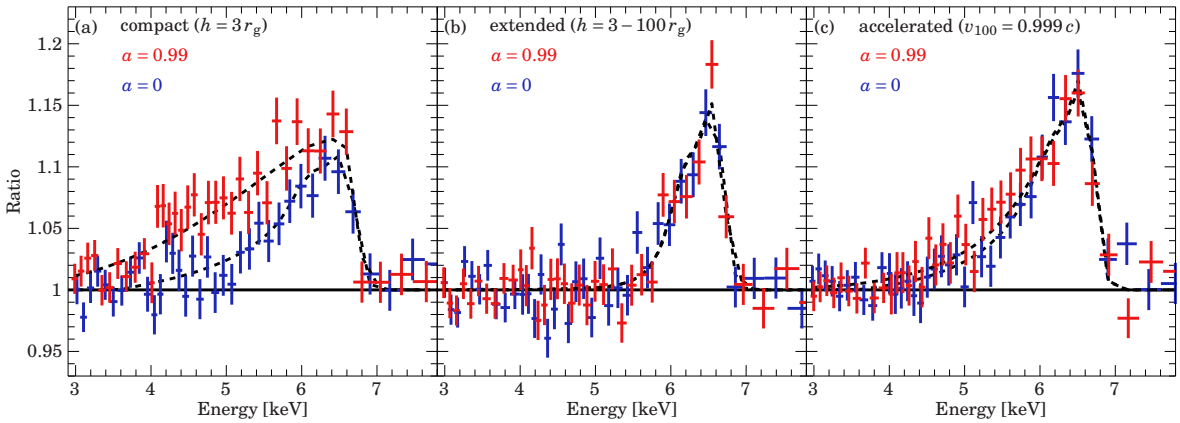

Fig. 2.17.: *A simulated XMM-Newton observation of* 100 *ksec exposure of the Fe Kα line for (a) a compact ($h = 3r_g$), (b) an extended jet ($h = 3$–$100r_g$), and (c) again an extended jet ($h = 3$–$100r_g$), but now extremely accelerated such that $v_{100} = 0.999\,c$. Parameters were taken to be similar to MCG−6-30-15 in the XMM-Newton observation with Obs. ID 0111570101 (Wilms et al., 2001). In order to obtain consistent line strengths the desired geometry was fixed and then the spin value and the normalization of the line was fitted to the data. The equivalent widths for high spin compared to non-spinning were determined to 432 eV vs. 175 eV (a), 110 eV vs. 109 eV (b), and 255 eV vs. 208 eV (c). Figure taken from Dauser et al. (2013).*

Tab. 2.1.: *This table summarizes the result of a simulation which tries to illustrate what spin value a would be obtained if we use the "standard" geometry (i.e., where the emissivity is proportional to r^{-3}) for describing data, which was originally produced by a more complex geometry of the primary source (compact, extended, or accelerated). This simulation was performed for two different values of spin ($a_{bh} = 0.99$ or $a_{bh} = 0.0$). All details are identical to the simulation described in Fig. 2.17.*

	compact	extended	accelerated
$a_{bh} = 0.99$	$1.00^{+0.00}_{-0.06}$	$-1.00^{+0.27}_{-0.00}$	$0.45^{+0.24}_{-0.34}$
$a_{bh} = 0.0$	$0.2^{+0.5}_{-0.6}$	$-1.0^{+0.4}_{-0.0}$	$-0.3^{+0.4}_{-0.7}$

$a_{bh} = 0.99$ and $a = -0.3^{+0.4}_{-0.7}$ for $a_{bh} = 0.0$). However, these values still do not agree with the real spin of the black hole. As this misleading determination of the spin does not fail due to low sensitivity but a lack of information of the primary source, future satellite missions or longer exposures will not be able to solve this issue automatically.

2.8. Conclusions from the Jet Base Geometry

In this Chapter a consistent approach in general relativity for modeling the irradiation of an accretion disk in the lamp post geometry was introduced. Besides a stationary point source, I also showed how a moving, a radially elongated, or an accelerating primary source can be easily modeled by slightly extending the formalism. I presented an extension to the `relline` code (Dauser et al., 2010), which can be used for model fitting in common data analysis programs and is capable of describing all different kinds of primary sources mentioned above. It was shown that only for a compact primary source the spin of the black can be measured properly. Elongated sources will

always produce a narrow relativistic reflection feature. Even if we introduce a strong acceleration, the simulation showed that the spin cannot be determined for such a setup and might be confused with a compact irradiating source around a non- or negatively rotating black hole.

For the different geometries of the primary source the difference in emissivity profiles was analyzed. Most importantly we could see that the innermost part (i.e., $r < 2r_g$), which is also the steepest part of the profile, is completely independent of the geometry and movement of the source (see also Fukumura & Kazanas, 2007). By changing the geometry in the lamp post setup, we will not be able to create steeper profiles than the standard one for a point source in order to explain the really steep emissivity indices measured in many observations (see, e.g., Wilms et al., 2001; Fabian et al., 2002; Fabian et al., 2004; Brenneman & Reynolds, 2006; Dauser et al., 2012). Even sources extended perpendicular to the rotational axis seem not to be able to alter the steepness of the emissivity (Wilkins & Fabian, 2012). However, these steep emissivities might be artificially created due to an over-simplified modeling. Recent analysis show that describing the reflection at the accretion disk with a constant ionization, instead of an ionization gradient (see outlook in Sect. 5.3.2) that would be expected from basic arguments (using, e.g., Shakura & Sunyaev, 1973), would result in over-estimating the emissivity index (Svoboda et al., 2012). Moreover it was shown that this independence of the inner part of the emissivity profile from the geometry comes from the fact that this steepening is mainly due to the strong blue-shift the photons exhibit during their flight towards the accretion disk. Although the strong focusing of the photons close to the black hole is commonly used to explain this steepening, Fig. 2.6 evidently showed that this effect actually contributes only little to the steepness, compared to the energy shift.

Using the presented `relline_lp` model, a variety of broad emission lines for very different parameter combinations was produced. This showed that only compact sources close to the black hole produce the really broad lines and are sensitive to parameters like the black hole spin or the steepness of the incident spectrum. Hence, observing a broad line already strongly constrains the primary emission region to be very close to the black hole, which also implies that most of the reflected radiation originates from the innermost parts of the accretion disk. Moreover the narrow line profile created by an elongated primary source is very similar and therefore hardly distinguishable from a point source at an effective, intermediate height. Introducing an acceleration of the elongated source effectively reduces the flux from the upper part of the source. This acceleration leads to a broadening of the line shape, which means that it becomes again more sensitive to the black hole parameters and more similar to the line profile created by a compact source at low height.

Simulating observations with current instruments, the line profile of elongated sources will always be rather narrow. Applying standard line models to X-ray spectra of such systems will always result in a low spin of the black hole, although this might not be the actual case. Hence, only a really broad emission line will give us the possibility to determine the spin of the black hole unambiguously. Such systems must have a compact emitting source and a rapidly rotating black hole. In all other cases with narrower lines, the emission line can either be described by a slower rotating black hole or an elongated source, which could have any arbitrary spin. The idea that a narrow, relativistic reflection feature might be produced by a primary source at a larger distance to the black hole is not new. Vaughan et al. (2004) suggested such a geometry to explain the reflection feature in Akn 120, as it required a flat emissivity at the inner edge of the accretion disk. In agreement with our results presented above, Chiang et al. (2012) conclude for XTE J1652−453 that the spin cannot be constrained if the primary source is assumed to be located at a large height above the black hole.

Note that in some sources broad lines have been seen to be changing. Galactic black holes are seen in two states, a hard state where the X-ray continuum is a power-law with an exponential

cutoff that can be well described by a Comptonization continuum with (relativistically smeared) reflection, and a soft state in which thermal emission from an accretion disk dominates the emission (see, e.g., McClintock & Remillard, 2006, for a review). During the hard state a relativistic outflow is present in these systems, which is quenched during the soft state (Fender et al., 2004). This jet can carry a significant percentage of the total accreted power (Russell et al., 2007, and references therein). In many models for the black hole states it is assumed that the inner disk radius is receded outwards during the hard state and that it only extends to the ISCO during the soft state (e.g., Esin et al., 1997; Dove et al., 1997; Fender et al., 2004). If the Comptonizing plasma is located close to the accretion disk, an inward moving accretion disk would increase Compton cooling of the Comptonizing plasma, which then collapses, resulting in the soft state. One of the major observational arguments for this picture are changes of the relativistically broadened line in these systems. For example, the Galactic black hole GX 339−4 is seen to have a broad line during the more luminous phases of the hard state, i.e., closer to the soft state (Miller et al., 2008, but note Kolehmainen et al. 2011) and a narrow line during the fainter phases of the hard state (Tomsick et al., 2008, see also Nowak et al. 2002). While this behavior is consistent with a receding disk, given the discussion above this picture is not as clear cut anymore. The broad band radio to X-ray spectra of galactic black holes are also consistent with emission from the base of a jet, with a statistical quality comparable to that to the disk-corona models (Markoff et al., 2005; Nowak et al., 2011). Furthermore, the jet properties in these sources are observed to change as the state approaches the intermediate and soft states, including the observation of single radio blob ejections close to transitional states (Fender et al., 2006; Wilms et al., 2007; Zdziarski et al., 2011). If this is the case, then according to the discussion above the change in line width from narrow to broad seen in GX 339−4 could also be due to a change in the jet properties from an extended jet far away from the soft state towards a compact jet, rather than a change in the inner disk radius (see also Miller et al., 2012).

For observations of sources where the line shape changes only on very long timescales, such as AGN, our results imply that solely relying on spectral fits we are only able to measure the spin of rapidly rotating black holes. All other spin values obtained from fitting reflection spectra are not trustworthy, as they can be easily explained by changing the geometry of the irradiating source. This result is of significant importance, e.g., when trying to use spectral black hole spin measurements to infer the spin distribution of the local black hole population, as it introduces a significant bias towards sources with small jet sizes.

Fortunately, however, reflection measurements are only one of several independent ways to determine black hole spins. For Galactic sources, where the accretion disk temperature is large enough that it can be observed in the soft X-rays, it is possible to use the shape of the accretion disk spectrum to infer the black hole spin (Zhang et al., 1997; Li et al., 2005; McClintock et al., 2010, but see Dexter & Quataert 2012). Where a broad line is observed, the results of continuum spin measurements and line measurements agree (e.g., Gou et al. 2011 and Duro et al. 2011 for the case of Cyg X-1). Furthermore, X-ray reverberation techniques allow constraining the location of the primary source through measuring X-ray time lags between the continuum and the reflection spectrum (Stella, 1990; Matt & Perola, 1992; Reynolds et al., 1999; Poutanen, 2002; Uttley et al., 2011, and references therein). Despite the comparatively small effective area of current X-ray instruments, such measurements have already been successfully applied to a small subset of extragalactic black holes, e.g., 1H0707−495 (Fabian et al., 2009; Zoghbi et al., 2010; Zoghbi & Fabian, 2011; Kara et al., 2013), NGC 4151 (Zoghbi et al., 2012), MCG−6-30-15 and Mrk 766 (Emmanoulopoulos et al., 2011), and PG 1211+143 (de Marco et al., 2011)). In all these measurements the primary source was constrained to be compact, extending only in the order of a few-to-tens r_g away from the black hole. Current concepts for the next generation of X-ray satellites such as

the Advanced Telescope for High Energy Astrophysics (*ATHENA+*; Barret et al., 2013; Nandra et al., 2013, and the discussion in Sect. 5.3.1) all have a large effective area. With such large collecting areas it will be possible to measure high-quality X-ray spectra for a larger sample of AGN within the typical light travel timescales for the lamp post model. These facilities will allow X-ray reverberation measurements to constrain the emission geometry of the observed sources such that the degeneracies pointed out above can be broken for a larger sample of sources.

CHAPTER 3

ANALYZING RELATIVISTIC REFLECTION

After producing new relativistic reflection models in the lamp post geometry and analyzing this more physical approach extensively, it is important to also test these models on real observations. Both of the two objects presented in the following depict interesting case studies of measuring relativistic reflection. The GBH Cygnus X-1 (Sect. 3.2) is an extremely bright source, where much information from decades of observations is available. Besides the inclination of the system, also the spin estimated by fitting the relativistic corrections to the thermal black body is known. The challenge is to test if our understanding and the developed models of the relativistic reflection agree with other methods and measurements. The observations analyzed in the following are the best signal to noise observations of relativistic reflection in GBHs. Moreover, simultaneous data of three different X-ray satellites was available to constrain the reflection spectrum. The other source considered, the SMBH black hole 1H0707−495 (Sect. 3.3), is well know for its very prominent drop around the iron K edge (Boller et al., 2002). It also was the first source to show a relativistically broadened iron L line (Fabian et al., 2009). In total, two observations of in total 1 Msec of data are analyzed in order to understand the complicated spectrum of this AGN.

3.1. BASIC INFORMATION ON THE APPLIED DATA ANALYSIS

Although the detailed data analysis of the two cases studies presented in the following largely differs, this paragraph briefly summarizes the very basic concepts and tools. All spectra were analyzed using the *Interactive Spectral Interpretation System* (ISIS, Houck & Denicola, 2000; Houck, 2002), which is a interactive software tool working with the scripting language S-Lang. Besides the built in functionalists, many useful data analysis functions were used from the Remeis ISISscripts[1].

For both objects, the most important detector was the EPIC-pn camera (Strüder et al., 2001) on board the *XMM-Newton* satellite (Jansen et al., 2001). The reason for this is the large effective area around the Fe Kα transition, combined with the high resolution of the CCD detector in the EPIC-pn camera needed to resolve features of the relativistic reflection. As the full energy range of this detector is from 0.5 keV–10 keV, it also captures the lower energetic reflection features, like the broad iron *L* around 1.2 keV. Data reductions were done with the most recent version of the *XMM-Newton* Software Analysis System (SAS) and the newest calibration files available at the time of publication.

When modeling the relativistic features, a complete reflection spectrum and not only a single emission line was always used. The reflection was described by, the `reflionx` model Ross & Fabian (2005); Ross & Fabian (2007). This reflection was then convolved with the relativistic convo-

[1] See `http://www.sternwarte.uni-erlangen.de/isis/` for more information.

lution kernel `relconv` (Dauser et al., 2010, 2013). Note that very recently I developed the `relxill` in a joint effort (García et al., 2014), which would have been even better suited for this kind of data analysis. Chapter 4 will treat the advantages and improvements of this model in detail. However, it was not available at the time when analyzing this data, which developed from applying the lamp post implementation of `relline` to this observational data. Reanalyzing the data with the new model was also not feasible bearing in mind the large effort in time and that I could show that the advanced `relxill` model does not lead to significantly different but only better constrained results (see Chapter 4.2).

3.2. The Galactic Black Hole Cygnus X-1

Together with Refiz Duro I analyzed the X-ray data of Cygnus X-1 taken with the *XMM-Newton* satellite, in order to obtain constraints on the relativistic reflection spectrum and the spin of the source. The first of four observation was already published (Duro et al., 2011), while the complete analysis has just been submitted (Duro et al., 2014). The calibration, extraction and technical details were mainly done by Refiz Duro and I focused more on providing the proper relativistic reflection model and fitting the data. In general, the results and their interpretation presented in Duro et al. (2014) and in the following could only be obtained due to the very intensive collaboration. This section is a short summary of the most important results obtained in these two publications, following especially Duro et al. (2014). A strong focus is put on the modeling and the interpretation of the relativistic reflection. The reader is referred to the PhD thesis of Duro (2014) for more details.

3.2.1. Data Analysis

As Cygnus X-1 is an extremely bright X-ray source (up to 300 mCrab, see, e.g., Grinberg et al., 2013), the EPIC-pn camera was operated in the Modified timing mode (Kendziorra et al., 2004). This procedure increases the lower energy limit of the detector to 2.8 keV. See the appendix in (Duro et al., 2014) for more details on this mode. In order to reliably determine the shape of the relativistic reflection, simultaneous data from the *RXTE* satellite (Bradt et al., 1990; Giles et al., 1995) was used. Combining the PCA (Jahoda et al., 2006) and HEXTE (Rothschild et al., 1998) detector on board this satellite, an additional coverage from 3 keV up to 120 keV is achieved (see Duro et al., 2014, for details on the extraction). Besides extending the energy range and therefore allowing us to constrain the reflection better by modeling the Compton hump between 20–40 keV, also the crucial energy range around the iron K transition is observed by two independent detectors. As described in Duro et al. (2011) and more detailed in the appendix of Duro et al. (2014), an apparent mismatch between EPIC-pn and PCA led to the discovery that the spectrum taken by *XMM-Newton* suffers from gainshift problems. The extremely high count rate effectively leads to an over-correction of the gainshift due to Charge Transfer Efficiency (CTE) effects in the EPIC-pn camera. Using the PCA and data from the *Chandra* satellite we were able to correct for this, by applying a gainshift correction of 2% to each photon energy. A detailed description of this complicated treatment is given in Duro et al. (2014). Using also data from the ISGRI detector (Lebrun et al., 2003) on-board the *INTEGRAL* satellite (Winkler et al., 2003), the energy was extended up to 500 keV to allow to fix the complete continuum spectrum even better.

The *XMM-Newton* data was taken from 2004 November to December in four observations between 19 ksec and 10 ksec (Obs-IDs 0202760201, 0202760301, 0202760401, 0202760501, named `Obs1-Obs4` thereafter). Cygnus X-1 is found to be in the hard-intermediate state, i.e., during a

failed state transition from the hard to the soft state (see, e.g., Grinberg et al., 2013, for a classification of the states of Cygnus X-1). The data was rebinned to a S/N= 100, which over-samples the detector resolution by about a factor of 4 (40 eV at 6.4 keV).

3.2.2. The Reflection Spectrum of Cygnus X-1

As is extensively discussed in Duro et al. (2014), a complete relativistic reflection spectrum is needed to be able to describe the data. Besides the reflection, the continuum consists of a power law with an exponential cutoff at ~170 keV and a multi temperature accretion disk (Mitsuda et al., 1984). Strong absorption lines of highly ionized iron, namely Fe XXV and Fe XXVI, are found in the data along with a fluorescent neutral Fe Kα originating from the distant wind (see, e.g. Hanke et al., 2009; Miškovičová et al., 2014). Figure 3.1 shows the model components along with the data. The most important parameters of the intrinsic reflection are the iron abundance of the accretion disk and its ionization state.

Modeling the actual shape of the relativistic reflection is the crucial part in this analysis. Using the empirical disk emissivity profile ($I \propto r^{-\epsilon}$, see Chapter 2 for more details regarding the irradiation of the accretion disk), a good fit to the data can be obtained. Similar to Fabian et al. (2012a), a broken power law emissivity yields the best results. Namely, we find a steep emissivity of $\epsilon \sim 5$–10 for all four observations at the inner part of the disk. Hence, most of the reflected radiation from Cygnus X-1 comes from the innermost regions of the accretion disk. Beyond the break radius, which is found to be around 3–4 r_g, we require the standard emissivity of $\epsilon = 3$ to which the emissivity necessarily has to converge for larger distances to the black hole (see Chapter 2, Fig. 2.8). In all cases, the inclination angle is higher, but almost consistent within the uncertainties to the inclination angle of the system ($\theta_{sys} = 27°$, Orosz et al., 2011). As expected from such a system, the accretion disk is found to be moderately ionized in all observations ($\xi \sim 2000$) with an iron abundance between 4–6 times the solar abundance. See Table 2 in Duro et al. (2014) for more details on the parameters of the fit.

Determining the spin from these observations requires even more care. In Duro et al. (2011), where one of the four data sets was analyzed with less broad band coverage, a reliable spin estimate could only be made by rejecting an unphysical solution consisting of a low spin but very steep emissivity at the inner parts. Including *INTEGRAL* data at highest X-ray energies improves the situation slightly, however, two solutions still remain. In order to further improve the degenerated situation and get a more physically consistent description of the irradiation, we employ the lamp post geometry for constraining the spin as well (see Chapter. 2).

The contour plots in Fig. 3.2 map for both models, the standard coronal model and the lamp post model, the parameter space between the emissivity profile, the inclination, and the spin. This plot evidently shows the degeneracy for the coronal model, already found by Duro et al. (2011). In all four observations there exist in principle two solutions for the coronal model, distinguished by a different steepness of the emissivity profile. The upper panel shows that either the data can be described by a large spin and a standard coronal emissivity profile ($\epsilon = 3$) or a slowly rotating black hole with a much steeper emissivity profile ($\epsilon \sim 5$).[2] For both of these solutions the inclination is consistent with each other, while for the standard corona the inclination angle is much less constrained (see lower panel). Employing the lamp post geometry for the irradiation of the accretion disk reduces the degeneracy (see the lower panels in Fig. 3.2). This leads to only one well defined solution for the spin, the inclination, and the height of the primary source, which parametrizes the emissivity profile. Consistently for all observations, a low height of the irradiating source and a

[2] This behavior is most present in Obs1 and Obs4.

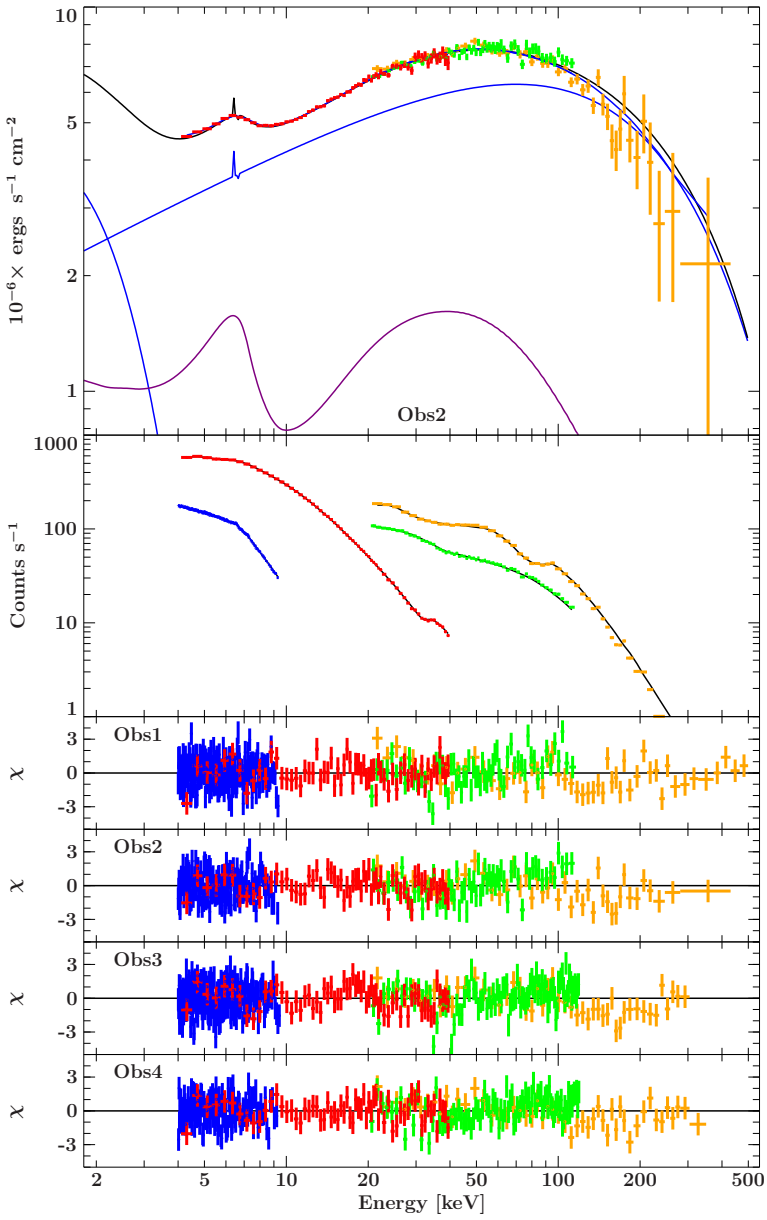

Fig. 3.1: *Upper panel: Unfolded spectrum of Cygnus X-1 taken with EPIC-pn (blue), PCA (red), HEXTE (green), and ISGRI (orange). The continuum and the black body are drawn in red, while the relativistic reflection component is purple. Middle panel: The count rate spectrum. Lower panels: Residuals of the best fit to the data for all four observations. Figure taken from Duro et al. (2014).*

rapidly spinning black hole is found. Although the inclination is predicted at slightly larger values than the optical measurements (Orosz et al., 2011), it is still consistent with these results. Note that recent observations by Tomsick et al. (2014) yield an inclination of at least 13° larger than the optical measurement (Orosz et al., 2011) at a high precision. These measurements were performed by simultaneous observations with *NuSTAR* and *Suzaku*, when Cygnus X-1 was in the soft state. This significant difference in inclination, which is very unlikely due to systematic effects, poses a problem to the general assumption that relativistic parameters do not change on such short time scales. On the other hand this apparent discrepancy might be an indication that the high accretion rate in the soft state produces a warped accretion disk (see, e.g., Pringle, 1996; Fragile, 2009). Such a disk is not any more perpendicular to the spin axis of the black hole at the innermost regions as is the case in the hard state, and might explain the different inclination inferred by similar methods in different states of the black hole. As the optical measurements yield the inclination of the outer disk, the given interpretation is strengthened. Namely that only in the soft state the inner part of

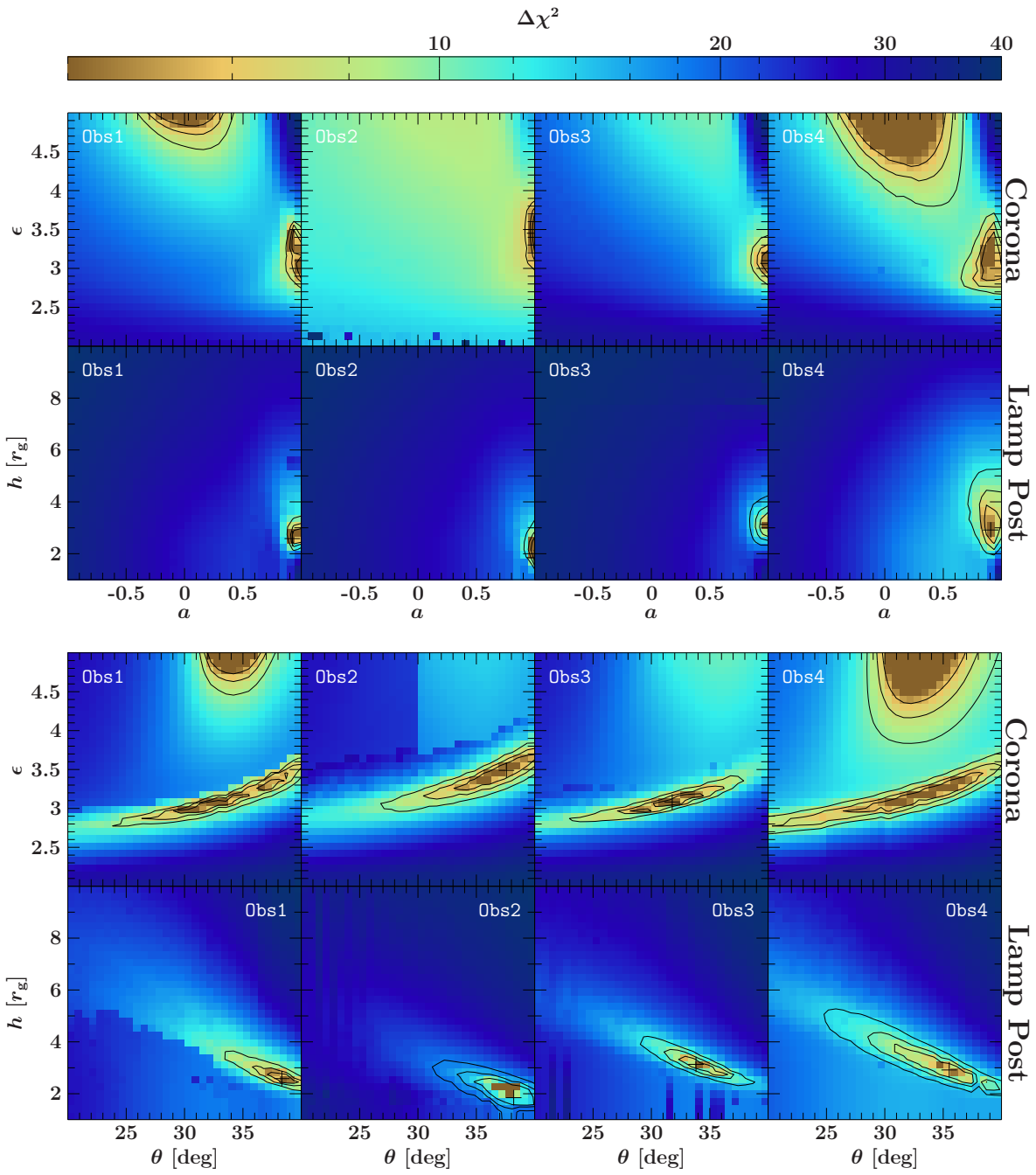

Fig. 3.2.: *Contours plots of the spin for all four observations. Upper panel: Contours between spin and inner emissivity index for the best fit model with a broken emissivity in the coronal geometry. Lower panel: Contours for the lamp post fit, between the spin and the height of the lamp post source. Contour plots adapted from Duro et al. (2014).*

the disk is warped. See Duro et al. (2014) for a larger discussion of this issue.

Using a broken power law emissivity to fit the data, and requiring a steep emissivity at the inner part, has previously been used to also obtain similar results (see, e.g., Fabian et al., 2012a). In Duro et al. (2014) a lengthy analysis and discussion for this case is also provided, leading to very

similar results when compared to the lamp post geometry. As is shown in this publication and also for 1H0707−495 in the next section, such an empirical model usually leads to very similar results when compared to the lamp post geometry. Looking at the calculations of the emissivity profile in the lamp post geometry, this similarity becomes obvious (see Fig. 2.8 and also the discussion in Sect. 2.4): For sources at low height the steep emissivity is already predicted by the lamp post geometry. While leading to very similar parameters, note that the lamp post geometry provides us with additional information. Besides avoiding degeneracies in the model parameters, the lamp post geometry allows to directly fit the height of the source ($h = 2$–$3\,r_g$). Such an estimate then gives us a rough feeling for the geometry of the Cygnus X-1 black hole system. Namely, this suggests that the accretion disk is irradiated by a very compact and centralized primary source of hard X-rays. In general, the lamp post model improves the fit in several points. While the goodness and the other parameters are very similar to the model with the empirical broken power law emissivity profile, the situation for the spin improves: It is now constrained to $a \sim 0.9$. The contours in Fig. 3.2 evidently show that the model is able to consistently describe the four observations with the same set of parameters. For details on the exact values of the best fit parameters and their uncertainties see Duro et al. (2014).

3.2.3. Constraints on the Spin and the Geometry of the Cygnus X-1 System

In summary, we can describe the relativistic reflection spectrum of Cygnus X-1 with a consistent set of parameters. As parameters like the spin are not expected to vary on such short timescales, this consistency is crucial for the reliability of our modeling. Note while the axis of the black hole spin is not expected to change, the apparent difference in inclination between this and the recent Tomsick et al. (2014) observation might be explained by a warped accretion, created in the soft state in the latter case. But besides these complications, it was shown that while Cygnus X-1 is in a similar state (i.e, for the four observations presented above), consistent results are obtained. In comparison with other measurements, it can be concluded that Cygnus X-1 is found to be rapidly spinning in all recent work, regardless of its state: While being in the soft state, Gou et al. (2011) retrieve a high spin of Cygnus X-1 from the continuum fitting method, after proper measurements of the inclination and the mass have been made (Orosz et al., 2011). Also for the hard state, Fabian et al. (2012a) confirm the high spin of Cygnus X-1. In a combined observation of *Suzaku* and *NuSTAR* (Tomsick et al., 2014) the continuum and the reflection method were applied, yielding again consistently large spin values.

Regarding the accretion geometry of the system, no distinct solution could be obtained. While the lamp post geometry yields a slightly better fit than the empirical power law emissivity (see Duro et al., 2014, for more details), a different shape of the corona can not be excluded. However, as explicitly showed in Chapter 2 (see Fig 2.16), the high spin in Cygnus X-1 strongly support a very compact irradiating source close to the black hole. Also the fits in the lamp post geometry suggest that the primary source is consistently about 2-3 r_g away from the black hole. Therefore also the extend of the irradiating source is less then a few r_g in size. Regardless of the exact geometry a compact solution is required, being probably a combination of a forming jet base and a corona.

The success in obtaining these consistent results is due to the high quality data in terms of signal to noise, combined with simultaneous coverage of other X-ray satellites. The extended energy range was able to fix the continuum, allowing for a precise measurement of the relativistic parameters. Moreover, more physical assumptions by employing the lamp post model, efficiently removed unphysical solutions which led to a unique description of the data. Therefore, Cygnus X-1 can be

called an important test case for measuring relativistic reflection. The good agreement of the results, regardless of the state of the source and the applied methods, validates our approach and the applied models.

3.3. THE SUPER MASSIVE BLACK HOLE 1H0707−495

Binary systems like Cygnus X-1, which was analyzed in the previous section, are characterized by strong variability in flux and also spectrum (see, e.g., Böck et al., 2011). Due to the much larger mass, reflection spectra from the inner parts of the accretion disks around super massive black holes are more constant on the typical observation time scales[3]. For the AGN 1H0707−495, two extremely long observations (500 ksec), spaced almost 3 years apart were available. Analyzing the data allows again to test the stability of the assumed model and the relativistic parameters also for the complicated spectrum of this source. Due to its very strong reflection and low absorption, 1H0707−495 is also an ideal example to apply the new lamp post model `relline_lp`. The analysis presented in the following is a detailed analysis of the available 1H0707−495 data. It has been published in Dauser et al. (2012). Therefore the following section strictly follows this publication, also taking large parts in verbatim.

3.3.1. THE AGN SYSTEM

The Narrow Line Seyfert 1 galaxy 1H0707−495 at a redshift of $z = 0.04057$ (Jones et al., 2009) is well known for its huge and sharp drop in flux at ∼7 keV. Discovered by Boller et al. (2002), this feature was initially interpreted as an absorption edge despite the lack of a fluorescent emission line. Subsequent models for the feature included partial covering by a thick absorber (Tanaka et al., 2004), which also explains the temporal changes seen in its location (Gallo et al., 2004). In a long *XMM-Newton* observation, however, Fabian et al. (2009) and Zoghbi et al. (2010) showed that relativistically broadened fluorescent iron Kα emission is a more likely explanation, especially given that these authors could also show that the source's soft-excess can be modeled by a relativistic iron Lα line, the first one ever observed. That the position of the two lines and the ratio of the normalizations agree with expectations adds further evidence to the reflection scenario (Fabian et al., 2009). In order to produce such a strong feature and an observable Fe Lα line, the iron abundance in 1H0707−495 has to be several times the Solar composition. The new observations also ruled out the partial covering explanation for the feature, as the strong absorption lines and edges predicted by these models are not compatible with high resolution X-ray spectra (Zoghbi et al., 2010). Recently, Fabian et al. (2012b) observed 1H0707−495 at low flux, confirming the reflection dominated interpretation. The same physical interpretation also successfully describes the spectra of similar AGN, e.g., IRAS13224−3809 (Boller et al., 2003; Ponti et al., 2010), too.

3.3.2. DATA ANALYSIS

In the following a detailed explanation of the data analysis procedure is given, which is taken from Dauser et al. (2012). Specifically, data of 1H0707−495 is analyzed from a ∼500 ksec long observing run of the *XMM-Newton* satellite (Jansen et al., 2001) from 2010 September 12 until 2010 September 19 (*XMM-Newton* revolutions 1971–1974, corresponding to the Obs. IDs 0653510301, 0653510401, 06535105010, and 653510601). These data are then compared to ∼500 ksec of mea-

[3] Note that this clearly excludes the variability seen in Blazers, when looking directly into the jet. Due to special relativistic beaming, this variability can be strongly enhanced.

surements from an earlier *XMM-Newton* observation of the source performed from 2008 January 29 to 2008 February 06. A focus is put on data from the EPIC-pn camera (Strüder et al., 2001) and the reflection grating spectrometer (RGS; den Herder et al., 2001). Data were reduced using the *XMM-Newton* Software Analysis System (SAS v.11.0.0) and the newest calibration files at the time of publication.

Both sets of observations were analyzed in the same way. The linearized event files of the four consecutive observations were merged into a single event file. These data were cleaned for high background times following Schartel et al. (2007) and Piconcelli et al. (2005), resulting in final exposure times of 328 ksec and 410 ksec for Rev. 1491–1494 and Rev. 1971–1974, respectively. The EPIC-pn source spectra were extracted from a circular region with a radius of 36″ centered on the maximum of source emission. In order to avoid any issues due to background Cu K emission lines from the electronic circuits on the back side of the detector (see Zoghbi et al., 2010), background data were taken from a different chip, using a circular region of the same size at a CCD position located at a similar distance from the readout node as the source position (see "XMM-Newton Users Handbook", Issue 2.9, 2011, ESA: XMM-Newton SOC).

In order to exclude any contamination of the spectra due to pile up, a light curve with a resolution of 40 s was generated and only times with count rates below 10 counts s^{-1} were included in the final spectrum (SAS extraction expression `(RATE> 0.5) && (RATE≤ 10.0) && (FRACEXP> 0.7)`, the last expression guarantees that each bin has an exposure of at least 70%)[4]. Excluding data with count rates above 10 counts s^{-1} changes the average flux by about 5% (Fig. 3.3, right). These changes are highest in the lower energy band, which dominates the overall source spectrum and is therefore the spectral part which is crucial for determining the spectral parameters. The light curves were extracted in the same manner, except that we dropped the condition (RATE≤ 10.0).

Note that since the publication of the earlier *XMM-Newton* observation of 1H0707−495 (Fabian et al., 2009; Zoghbi et al., 2010) the calibration of the EPIC-pn camera has significantly changed in the soft X-rays (3% below 0.6 keV, see Fig. 3.3, left). The newer response is now in line with simultaneous measurements from the RGS (see XMM-CCF-REL-266, available at `http://xmm2.esac.esa.int/external/xmm_sw_cal/calib/rel_notes/index.shtml`). In order to take into account any remaining systematic uncertainties in the complex spectral models as well as any remaining calibration uncertainty, a systematic error of 3% is added to data taken below 1.2 keV.

The RGS spectra were processed with the SAS task `rgsproc` with calibration files created mid April 2011. The observations were screened for high background times in the standard way and run with the RGS rectification on (see XMM-CCF-REL-269, available at `http://xmm2.esac.esa.int/external/xmm_sw_cal/calib/rel_notes/index.shtml`), which allows a direct comparison with EPIC-pn results.

Simultaneously to the *XMM-Newton* observations, between 2010 September 12 and 2010 September 19, 1H0707−495 was also observed with the *Chandra* satellite (Canizares et al., 2005) for a total of 118.2 ksec (Obs. ID 12115, 12116, 12117, and 12118). The Medium and High Energy Transmission Gratings spectra (METG and HETG) were extracted and the grating ARFs and RMFs were created using the standard `ciao` threads (v4.1) and `caldb` v4.1.2. The spectra for each observation and for the +1 and -1 orders were then combined using standard `ciao` scripts.

Spectral fitting was performed with the *Interactive Spectral Interpretation System* (*ISIS*; Houck & Denicola, 2000). Data were rebinned to over-sample the intrinsic energy resolution of the EPIC-pn camera slightly, requiring a rebinning to 2, 3, 10, 15, and 25 bins for energies above 0.8, 2.0, 4.0, and 7.0 keV, respectively, where one bin has a width of 5 eV. Where necessary, data were rebinned further in order to reach a signal to noise ratio of $S/N > 2.5$. All uncertainties are given at 90%

[4] This selection is not fulfilled for 2.4% (Rev. 1491–1494) and 5.3% (Rev. 1971–1974) of these time bins.

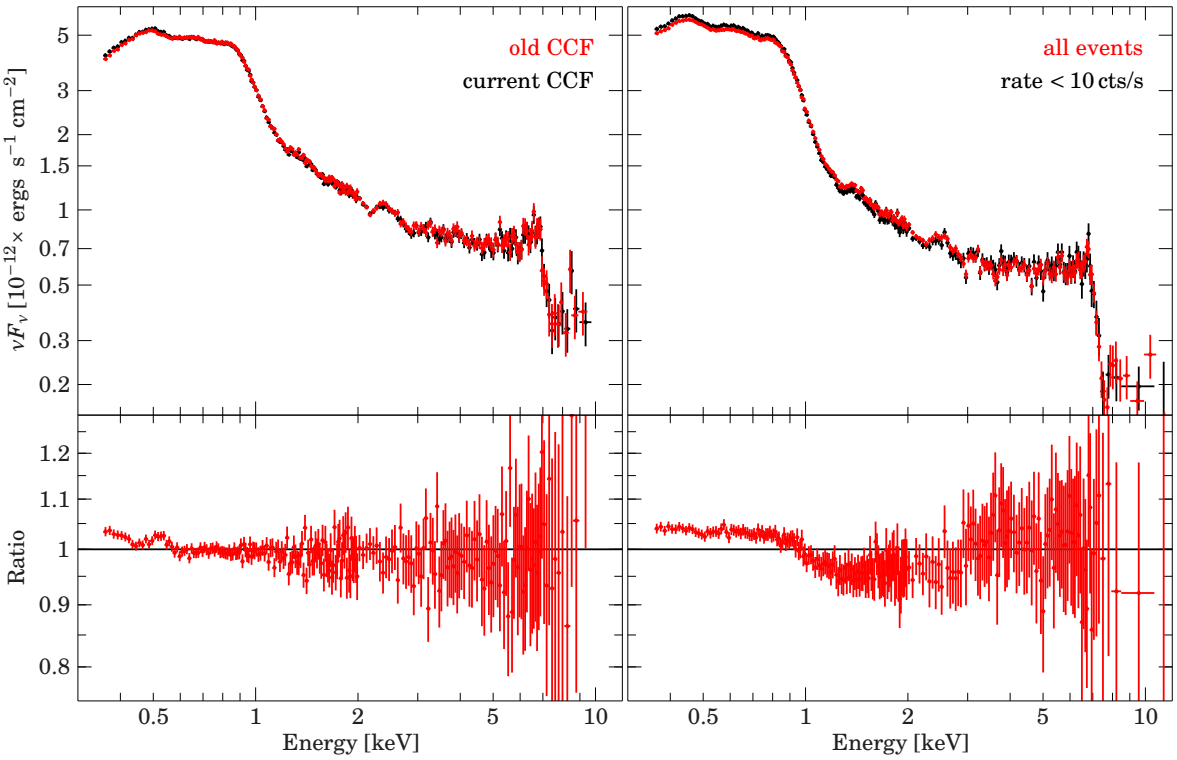

Fig. 3.3.: ***Left**: Comparison of the extractions for Rev. 1491–1494 between the current calibration of the EPIC-pn (black, calibration date 2011-09-13) and the older version (red, 2009-07-01). The bottom figure shows the ratio between the data sets. **Right**: Spectra of Rev. 1971–1974 obtained for a "normal" extraction (red) and an extraction with the conditions* `RATE` < 10 *(black). All spectra are normalized in flux to the "black" spectra. Figure taken from Dauser et al. (2012).*

confidence if not stated differently.

3.3.3. The X-ray spectrum of 1H0707−495

Strictly following Dauser et al. (2012), a thorough presentation of the X-ray spectrum of 1H0707−495 is given in the following. As known from previous observations, 1H0707−495 is a highly variable Narrow Line Seyfert 1 Galaxy (see, e.g., Leighly, 1999; Turner et al., 1999). Figure 3.4 shows the light curve and hardness ratio during the observation in Rev. 1491–1494 and Rev. 1971–1974. In comparison the older observation (Rev. 1491–1494) was a little less variable (rms variability of 6% compared to 9% for 100 s bins) and slightly weaker (4.6 cts s^{-1} in average compared to 5.1 cts s^{-1}). In combination with the hardness-intensity diagram (Fig. 3.5), where no distinct difference between the two observations can be seen, it is obvious that the source was in a similar state. Nevertheless, this diagram reveals that data from the newer observation are slightly softer (mean hardness ratio of 0.030 compared to 0.038). In Sect. 3.3.5 it will be shown that the softening originates from a softer power law index and a stronger soft-excess, but does not influence other fitting parameters significantly.

Figure 3.6 compares the unfolded spectra of Rev. 1491–1494 and Rev. 1971–1974. Apart from the overall similar spectral shape, a large number of the smaller spectral features are similar, including the "wiggles" in the 2–5 keV band that have been attributed to the complex emission and absorption spectrum of the source (Blustin & Fabian, 2009). Moreover, the characteristic drop at ~7 keV

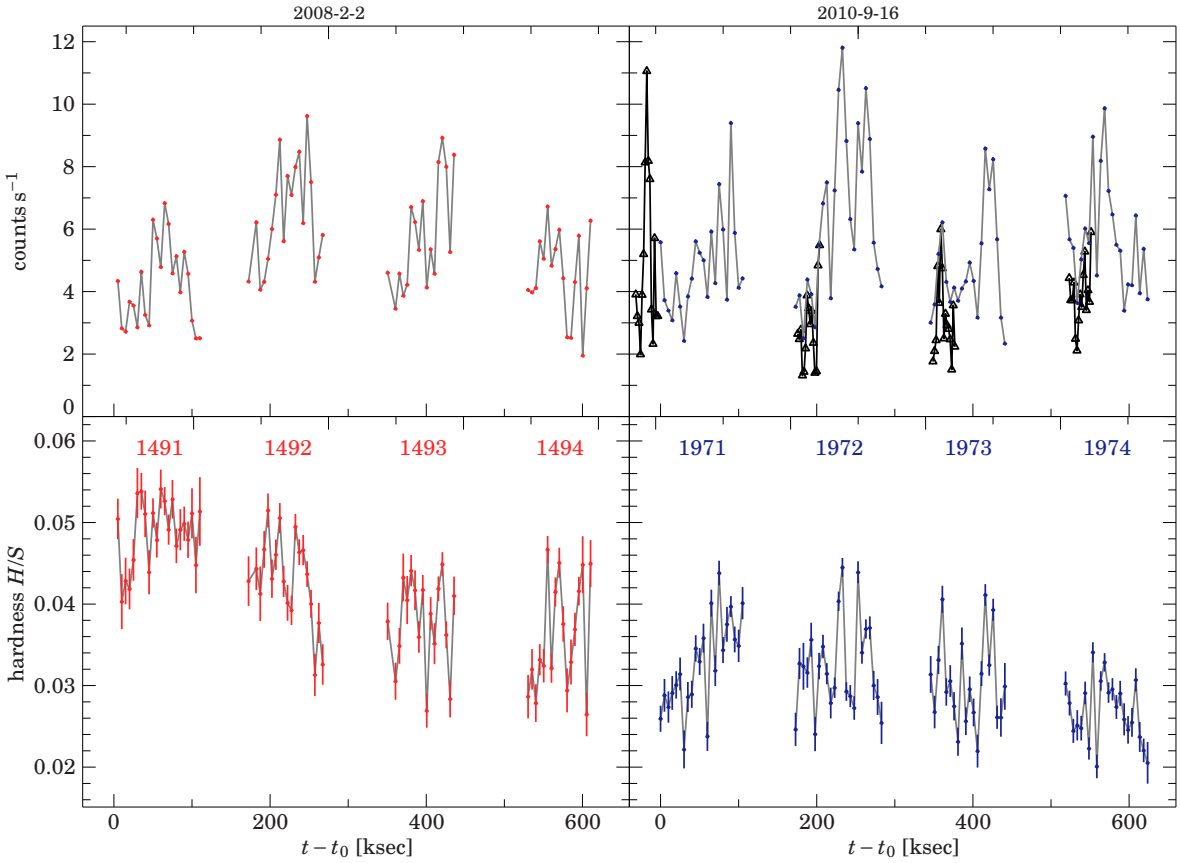

Fig. 3.4.: *Left: Light curve of the measurements analyzed by Zoghbi et al. (2010) (Revs. 1491–1494, red) and Right: Light curve from the 2010 September observations (Revs. 1971–1974, blue). Both light curves are binned to a time resolution of 5 ksec for the energy band* 0.3–10.0 *keV. In addition, the simultaneous Chandra light curve for* 0.35–8.0 *keV is shown below the XMM-Newton light curve (black, triangles). Due to lower count rate, the rate was multiplied by a factor of 50 for comparison. Bottom panels: X-ray hardness for both observations. S and H denote source counts in the bands 0.35–1.5 keV and 2.0–8.0 keV, respectively. Figure taken from Dauser et al. (2012).*

is observed at the same energy. At energies above this spectral drop, more flux is missing than can be explained by a simple softening of the source. As will be shown in Sect. 3.3.7, this difference might be due to variability of an ultra-fast and highly ionized wind, which acts as an absorber.

3.3.4. Broad Band Spectrum and Absorption

The average X-ray continuum is modeled by using the standard spectrum for Narrow Line Seyfert 1 spectra, namely, a steep, absorbed power law spectrum plus (relativistically smeared) X-ray reflection (e.g., Vaughan et al., 1999; La Mura et al., 2011). Initially, foreground X-ray absorption was modeled assuming an equivalent column of $N_{\mathrm{H}} = 4 \times 10^{20}\,\mathrm{cm}^{-2}$ as obtained from the full resolution data of the Leiden-Argentine-Bonn 21 cm survey (LAB survey, Kalberla et al., 2005) and assuming the abundances of Wilms et al. (2000). After adding a weak soft excess modeled by a disk blackbody (Mitsuda et al., 1984; Makishima et al., 1986) with a temperature of $kT_{\mathrm{in}} \sim 100\,\mathrm{eV}$, a basic model which describes the EPIC-pn data well is obtained, although below 0.5 keV, some residuals remain. One explanation for these residuals is additional source intrinsic absorption at a level of

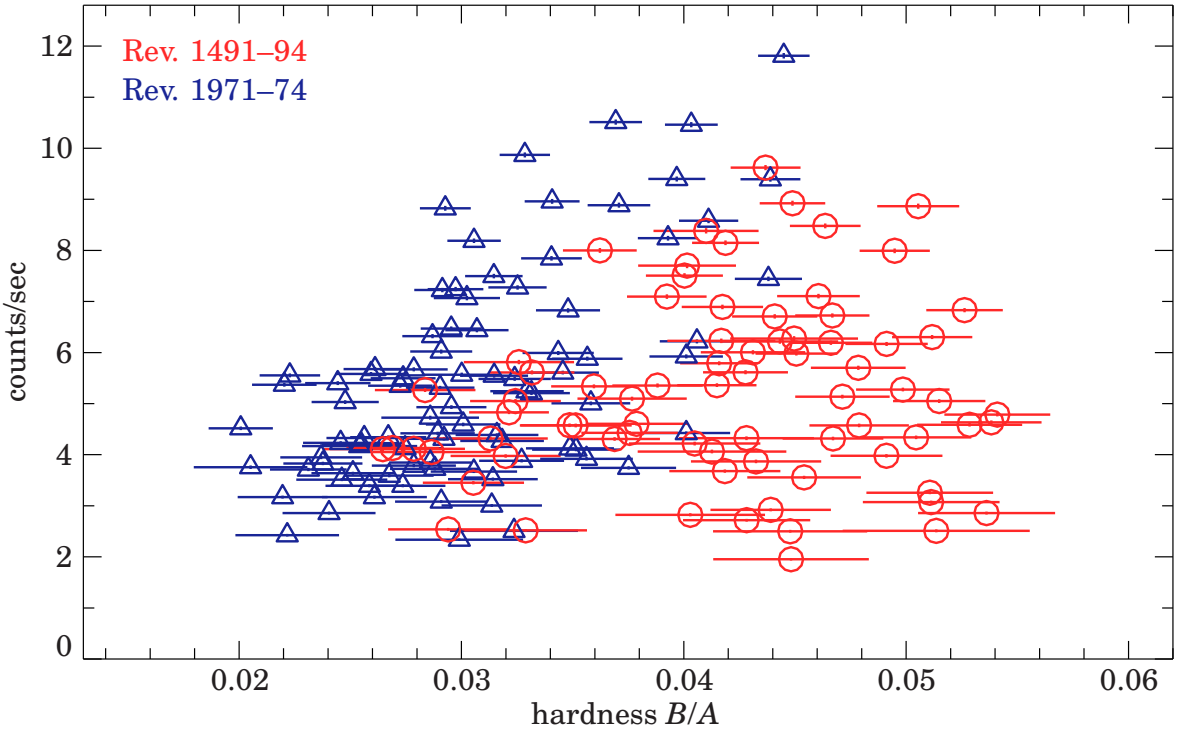

Fig. 3.5.: *Hardness-intensity diagram of the observations, based on a time resolution of 5 ksec. The new observation (Rev. 1971–1974, blue triangles) is slightly but significantly softer than Rev. 1491–1494 (red circles). There is a positive correlation between the hardness and the intensity, which is stronger for Rev. 1971–1974 (correlation coefficient $\rho = 0.60$) than for Rev. 1491–1494 ($\rho = 0.23$). Figure taken from Dauser et al. (2012).*

$\sim 3 \times 10^{20}\,\mathrm{cm}^2$. An increased column in this range is necessary to obtain any good fit at all when extending the lower end of the spectrum to 0.3 keV. If true, however, at this column a resonant O I Kα line at 0.527 keV in the rest frame of the source should be visible, i.e., at 0.506 keV in the measured spectrum, which is not the case (Fig. 3.7). A systematic grid search for any other narrow line associated with a potential absorber failed as well. Any increased neutral N_H must therefore be of Galactic origin. We note that like most 21 cm N_H values quoted in X-ray astronomy, the N_H value quoted above is from an all-sky 21 cm survey with a rather coarse angular resolution of 0.6° such that small scale variations of N_H are washed out. Within 3° of 1H0707−495, the LAB-survey contains points with N_H as large as $8 \times 10^{20}\,\mathrm{cm}^{-2}$. In addition, 21 cm data only probe the gas phase of the interstellar medium, while a significant amount of X-ray absorbing material could also be in molecules. It is not uncommon for higher Galactic latitudes that the gas and molecular columns are comparable ($N(\mathrm{H}_2)/N(\mathrm{H})$ varies between 0.2 and 5 in the sample of Magnani et al. 1985). Finally, it cannot be ruled out that some of the excess absorption is source intrinsic and either in mildly ionized material or in material that is fast enough that narrow features are smeared out as suggested by Zoghbi et al. (2010). N_H is therefore left as a free parameter in the spectral modeling and it is not speculated on the relative fraction of source-intrinsic and Galactic absorption along the line of sight to 1H0707−495 from these fits.

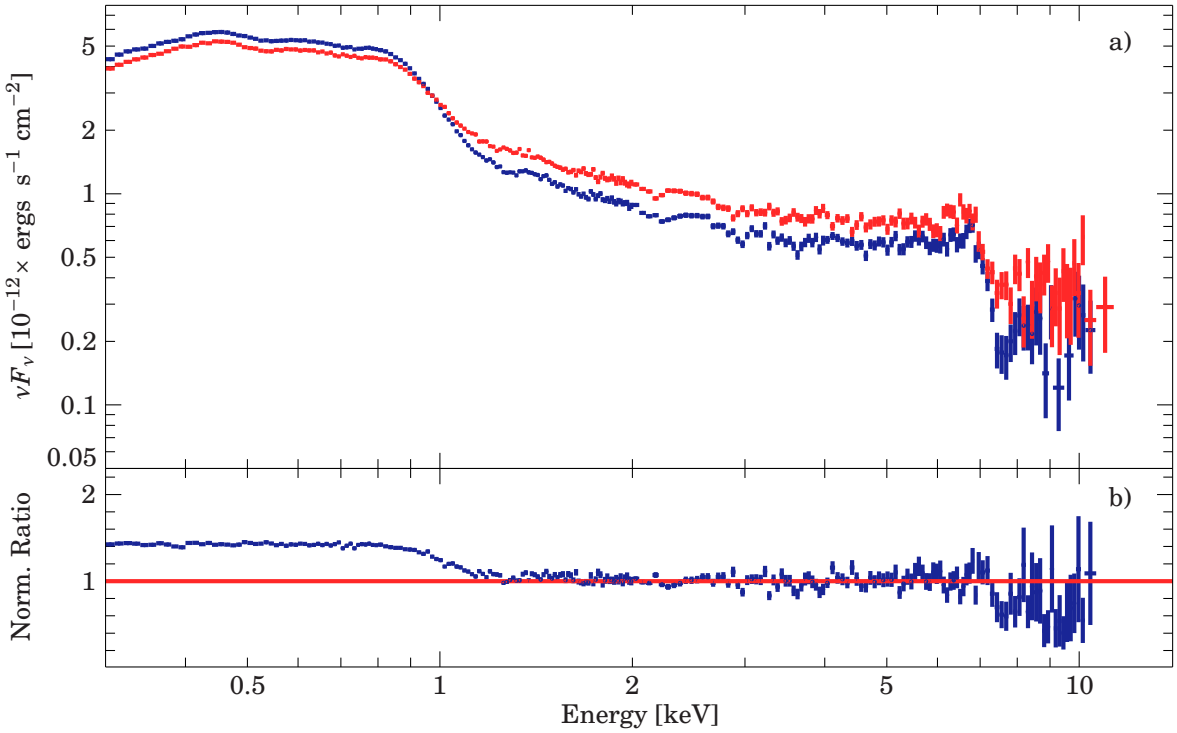

Fig. 3.6.: *(a) Unfolded spectra of Rev. 1491–1494 (red) and Rev. 1971–1974 (dark blue). The bottom panel (b) shows the ratio of the unfolded spectra (Rev. 1971–1974 divided by Rev. 1491–1494). It demonstrates that the new observation is softer, but most spectral features remain the same. For illustrative purposes the ratio spectrum was multiplied by a constant factor such that the 2–5 keV range coincides with unity. Figure taken from Dauser et al. (2012).*

3.3.5. Reflection Model

As a starting point for the detailed modeling of the spectrum the single reflection model as proposed as best-fit model by Fabian et al. (2009) and Zoghbi et al. (2010) was used. This model consists of ionized reflection from an accretion disk (`reflionx`, Ross & Fabian, 2005; Ross & Fabian, 2007), which is relativistically smeared using the `relconv` model (Dauser et al., 2010). In addition, a weak disk blackbody with $kT_{\rm in} \sim 100\,$eV was added to describe the soft-excess.

In this model, relativistic smearing is parametrized using the emissivity law $\epsilon(r)$ of the accretion disk, which describes the radius-dependent reflected power of the accretion disk per unit area incident on the disk according to $I \propto r^{-\epsilon}$ (see Chapter.2 and Dauser et al., 2010, 2013). Initially, $\epsilon(r)$ was described by a broken power law. Extensive spectral analysis showed, however, that the parameters for describing such an emissivity, two spectral indices and the break radius, were only poorly constrained when allowed to vary freely. As suggested for 1H0707−495 by Wilkins & Fabian (2011) and Fabian et al. (2012b) and for Narrow Line Seyfert 1 Galaxies in general by Ghisellini et al. (2004), the lamp post geometry is again used to constrain the emissivity. Therefore the height of the primary source determines the emissivity profile, as explained in detail in Chapter 2. As the emissivity in the lamp post geometry can also be approximated by a broken power law to $0^{\rm th}$ order (see, e.g., Fig. 11 of Fabian et al., 2012b, and again Chapter 2), any good fit in the lamp post geometry was easily reproduced with an equally good one for a broken power law emissivity. Therefore these power law indices will be given explicitly for the most important results in the following. Similar to previous analysis (e.g., Zoghbi et al., 2010), the accretion disk was assumed to

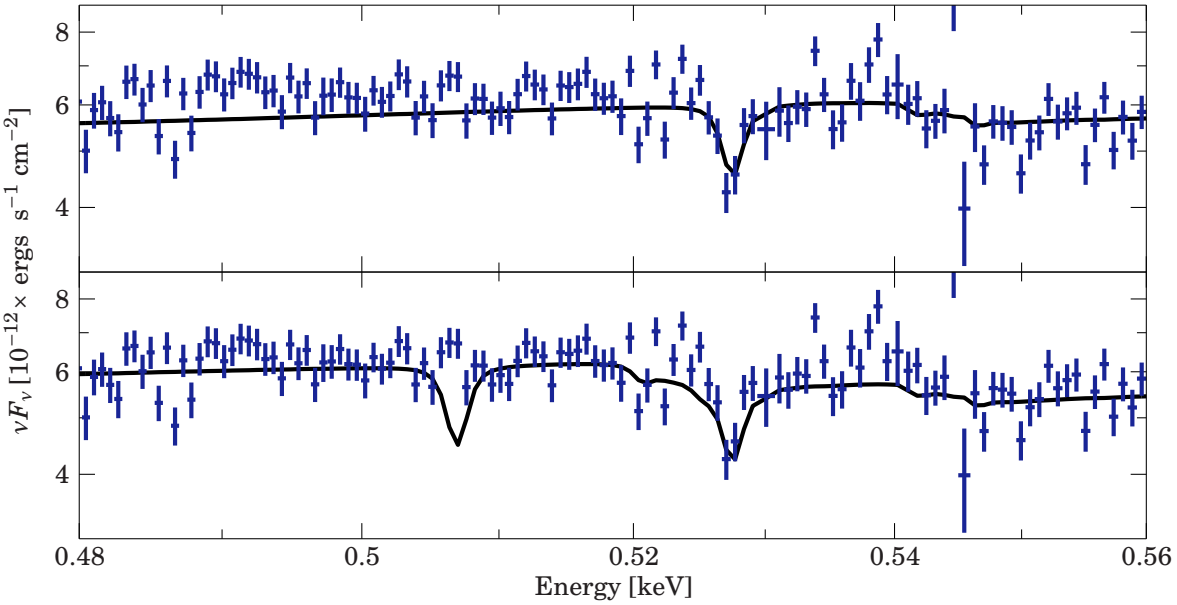

Fig. 3.7.: *The EPIC-pn best-fit applied to the RGS spectra of Rev. 1971–1974 and focusing on the* O I *(0.527 keV) absorption line. The upper panel shows the best-fit model for Galactic absorption only. The absorption line is clearly seen in the data. Residuals from a better fit including source intrinsic absorption (*z = 0.04057*) are shown in the lower panel. The lack of a redshifted* O I *line at 0.506 keV in the measured spectrum shows that the additional neutral absorption is not source intrinsic. Figure taken from Dauser et al. (2012).*

extend from the innermost stable circular orbit out to 400 r_g.

This model presented above is capable of roughly describing the data (χ^2/dof = 359/220 ~ 1.63 and χ^2/dof = 503/214 ~ 2.35 for Rev. 1491–1494 and Rev. 1971–1974, respectively), with relativistic parameters for both observations being similar to Zoghbi et al. (2010). Figure 3.8b shows the corresponding fit and residuals, Table 3.1 lists the best-fit parameters. Note that the best-fit values of height and inclination for Rev. 1491–1494 differ significantly from those values obtained in the other models. However, there exists some degeneracy between the best-fit values for these parameters, as the model only roughly describes the data. Therefore the fit is found to be almost as good, when the height and inclination are fixed to the best-fit values obtained for the other fits.

Especially for Rev. 1971–1974, the sharp drop in the spectrum at ~7 keV is not well modeled by a single reflection. Using a second reflection component, which is highly ionized, significantly improves the fit ($\Delta\chi^2$(Rev. 1971–1974) = 64, Fig. 3.8c). This second reflection component acts as an additional layer on top of the moderately ionized component, i.e., the reflectors are not radially separated. In this composite model, emission from the highly ionized reflection component at low energies describes the soft excess, i.e., an additional blackbody component is not required, while the low ionized reflection with strong Kα emission line accounts properly for the strong drop in flux around 7 keV.

Even in this two component reflection fit, however, some residuals remain in the area around ~1 keV, especially for Rev. 1971–1974. These residuals can be described by a highly ionized ($\log(\xi) \sim$ 3.5) and a smeared outflow, modeled here using the `swind` model (Gierliński & Done, 2004, see Fig. 3.8d and green line in Fig. 3.8a). Particularly for Rev. 1971–1974, such an absorption improves the fit a lot ($\Delta\chi^2$ = 165). Moreover, the blue-shifted absorption of Fe XXV and Fe XXVI at 6.7 keV and 7.0 keV is automatically predicted at the position of the prominent absorption feature

at ~7.5 keV seen directly below the sharp drop. The `swind` model describes the remaining residuals in a satisfactory manner, with outflow velocities of $0.18 \pm 0.01\,c$ and $0.11 \pm^{+0.01}_{-0.02}\,c$ for Rev. 1971–1974 and Rev. 1491–1494, respectively, calculated from the determined redshift parameter $z_{\texttt{swind}}$ (see Tab. 3.1). Winds at these speeds are commonly seen in many sources (see, e.g., Tombesi et al., 2010). This result will be discussed in greater detail below (Sect. 3.3.7). In addition, the smearing due to a turbulent velocity is in the order of 0.01–0.02 c, i.e., 3000–6000 km s^{-1}, which is in agreement with the gratings spectrum (see Sect. 3.3.4). Despite this overall success of the model, however, the predicted strength of these lines is too weak. This weakness is a limitation of the `swind` model, which is constrained to material of Solar abundances and does not allow us to model these lines using the extreme metallicity indicated by the reflection component.

Despite the large uncertainties, at each point above 7 keV in Rev. 1971–1974 there is a systematic over-prediction of the flux (see Fig. 3.8d, right). It probably originates from improperly modeled accretion disk reflection; in particular, contributions from the lower ionized component contribute to a large amount of the total flux observed in this energy range (see Fig. 3.8a). As will be discussed in detail in Sect. 3.3.8, the modeling of the reflection suffers from several constraints. For example, the simplified modeling of the accretion disk spectrum, or the fact that Fe is highly over-abundant while all other elements are at Solar abundance, could easily produce an over-prediction of the model flux above 7 keV. In addition to that, the mildly ionized wind can only be modeled assuming Solar composition, too, although the reflection component strongly suggests that Fe is highly over-abundant. It is therefore expected that the model under-predicts the absorption by H-like and He-like transitions of iron in the energy range around 7 keV.

3.3.6. Alternative Models: Smeared Absorption

As an alternative to the "pure" reflection model, the model proposed by Gierliński & Done (2004) was also tried to fit to the data, which models the soft-excess by a strongly ionized and ultra-fast outflow. As discussed in Sect. 3.3.4, there are no narrow lines present in the RGS spectrum of 1H0707−495. Therefore the `swind` model is again used to describe the smeared absorption. Figure 3.9 shows that this model together with a single reflection component is capable of describing the data. Compared to the residuals in Fig. 3.8, however, the emission-like hump around 0.9 keV is much more pronounced. In order to work, the model requires an outflow velocity of $\sim 0.37\,c$ of the absorbing material, which is larger than most relativistic outflows observed in Active Galaxies (see, e.g., Blustin et al., 2005; Tombesi et al., 2010). More doubtful is that in order to explain the data a line broadening with a rms velocity distribution of as high as 50000 km s^{-1} has to be assumed. From a statistical point of view, however, this model cannot be completely rejected ($\chi^2/\mathrm{dof} = 375/226 \sim 1.66$ for Rev. 1971–1974).

Finally, as argued by Zoghbi et al. (2010), if the spectral drop was due to a partially covering absorber a strong neutral K-line would be expected. For the upper limit search the summed *Chandra* HETG spectrum is used without applying any further binning. With these observations we are able to determine the upper limit of the flux of a narrow ($\sigma = 1$ eV) Gaussian line at 6.4 keV to $F_{6.4} < 2.0 \times 10^{-6}$ photons s^{-1} cm^{-2} at 90% confidence. This upper limit is consistent with our EPIC-pn spectral modeling, but does not allow to constrain the modeling further. The absence of this line again argues against the absorption interpretation.

3.3.7. A highly ionized outflow in 1H0707−495

As shown in Dauser et al. (2012), the data presented above harbors information about a highly ionized outflow in 1H0707−495. The detailed discussion taken from Dauser et al. (2012) will be

Tab. 3.1.: *Best-fit models, as shown in Fig. 3.8: Model 1 is a power law, a single broadened reflection component and a blackbody. Model 2 consists of two reflection components of different ionization parameter, ξ, and Model 3 is the best-fit model, based on Model 2 combined with absorption of radiation in a highly ionized wind. The ionization parameter is defined as $\xi = 4\pi F/n_e$, with flux, F, and electron number density, n_e. The parameter v_{swind} is the velocity dispersion of the wind and z_{swind} its redshift compared to the rest frame. Note that in most models, the iron abundance relative to Solar in the* `reflionx` *component, Z_{Fe}, pegs at the upper limit of $Z_{Fe} = 20$, while all other elemental abundances are fixed to Solar. Table adapted from Dauser et al. (2012).*

	Model 1 (Single Refl.)		**Model 2** (Double Refl.)		**Model 3** (Double Refl. + Wind)	
	Rev. 1491–1494	Rev. 1971–1974	Rev. 1491–1494	Rev. 1971–1974	Rev. 1491–1494	Rev. 1971–1974
$A_\Gamma \times 10^{-3}$	$0.958^{+0.017}_{-0.029}$	$0.727^{+0.013}_{-0.014}$	$1.093^{+0.023}_{-0.031}$	$0.836^{+0.018}_{-0.020}$	$1.182^{+0.030}_{-0.027}$	$0.913^{+0.024}_{-0.025}$
Γ	$2.575^{+0.032}_{-0.022}$	$2.609^{+0.025}_{-0.020}$	$2.86^{+0.04}_{-0.05}$	2.91 ± 0.04	$2.86^{+0.05}_{-0.04}$	$2.853^{+0.027}_{-0.025}$
$A_{refl_1} \times 10^{-5}$	$0.096^{+0.032}_{-0.025}$	$0.088^{+0.026}_{-0.016}$	$2.0^{+0.6}_{-0.5}$	$2.7^{+0.7}_{-0.4}$	$3.6^{+0.4}_{-1.4}$	$4.8^{+0.6}_{-2.0}$
$A_{refl_2} \times 10^{-5}$	-	-	$0.0058^{+0.0018}_{-0.0010}$	$0.0111^{+0.0013}_{-0.0010}$	$0.0056^{+0.0010}_{-0.0007}$	$0.0048^{+0.0013}_{-0.0008}$
$\log(\xi_{Refl_1})$	$1.965^{+0.059}_{-0.030}$	$2.074^{+0.027}_{-0.022}$	$1.301^{+0.014}_{-0.148}$	$1.301^{+0.010}_{-0.109}$	$1.00^{+0.14}_{-0.00}$	$1.004^{+0.251}_{-0.004}$
$\log(\xi_{Refl_2})$	-	-	$2.995^{+0.012}_{-0.115}$	$3.000^{+0.004}_{-0.051}$	$3.000^{+0.027}_{-0.081}$	$3.301^{+0.006}_{-0.118}$
Z_{Fe}	$19.73^{+0.28}_{-11.54}$	$20.0^{+0.0}_{-1.0}$	$10.3^{+3.4}_{-2.5}$	$12.0^{+2.8}_{-2.5}$	15 ± 5	20^{+0}_{-6}
h^{lp} [r_g]	29^{+8}_{-5}	$3.0^{+0.6}_{-0.0}$	$3.13^{+0.71}_{-0.13}$	$3.00^{+0.28}_{-0.00}$	$3.0006^{+0.3372}_{-0.0006}$	$3.00^{+0.13}_{-0.00}$
a^{lp}	$1.0^{+0.0}_{-1.2}$	$0.971^{+0.016}_{-0.017}$	$0.998^{+0.000}_{-0.009}$	$0.9980^{+0.0000}_{-0.0023}$	$0.998^{+0.000}_{-0.008}$	$0.998^{+0.000}_{-0.011}$
θ^{lp} [deg]	$77.7^{+2.3}_{-4.8}$	$58.4^{+0.9}_{-1.3}$	$48.8^{+1.4}_{-1.9}$	48.8 ± 1.0	$52.0^{+1.7}_{-1.8}$	$48.8^{+1.3}_{-1.2}$
N_H [10^{22} cm^{-2}]	$0.070^{+0.019}_{-0.009}$	0.082 ± 0.010	$0.052^{+0.004}_{-0.005}$	$0.0589^{+0.0024}_{-0.0025}$	$0.0545^{+0.0027}_{-0.0030}$	$0.0628^{+0.0025}_{-0.0028}$
$A_{bb} \times 10^4$	$0.59^{+1.07}_{-0.19}$	$1.7^{+1.0}_{-0.7}$	-	-	-	-
kT_{bb} [eV]	112^{+8}_{-17}	96^{+7}_{-6}	-	-	-	-
N_H^{swind} [10^{22} cm^{-2}]	-	-	-	-	$3.6^{+7.0}_{-0.6}$	$4.0^{+1.3}_{-1.0}$
$\log(\xi_{swind})$	-	-	-	-	$3.61^{+0.17}_{-0.07}$	$3.299^{+0.024}_{-0.071}$
v_{swind} [c]	-	-	-	-	≤ 0.025	≤ 0.014
z_{swind}	-	-	-	-	$-0.063^{+0.015}_{-0.007}$	$-0.1262^{+0.0015}_{-0.0036}$
χ^2/dof	$359/220 = 1.63$	$503/214 = 2.35$	$290/220 = 1.32$	$439/214 = 2.05$	$237/216 = 1.10$	$274/210 = 1.31$

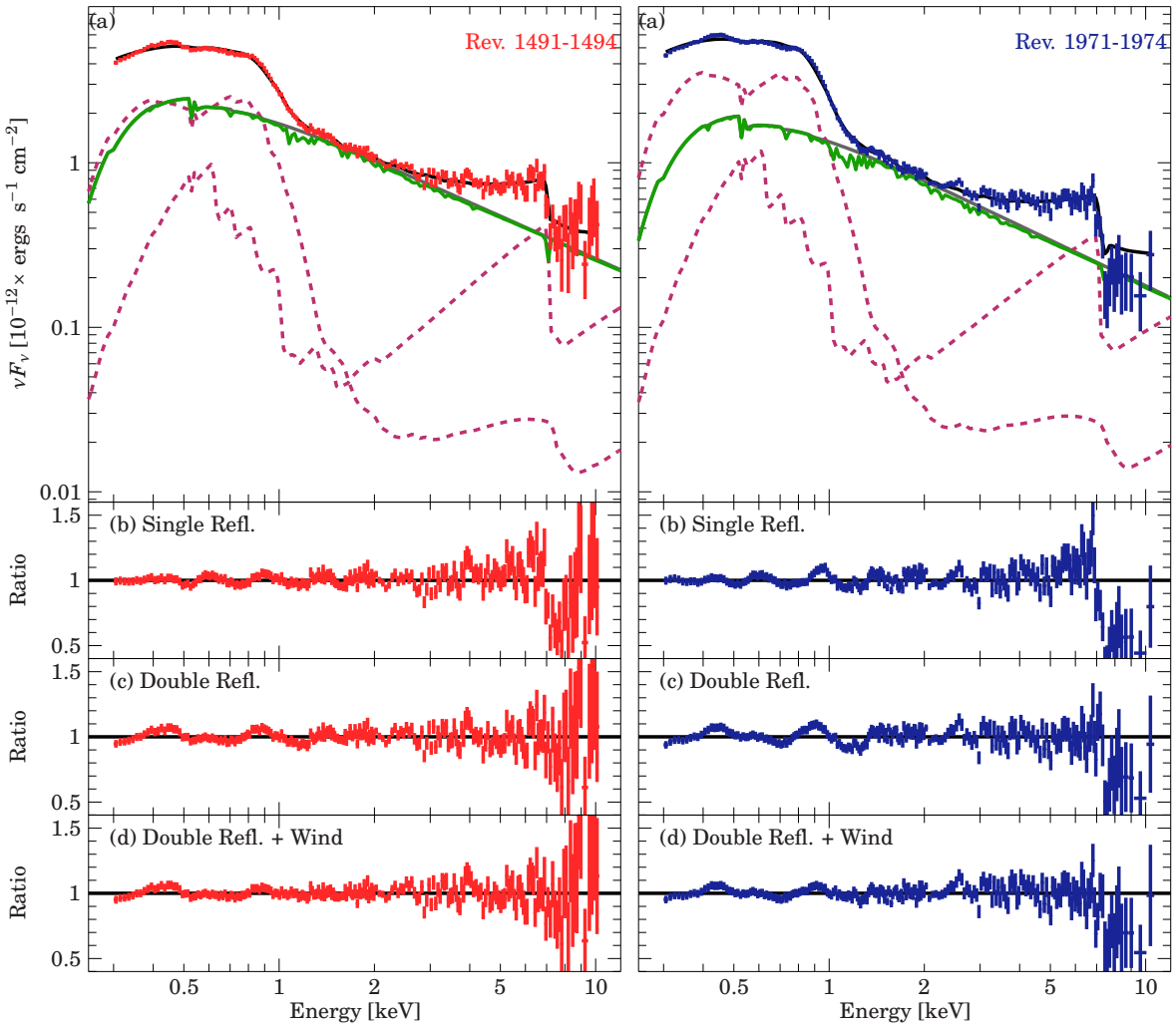

Fig. 3.8.: *Best-fit model of Rev. 1491–1494 (left) and Rev. 1971–1974 (right). (a) The upper panel shows the best-fit model components: Two relativistic reflection components (purple, dashed) and a power law (dark gray), absorbed by a highly ionized and blue-shifted outflow (green). The lower panels show the residuals of (b) a single reflection component, (c) two reflection components, and (d) the best-fit model with additional absorption by an ionized wind. This figure is taken from Dauser et al. (2012).*

given in verbatim in the following. Generally, a highly ionized and fast outflow was already used by Done et al. (2007) to describe the spectrum of 1H0707−495, where strong absorption in this wind models the complete spectral shape, including the sharp drop at ~7 keV as a P Cygni line. In contrast, in our best-fit model the main spectral features (the soft-excess and the sharp drop) are described by reflection, while the wind, being more ionized, has a smaller influence on the observed spectrum. We saw in Sect. 3.3.5 that a major difference between Rev. 1491–1494 and Rev. 1971–1974 is a difference of ~0.07 c in wind velocity. Comparing the two spectra for the higher energetic range (Fig. 3.10a) reveals that of all the structure seen in this energy band only the steep drop around ~7 keV agrees in both observations. This constancy is expected if the 7 keV feature is due to a relativistic line emitted from an accretion disk. If one wanted to explain the full spectrum by absorption, however, it would be very unlikely that all spectral features except for the drop

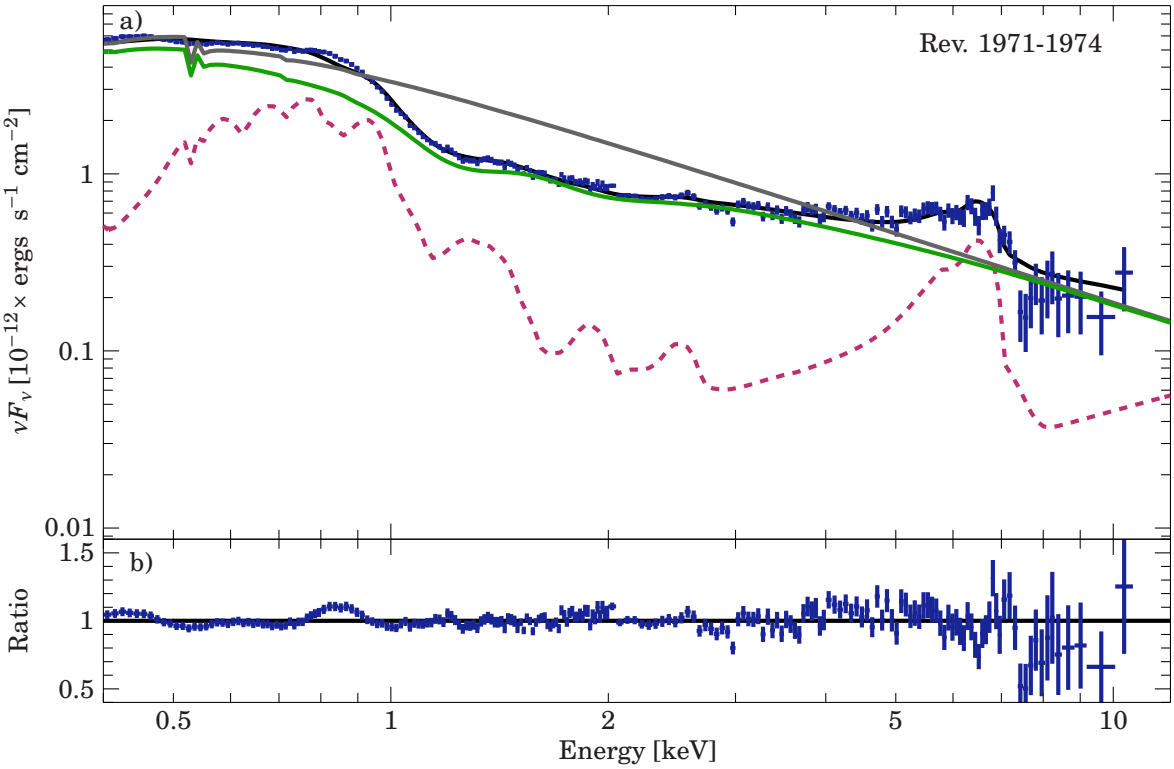

Fig. 3.9.: *An alternative model (here for Rev. 1971–1974) which describes the soft-excess as a blend of several mildly ionized* ($\log(\xi) \sim 2.2$) *and smeared Oxygen absorption lines. (a) Single components: The effect of the absorption on the original power law (dark gray) is illustrated by the green line and the reflection component is shown by the purple, dashed line. (b) Residuals of the best-fit* ($\chi^2/\mathrm{dof} = 375/226 \sim 1.66$). *Figure taken from Dauser et al. (2012).*

change their location and that only the strongest feature stayed constant.

Taking a closer look at the spectra away from the 7 keV feature reveals that indeed the same features appear in both observations, but they are slightly shifted in energy. Correcting for this shift "by eye", Fig. 3.10b shows that most features agree nicely if the shift is approximately

$$\Delta z = z_{\mathrm{Rev.19}} - z_{\mathrm{Rev.14}} \sim -0.045 \quad . \tag{3.1}$$

This relative shift is consistent with the difference in redshift found between the two swind components obtained by spectral modeling, $\Delta z_{\mathtt{swind}} = -0.06^{+0.01}_{-0.02}$. We can therefore attribute the fine spectral structure between 2–5 keV to a fast and highly ionized outflow.

Assuming redshifts of $z_{\mathrm{Rev.14}} = -0.04$ and $z_{\mathrm{Rev.19}} = z_{\mathrm{Rev.14}} + \Delta z = -0.085$, the structures in the spectrum can tentatively be identified with single 1s-2p transitions of H-like Si, S, and Ca (see Fig. 3.10b). Again, the individual redshifts found by eye agree with the ones found in our spectral fits for the two swind components, $-0.06^{+0.02}_{-0.01}$ and -0.13 ± 0.01. In such a highly ionized plasma we would also expect a strong resonant transition from Argon. Inspection of the Ar band reveals a feature that is more complex than the absorption features in the Si, S, and Ca band, making its interpretation difficult at the resolution of an X-ray CCD. A possible explanation could be a P Cyg profile of H-like Ar, however, in this case Ar would have a different redshift than the other features, which seems unlikely. Note, however, that the overall shape of this feature remained stable between both observations. Further modeling of the spectral features using proper wind

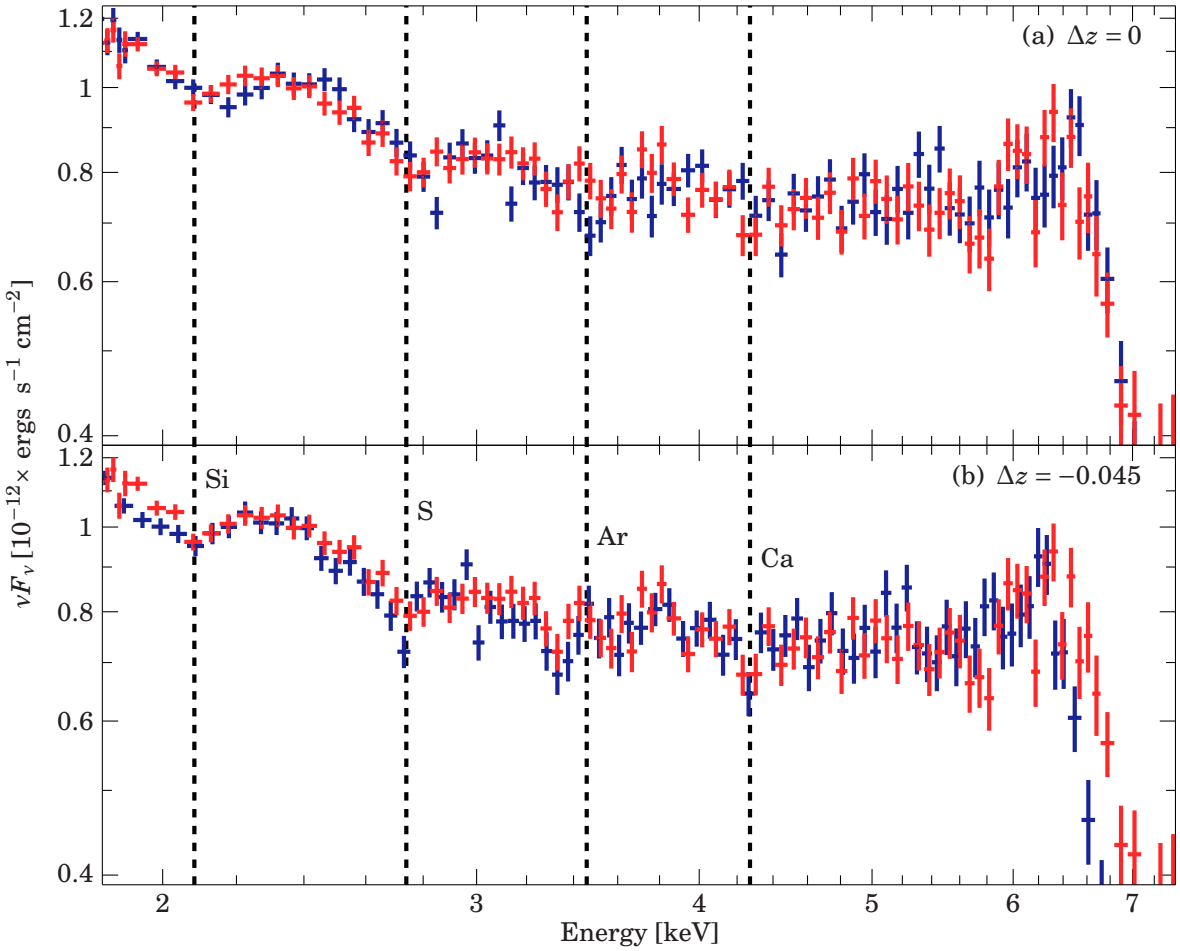

Fig. 3.10.: *(a) A zoom into the hard X-ray bandpass of the spectra: For illustrative purposes Rev. 1971–1974 (dark blue) is renormalized to the same νF_ν in the 2–5 keV band as Rev. 1491–1494 (red). Energies are given in the rest frame of the source. (b) Here we apply a manual energy shift to Rev. 1971–1974 (blue) corresponding to a redshift of $\Delta z = z_{\mathrm{Rev.\,19}} - z_{\mathrm{Rev.\,14}} = -0.045$, which leads to the best agreement for most absorption-like features that are seen consistently in both observations. The most prominent of these features are indicated by dashed lines. Assuming an outflow velocity in Rev. 1491–1494 of ∼0.04 c they can be attributed to 1s-2p transitions of H-like Si, S, Ar, and Ca. Figure taken from Dauser et al. (2012).*

models is therefore required to understand the details of these features.

3.3.8. Discussion of the Results

In this section the results from a spectral analysis of 500 ksec of new *XMM-Newton* and *Chandra* data from the AGN 1H0707−495 have been presented and compared to the previous long observation of the source. All of this work is presented in detail in Dauser et al. (2012). In agreement with earlier work (Fabian et al., 2009, 2012b; Zoghbi et al., 2010), the simple picture for 1H0707−495 deduced from these observations is that an accretion disk around a maximally rotating black hole is irradiated by a central and compact source closely above the black hole, producing the underlying complex X-ray continuum by reflection. In both observations, the primary X-ray source which

irradiates the accretion disk has a height of $\leq 4\,r_g$ above the black hole. Such a low emitter is in line with timing measurements (Zoghbi et al., 2010) and implies that the photons are extremely focused onto the inner parts of the disk. Note that this is, again, in very good agreement with the theoretical predication that only reliable spin estimates can be made for compact primary sources close to the black hole (see Chapter 2 and Dauser et al., 2013; Fabian et al., 2014). Fits with an empirical broken power law emissivity confirm this interpretation ($\epsilon_{r<r_{br}} = 10.2^{+0.8}_{-0.9}$, $\epsilon_{r>r_{br}} = 2.3^{+0.5}_{-0.1}$, $r_{br} = 2.9^{+0.2}_{-1.0}\,r_g$ for Rev. 1971–1974). Despite significant changes in the continuum shape between both observations, the black hole in 1H0707−495 is consistently well determined to be maximally rotating. Similar to the results obtained for Cygnus X-1 in the previous section, this finding again adds further credibility to the relativistic line interpretation of the spectrum, as the black hole parameters are not expected to change on such short time scales. Such a behavior would be significantly more difficult to explain in alternative models explaining the line via an ionized and blue-shifted radial wind. Interestingly, the highly ionized wind component that is found in addition to the reflection component indeed changes in between the two *XMM-Newton* observation.

The accretion disk causing the observed reflection features has a complex ionization structure, which is here approximated by two reflectors of strongly different ionization as modeled by Ross & Fabian (2005) and Ross & Fabian (2007). Even though the highly ionized reflector dominates the soft X-ray spectrum, its normalization is only 0.1–0.2% of that of the weakly ionized reflector, i.e., most of the irradiated X-rays are intercepted by the colder medium. This result fits nicely into the picture of a rather neutral accretion disk with a thin skin of highly ionized material caused by the incident X-rays (see, e.g., García & Kallman, 2010; García et al., 2011). As a caveat, however, note that this approach implicitly assumes that the ionization fraction of the disk is independent of distance from the black hole. From basic arguments it is clear that the patronization due to the incident X-rays will result in an ionization structure of the disk surface which strongly depends on radius, as even in the simplest and most conservative models photons are strongly focused towards the inner parts. Additionally, the energy release within the accretion disk itself will give rise to a temperature and ionization gradient (e.g., Hubeny et al., 2001; Davis et al., 2005, and references therein). Hence, the special reflection spectrum of 1H0707−495 makes this source a perfect candidate to test a relativistic reflection model including such an ionization gradient. Note that in the outlook (Sect. 5.3.2) a brief sketch and first results of such a model is given. As for some parameter combinations (see Fig. 5.4) a very steep gradient is expected, the approximation of the ionization in the accretion disk by only two different values of ionization could also be explained within this more physical approach. However, a detailed examination of the ionization gradient is necessary to draw firm conclusions.

As shown by our modeling of the weaker spectral features, the relativistically blurred continuum is then modified by absorption in an ultra-fast wind (0.11–0.18 c, i.e., 30000–50000 $\mathrm{km\,s^{-1}}$). Due to the change of the minor features at 2–5 keV and the constancy of the 7 keV drop between the two observations (see 3.3.7), the ionized wind could be uniquely identified to exist along with the reflection, which dominates the spectrum. The overall properties of this wind are in line with the relativistic, highly ionized winds that have now been detected in more than 40 radio-quiet AGN, including Narrow Line Seyfert 1 galaxies. These winds have been mainly detected through strongly redshifted Kα and Kβ absorption lines from H- and He-like iron. See, e.g., Chartas et al. (2002), Pounds et al. (2003), Turner et al. (2004), or Cappi et al. (2009) for discussions of individual sources and Tombesi et al. (2010) for a recent comprehensive study with *XMM-Newton*.

Radiation hydrodynamical calculations show that such winds can in principle be formed as line driven winds from an accretion disk (Proga et al., 2000; Kurosawa & Proga, 2009, and references therein). The spectral signature imprinted on the X-ray continuum are in rough agreement with the features seen here (e.g., Schurch et al., 2009), although further theoretical work such as proper

inclusion of Compton broadening is clearly needed (e.g., Sim et al., 2010). Unfortunately, the current wind models available for X-ray spectral modeling also do not yet allow us to self-consistently model absorption with abundances consistent with the significant overabundance in the accreted material inferred from the X-ray reflection. Despite this problem, however, the agreement between our simple wind model and the data is remarkable. Interestingly the measured outflow velocity is also consistent with the unified model for quasars proposed by Elvis (2000), where a "Warm Highly Ionized Medium" is ejected at speeds of 10000–60000 km s^{-1} at an inclination of around 60°. Coincidentally, this value is in agreement with our best-fit inclination angle. Note that in order to explain the apparent shift of minor spectral features in the 2–5 keV band, the line of sight velocity of this wind must have changed between both observations. As such a wind is expected to be highly structured (Sim et al., 2010), only very slight changes in the line of sight would be required to explain the observed change in velocity.

Despite the overall success of the modeling, however, some significant broad residuals remain (Fig. 3.8d). There are several major issues which could explain these discrepancies that could not be treated properly in this analysis due to limitations of our best-fit model (Sect. 3.3.5). First of all, while measurements of the reflection show a high Fe abundance in reflection, all other elements are assumed to be of Solar abundance. From basic arguments it is clear that a high Fe abundance likely implies that other elements are over-abundant as well, which could not be taken into account in this approach due to the limitations of the reflection models[5]. Such a restriction might therefore underpredict emission from other elements, while at the same time over-predict the Fe abundance. Improving on modeling the ionization gradient in the accretion disk as discussed above could also slightly reduce the artificially high Fe abundance obtained from fitting the data with simple reflection models (Reynolds et al., 1995). As already discussed by Zoghbi et al. (2010), however, NLS1 galaxies such as 1H0707−495 exhibit enhanced star formation (Sani et al., 2010) and therefore are expected to be Fe enriched. This assumption is confirmed in near-IR measurements (see, e.g., Shemmer & Netzer, 2002). Moreover, in similar sources like MCG−6-30-15 (Miniutti et al., 2007), 1H0419−577 (Fabian et al., 2005), or IRAS13224−3809 (Ponti et al., 2010) iron is also required to be over-abundant. Finally, the newest results obtained with the `relxill` model (see Sect. 4.1 and García et al., 2014), which include for the first time a proper treatment of the angular dependency of the reflected radiation, will be shown to have a large effect on the iron abundance inferred by common relativistic convolution models (see Sect. 4.2, Fig. 4.7). For the presented results of 1H0707−495 this means that the iron abundance obtained by fitting the reflection with `reflionx` convolved by `relconv` might be over-estimated by 50–70 % (see Tab. 4.1).

Regarding the ionized wind seen in absorption, a lower wind velocity and $N_{\rm H}$ is measured compared to earlier absorption dominated models (Gallo et al., 2004; Done et al., 2007). This difference is probably due to the fact that in earlier models the full continuum was seen to be dominated by the wind, while in the present model the soft-excess is mainly described by reflection of a highly ionized accretion disk. This interpretation is in line with the identification of weaker spectral features as absorption lines from H-like ions (Si, S, Ca, and possibly Ar), which are found at the correct energies expected from the inferred wind velocities. As discussed above, since the 7 keV feature is non variable, it cannot be due to the wind. This result significantly simplifies the wind modeling, as in order to explain the whole 7 keV feature as a wind a very complex absorber is necessary (see also Done et al., 2007, note, however, that the ionized and blue-shifted absorption is required to describe the narrow absorption feature right above the drop).

[5] `reflionx` as well as `xillver` only allow the Fe abundance to change. Including different abundances for additional elements requires a large computational effort and would result even larger tables. For each element included additionally, the effort and the required memory space increases by approximately factor of 5 to 10. Hence, taking already almost 1 GByte of space, it is simply not feasible to include more than one additional element in `xillver`.

CHAPTER 4

THE RELXILL MODEL: COMBINING REFLECTION AND RELATIVITY

The case study of 1H0707−495 and Cygnus X-1 in Chapter 3 both showed that a relativistically convolved reflection spectrum does model and constrain the relativistic reflection in GBHs and AGN very well. Besides the relativistic smearing, which was extensively treated in Chapter 2, the intrinsic reflection spectrum is also of great importance. This chapter is therefore dedicated to the marriage of the reflection code `xillver` with the relativistic kernel `relline` and its significant improvements to previously available models.

4.1. THE RELXILL MODEL

As has been shown in García et al. (2013), the generally used `reflionx` model exhibits several problems and is for the newest generation of X-ray satellites such as *NuSTAR* at its limit. In the following the `xillver` model will therefore be used. Concerning the non-relativistic reflection at an ionized accretion disk the `xillver` model is currently the best suitable model available. First presented by García & Kallman (2010) and García et al. (2011), it is similar to the popular reflection code `reflionx`, which was successfully used in many studies (see Chapter 3 and, e.g., Reis et al., 2008; Zoghbi et al., 2010; Duro et al., 2011; Dauser et al., 2012; Fabian et al., 2012b; Risaliti et al., 2013). The major improvement of `xillver` comes from the usage of the largest collection of atomic data for X-ray astronomy, namely the `xstar`[1] atomic database (Bautista & Kallman, 2001). In a recent update, we presented important improvements regarding new atomic data and the input spectrum, along with a thorough comparison to previous models such as `reflionx` (García et al., 2013). This newly presented code is explicitly used to calculate a complete grid of reflection spectra for the typical ranges of parameters commonly found in observations (power law index, $1.2 \leq \Gamma \leq 3.4$; ionization parameter, $1 \leq \xi \leq 10^4$; iron abundance, $0.5 \leq A_{\mathrm{Fe}} \leq 10$). More details regarding non-relativistic reflection and the implementation of the `xillver` code, can be found in García et al. (2013). The simulation is stored in a table[2] and can be used directly for data analysis in common X-ray data analysis tools, like ISIS or XSPEC.

In the following the `xillver` reflection code will be used as a basis to create the new relativistic reflection model `relxill` by combining it with the relativistic smearing kernel of `relline` (Dauser et al., 2010, 2013). This new model, being the first angular resolved model for relativistic reflection, is presented in García et al. (2014). Besides enhancing the usability, directly combining the

[1] See `http://heasarc.gsfc.nasa.gov/xstar/xstar.html` for more information.
[2] Download at `http://hea-www.cfa.harvard.edu/~javier/xillver/`.

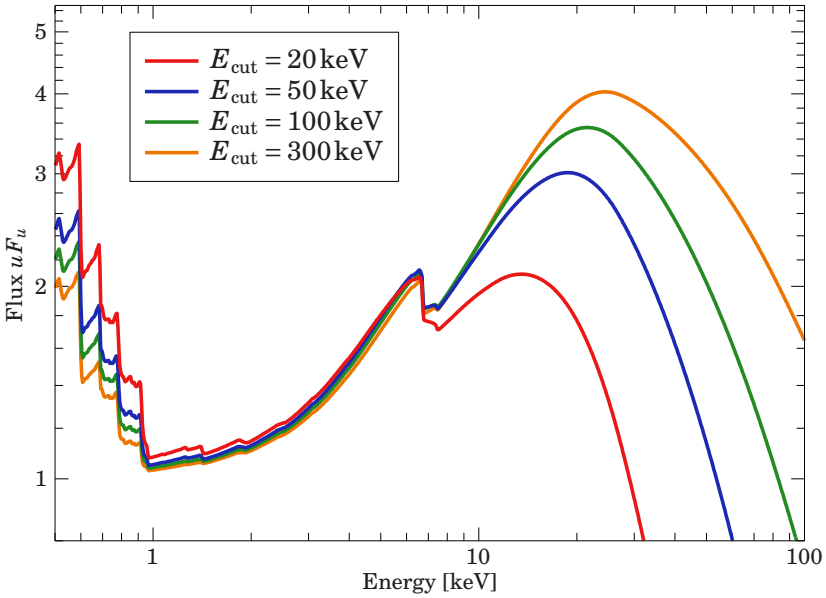

Fig. 4.1: *Sample spectra of the* `relxill` *model for different cutoff energies* $E_{\rm cut}$*, as indicated in the figure. Standard values for the other parameters were chosen:* $\Gamma = 2$*, almost neutral disk* ($\log\xi = 1$)*, low source height* ($h = 3\,r_{\rm g}$)*, high spin* ($a = 0.998$)*, inclination* $\theta = 30°$*, and iron abundance* $A_{\rm Fe} = 1$*.*

reflection and the relativistic kernel has two important improvements. Namely a proper angular treatment of the reflected radiation (Sect. 4.2, García et al., 2013) and a direct constraint on the reflection fraction (Sect. 4.3, Dauser et al., 2014). As will be explicitly demonstrated in the following, separately modeling reflection and relativistics (as, e.g., also used in Chapter 3) does not allow to take these effects into account. `relxill` is the first model, which incorporates these effects.

Besides the direct combination of reflection and relativistic convolution, no other assumptions enter the `relxill` model. Actually, it exhibits even less free parameters, as the `limb` parameter is now superficial as it is calculated self-consistently from the reflection (see Appendix A). However, a parameter called `angleon` was added to switch between the new approach (`angleon=1`) and the previous, angle-averaged approach (`angleon=0`). Clearly, this parameter should only be set to 0, in order to directly compare the `relxill` model to older observations, as taking the angular effects into account is more correct in any case. Again, similar to `relline` (see Dauser et al., 2010; Dauser, 2010), the `relxill` model is designed to be used in common X-ray data analysis tools (like `isis` or `xspec`). Further information on the model, the single parameters, and the different flavors is given in the appendix.

Similar to the `relline` model, `relxill` is able to describe the standard coronal geometry with an empirical broken power law emissivity, but also incorporates the lamp post geometry. In the latter case the model is called `relxilllp`. As mentioned above, aside from the angular directionality, a parameter called the *reflection fraction* R was introduced in the model. It is defined as the ration between the reflected and the directly observed flux. Technically, it means that an additional power law component is now automatically included.[3] Besides fitting the reflection fraction, the lamp post flavor of the model (`relxilllp`) also allows to fix R, freezing the normalization between direct and reflected spectrum to the value that is directly predicted from the lamp post geometry. Note, however, due to slight differences in the geometry of the source this strict connection does not necessarily have to be true. Therefore the model also provides the possibility to only display the predicted value of the reflection fraction, in order to compare how far the theoretical value differs from the observed one (see Appendix A for further information).

[3] Note, however, that similar to the `pexrav` model, the direct radiation can be switched of by setting R to a negative value.

Moreover, the new xillver table model allows a variable cutoff energy from 20–300 keV. This dependency is also implemented in the new relxill model. Especially since the *NuSTAR* X-ray satellite is able to well resolve and measure the cutoff energy (see, e.g., the recent measurement by Marinucci et al., 2014), a proper description of reflection spectra exhibiting an exponential cutoff is essential. Figure 4.1 shows the effect the cutoff energy has on the over all reflection spectrum. Very importantly, not only does the cutoff shift to higher energies, but also the lower energetic part of the reflection is largely influenced. While there is only a slight change in the Fe Kα line feature itself, the main effect of the cutoff on the lower energies is to soften the spectrum for a decreasing cutoff energy. Hence, also a cutoff energy of >100 keV does influence the lower energetic parts (<10 keV), which is the energy range observed by, e.g. *XMM-Newton*. Note that there has never been a xillver model without a cutoff. Initially the cutoff was fixed at $E_{\rm cut} = 300$ keV, as is also done in the reflionx model.

4.2. Angular Effects

The following section treats the angular effects of relativistic reflected radiation at an accretion disk, focusing on the direct combination of reflection and relativity with relxill and its impact for measuring relativistic parameters. These angular effects are investigated in detail in García et al. (2014). The following section closely follows this publication, focusing on the relativistic effects of the angular dependency, which were analyzed by me.

4.2.1. Angle dependent reflection

The most commonly used reflection model for ionized accretion disks, reflionx (Ross & Fabian, 2005), does only predict angular-averaged solutions for the reflection. However, previous work on angular effects of reflected radiation (Haardt, 1993; Ghisellini et al., 1994) already showed the importance of such effects, although not treating line emission and photoelectric absorption. Using the full capabilities of the xillver model, a new grid of reflection models was calculated, taking the angular distribution into account. The exact details of the calculation can be found in García et al. (2014).

Figure 4.2 shows the simulated angle dependent spectra for different ionization states of the accretion disk. First of all, large differences to the angle-averaged spectra are evident regardless of the ionization parameter. While being over a factor of two for neutral and mildly ionized disks, the difference decreases for the largest ionizations ($\log\xi \geq 3$). A more detailed view reveals that not only the strength of the emission and absorption lines, but also the continuum strongly depends on the viewing angle onto the disk. Most interestingly, the line features behave differently than the continuum. Also the higher energetic photons, including the region around the Compton hump, are highly affected by a change in viewing angle (Lightman & Rybicki, 1980; Lightman et al., 1981; Magdziarz & Zdziarski, 1995). Due to the large number of scatterings, these high energy photons are actually affected most (García et al., 2014).

This strong angle dependence and the fact that it differs for the lines and the continuum can be explained by the change in effective optical depth. It is defined as the projection of the actual optical depth τ along the line of sight. As explained in detail in García et al. (2014), spectral features inherent to the reflection spectrum are produced at different optical depth. When viewed under gracing angle, the observed flux from elements produced at larger τ (like Fe or Ni) is weaker than from features produced closer to the surface (C, N, and O). Similarly, the angular dependence of the continuum can be explained. Also notable from Fig. 4.2 is that the angular dependence at

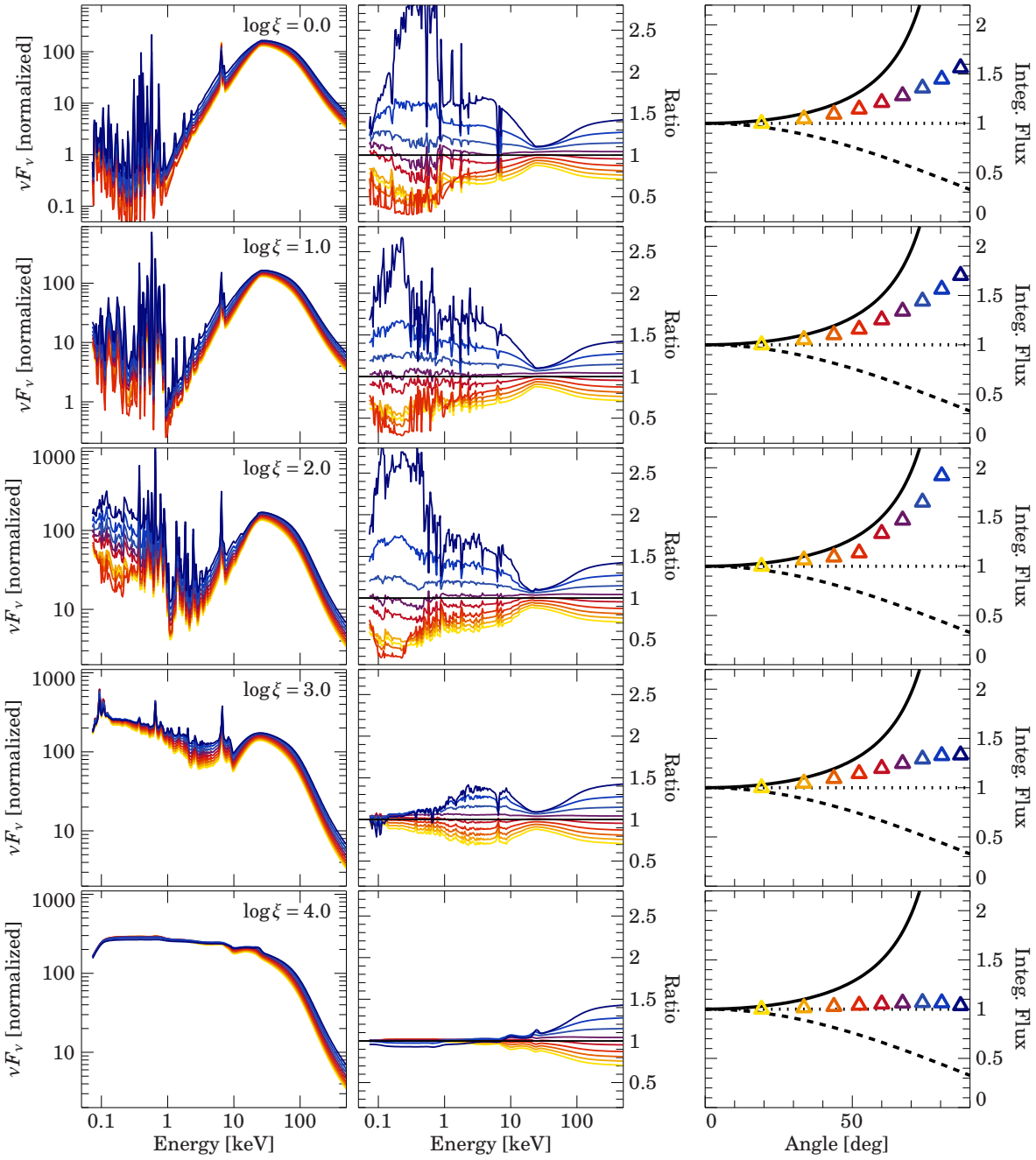

Fig. 4.2.: *Left column: Spectra for different angles calculated with the new* `xillver` *model. Middle column: Ratio between the angle-resolved spectra from the left panel and the angle-averaged spectrum. Right column: The integrated flux as depending on the viewing angle. Colors of all panels correspond to the angles as plotted in the right panel. The commonly used limb-brightening (Haardt, 1993,* $I \propto \ln(1+1/\cos\theta_e)$*) and darkening (Laor, 1991,* $I \propto \ln(1+2.06\cos\theta_e)$*) laws for relativistic smearing are indicated as solid and dashed line, respectively.*

the Compton hump and above (i.e., ≥ 20 keV) does not depend on the ionization parameter, as the main source of reflection at these energies is due to Compton scattering (García et al., 2014). Moreover, the angular effects at low energies are most pronounced for a neutral disk, as the disk opacity and therefore the photoelectric scattering is strongest for low ionization. In general, looking closely at Fig. 4.2 shows that the angle-averaged solution is closest to spectra under a viewing angle of ∼ 60°. Hence, the largest improvement of the new model are expected for either low or very high inclination systems.

As can be seen in the right panel of Fig. 4.2, a limb-brightening, i.e., an enhanced flux for larger viewing angles is predicted regardless of the ionization of the accretion disk. Generally, relativistic smearing kernels like `relconv` (see, e.g., Chapter 2 and Dauser et al., 2010) a generic limb-brightening or darkening law can be chosen, which does not depend on the energy. However, only for a mildly ionized accretion disk the actual limb-brightening law is recovered. While it already significantly differs from this law for a neutral disk, for a highly ionized accretion disk ($\log\xi \geq 3$), the emissivity becomes close to isotropic. The latter effect can be explained by the fact that the spectra in the highly ionized regime are dominated by electron scattering, which is largely independent of the viewing angle (García et al., 2014). Note that the predicted limb-brightening of the new simulation is in contrast to the common practice of older models (e.g., `kdblur` or `kerrconv`), which use the Laor (1991) limb-darkening law. However, note that Monte Carlo simulations by Svoboda et al. (2009) already suggested a slight limb-brightening of the reflected radiation.

4.2.2. Relativistic Effects: The Emission Angle

So far, we only considered the effects of the reflection under different viewing angles. However, only in the non-relativistic regime these viewing angles, which are measured in the rest frame of the accretion disk, are identical to the inclination angle. As soon as light-bending effects get important, different emission angles θ_e are expected throughout the disk. Using the momentum of the emitted photon (see Eq. 2.13), it can be readily calculated via

$$\cos\theta_e = \frac{\vec{p}_{e\perp}}{|\vec{p}_e|} \tag{4.1}$$

(see, e.g., Bardeen et al., 1972; Dauser, 2010). Figure 4.3 shows how the emission angle varies over the accretion disk, depending on the inclination angle. At larger distances to the black hole ($\approx 10\, r_g$) the emission angle almost constantly equals the inclination angle. However, at the innermost regions the light-bending is getting strong enough to produce any possible emission angle. Note that we know from the jet base model (Chapter 2) and observations (Chapter 3) that the emission strongly peaks at the very innermost parts. Hence, in general a constant emission angle for the reflection spectrum is not at all suitable for modeling relativistic reflection.

4.2.3. Combining Relativity and Angular Directionality

While previously an angle averaged reflection (like `xillver`) was convolved with a relativistic reflection kernel `relconv` with usually isotropic emission pattern, the new `relxill` model is designed to overcome this simplification. As could be seen in Fig. 4.2, the reflection spectrum is highly dependent on the viewing angle. However, this viewing angle, which is the emission angle for the relativistic smearing kernel, does vary by a large amount at the innermost regions of the accretion disk due to relativistic effects (Fig. 4.3). The `relxill` model now takes the actual reflection spectrum for each point at the disk into account and convolves it according to its position on the disk, weighted by the chosen irradiation. Note that this means that such an approach can not

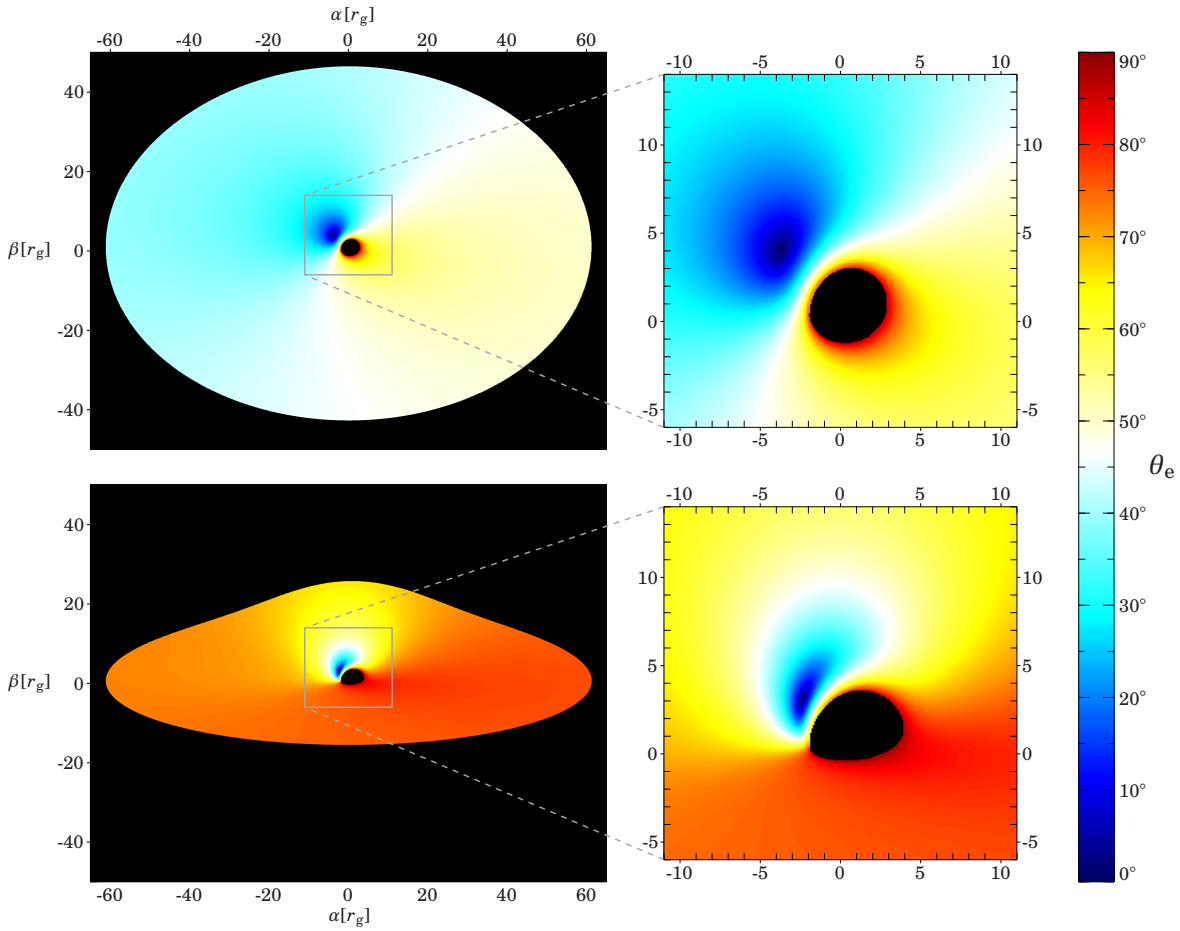

Fig. 4.3.: *An accretion disk as seen by a distant observer under and inclination of* 45° *(upper panel) and* 75° *(lower panel). The color code shows the emission angle* θ_e *in the rest frame of the accretion disk.* α *and* β *are again sky coordinates, as already used in Fig. 2.4.*

be mimicked by any model, which simply convolves a reflection spectrum. Therefore the direct combination of reflection and relativity is essential to the results presented in the following.

Figure 4.4[4] compares the `relxill` model with the new angle-dependent `xillver` model, convolved with `relconv`. The inclination angle was linked in both models, to visualize that only the improvement to an angle-dependent reflection is not sufficient. Especially for larger ionization and large angles major differences are evident. Moreover, the models not only differ at the strong Fe Kα line, but also the continuum and the Compton hump exhibit changes (mainly for $\theta = 80°$). Note that already small differences can have a large impact on the determination of parameters like the spin of the black hole. Section 4.2.4 will explicitly analyze the bias that arises.

Figure 4.5 compares `relxill` with the common approach, i.e., convolving an angle-averaged reflection model (in this case `xillver`) with a relativistic smearing kernel (e.g., `relconv`). For increasing inclination angle the spectrum shifts to higher energies. Despite this generally known shift, more subtle differences can been seen in the ratio plot. While being very similar around the Compton hump (20–40 keV), the difference in the more energetic parts of the spectrum increase with decreasing inclination angles (up to 10 %). Even more importantly, at softer energies large

[4] Note that in García et al. (2014) in this figure the color and the gray lines were accidentally switched.

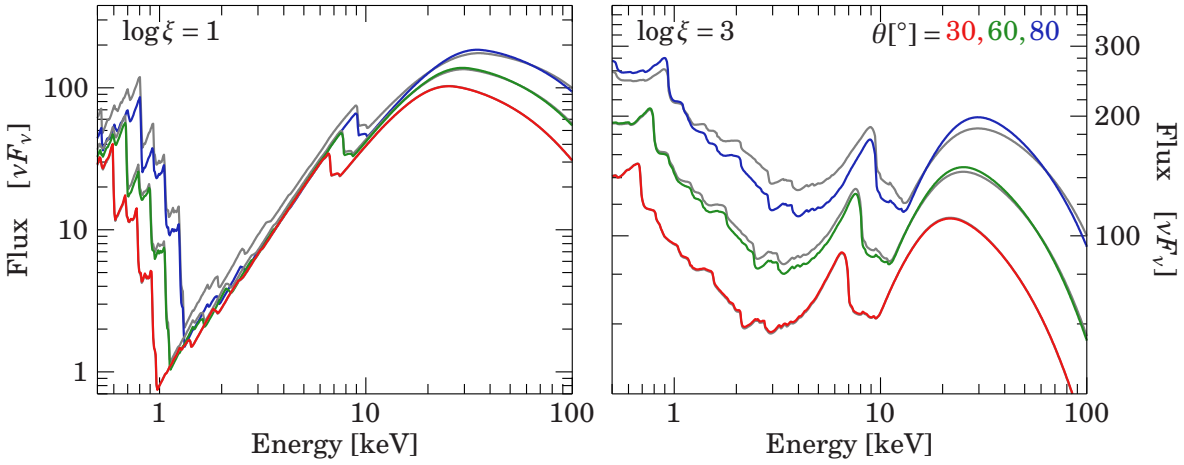

Fig. 4.4.: *Spectra calculated with the new* `relxill` *model for different inclination angle, properly taking into account the angular effects. In order to visualize the difference to the common approach, the angle-dependent* `xillver` *model convolved with* `relconv` *(with angles linked) is shown in gray. The other parameters are the same, i.e., photon index* $\Gamma = 2$*, emissivity* $\epsilon = 3$*, and spin* $a = 0.99$*. Figure adapted from García et al. (2014).*

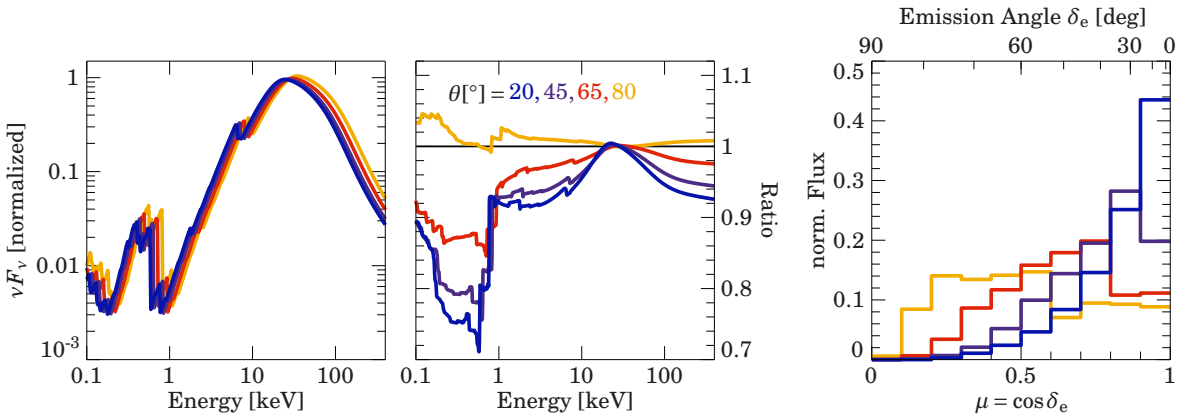

Fig. 4.5.: *Left: The* `relxill` *model for different inclination angles. Middle: Ratio between* `relxill` *and the previous, angle-averaged approach. Right: Distribution of angles depending on the inclination angle. Note that the angle-averaged version of the model would assume a constant distribution. Colors are for different inclination angles, as indicated in the middle panel.*

amounts of flux are "missing" for a low inclination, compared to the angle averaged model. Generally, note that the differences seen for the lines and the continuum in the non-relativistic case are recovered here. Clearly, the absolute deviation is now lower due to the strong relativistic smearing. The reason for these differences can be seen in the the right panel of Fig. 4.5. It shows how the flux is distributed depending on the emission angle. While the angle-averaged models implicitly assume a constant distribution, different distributions depending on the relativistic parameters and the inclination angle are actually expected. In this example, for a standard emissivity law ($I \propto r^{-3}$) and high spin ($a = 0.99$), a flat distribution is recovered for large inclinations ($\theta = 80°$). This behavior nicely explains why this inclination show only little deviations to the angle-averaged treatment. However, for lower inclination angles the flux distribution of the emission angle gets increasingly peaked around the actual inclination angle. Therefore also the relativistic reflection spectrum dif-

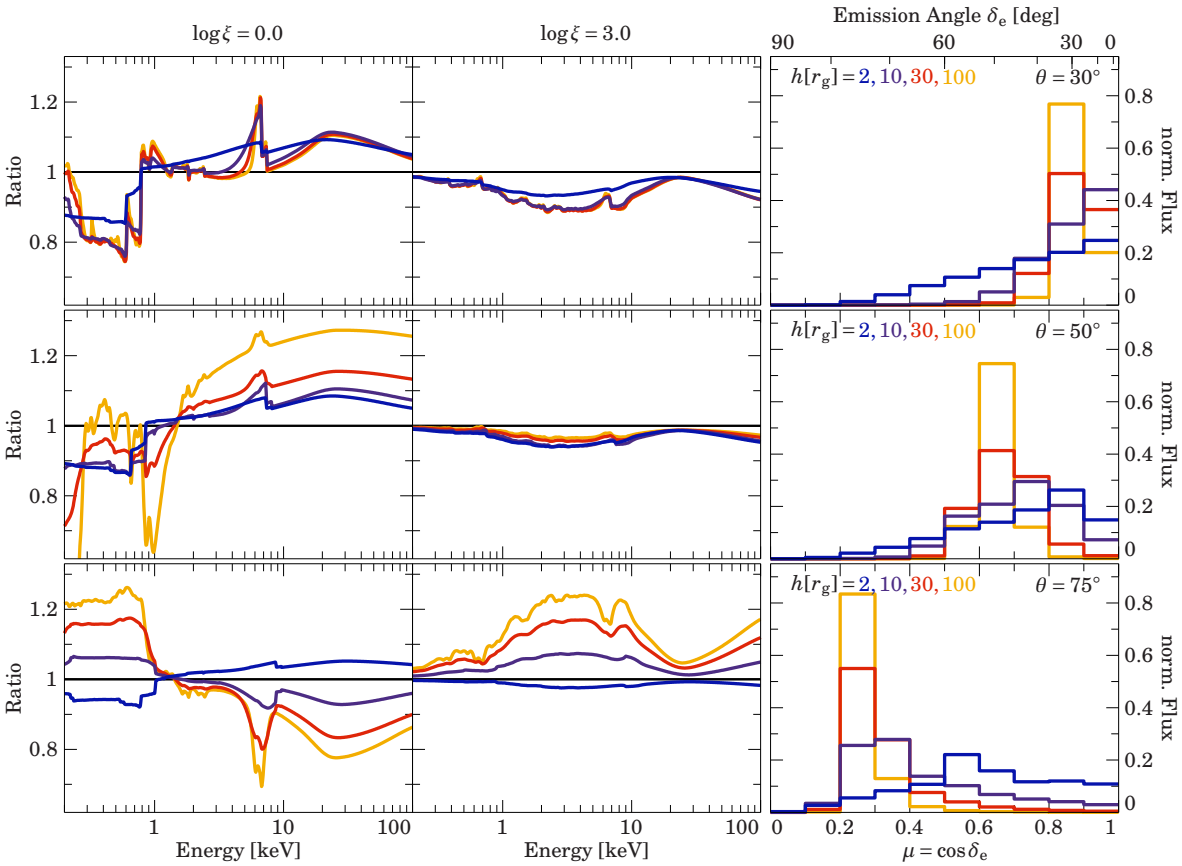

Fig. 4.6.: *Left and Middle: Ratio of spectra of the new* `relxilllp` *model (similar to middle column of Fig. 4.5), compared to the angle-averaged treatment, i.e., simply convolving* `xillver` *with* `relconv_lp` *for an almost neutral* ($\log\xi = 0$, *left) and a highly ionized* ($\log\xi = 3$, *middle) disk. The rows are for different inclination angles of the system* (30°, 50°, 75°; *as indicated in the right column). Right: Distribution of the flux depending on the emission angle; equal to right column of Fig. 4.5. As indicated in the figure, different colors depict different heights of the primary source.*

fers with an increasing amount from the averaging approach. Note that while for lower spin the impact of the relativistic smearing is less, the actual difference between the proper and averaging angle treatment does not vanish. As has been shown previously, the non-relativistic reflection only coincides with the angle-averaged reflection around 65°, while differing for lower and highers inclinations.

In general, however, these results depend on the whole variety of relativistic parameters (emissivity profile, spin, ionization of the disk, and photon index). Using the more physically motivated lamp post geometry again, the differences are analyzed in more detail in the following. In Fig. 4.6, a composition of ratio plots between the proper and the averaged angle treatment for the most relevant combinations of parameters is displayed. Spectra are now calculated for different heights of the primary source, implying a change in steepness of the emissivity profile. Simulations are only done for $a = 0.99$, as it was shown that high spin is necessary for a successful and reliable spin determination (see Chapter 2 and Dauser et al., 2013). Generally, deviations from the averaged model are at most 30%, being largest for a large source height, i.e, a flat irradiation of the accretion disk. For the strongly focused irradiation, i.e., the lowest heights of the primary source ($h < 10\,r_g$) the difference to the angle-averaged model is usually below 10 %. Note that we could

show in Fabian et al. (2014) that in order to obtain a reliable spin estimate the source has to be closer than this value to the black hole. Hence, the difference between the new relxill model and the common, angle-averaged approach will be below these 10 % for the cases actually applicable to real data. The reason for the smaller difference for a lower source height, i.e., in the more relativistic case, is easily understood. Due to the flatter emissivity profile, the outer regions of the disk are more important for the resulting spectrum. However, these outer regions do not exhibit a large effect due to light-bending (see Fig. 4.3) and therefore most flux is emitted directly under the viewing angle (see right column of Fig. 4.6). As the angle-averaged model uses a constant distribution, a stronger peaked function yields larger deviations. For decreasing height of the source this function gets less peaked. Interestingly, for the lowest heights ($h < 10\,r_g$), this peak does not completely diminish, but actually shifts to smaller angles. In summary, a low source height approximates a flat distribution best and therefore the deviations are less. Moreover differences in the reflection for a highly ionized disk (middle column, Fig. 4.6) are generally much less than for a neutral disk. The only exception to this are very large inclination angles. There the deviations are in the same order, but the energy at which they take place are totally different. While for a neutral disk a large deviation is in the lines (below 1 keV and at the Fe Kα line), these features are not existent for a highly ionized disk. Instead, the continuum in between differs by approximately the same amount. In summary, the angle-averaged treatment affects a neutral disk and especially the line features most. Moreover, a strongly focused irradiation leads to smaller deviations in the relativistic reflection spectrum.

4.2.4. Estimating the Bias for Angle-Averaged Reflection Results

As evident from the previous section, significant differences exist when using an angle-averaged approach instead of properly linking the emissivity angles to the corresponding reflection spectra. As already mentioned in the previous section, all models prior to relxill used an angle averaged approach. In the following I try to estimate the direct impact on the relativistic parameter values when using relxill instead of the commonly used convolution approach. Moreover this simulation aims to detect the amount of systematic bias, which was introduced by this simplification of using an angle-averaged relativistic reflection. In order to estimate this bias for a typical observation, an observation of a typical AGN exhibiting relativistic reflection is simulated. Therefore I assume a 100 ksec observation with *XMM-Newton* with flux and parameters similar to MCG−6-30-15 (e.g., Brenneman & Reynolds, 2006), i.e., a flux $F = 3.7 \cdot 10^{-11}\,\mathrm{erg\,s^{-1}\,cm^{-2}}$. The data is simulated with the new relxill model. The obtained spectrum is then analyzed with the common approach using an angle-averaged reflection relconv × xillver. In case of our modeling setup this simply means setting angleon=0. Moreover, standard parameters are used for the photon index ($\Gamma = 2$) and iron abundance ($A_{Fe} = 1$). The initial values are used as starting parameters for the model fit. Hence, a deviation from the initial parameter values necessarily implies an improvement of the fit.

As an irradiation of the accretion disk similar to the lamp post geometry is expected (see Chapter 2), the relxilllp model for different heights is used in this simulation. Figure 4.7 shows the resulting bias for various combinations of parameter values. In general, the results can be classified in two groups, according to the irradiation of the disk: Strong irradiation of the innermost regions (low source height) and a more constant illumination of the disk (larger source height).

A primary source at $h = 3\,r_g$ is used to study the case of a strongly focused irradiation (Fig. 4.7, left panel). Most strikingly, the iron abundance is affected most for all combinations of spin and ionization of the disk. The actual value strongly depends on the inclination angle in a way that the lower the inclination angle the larger the actual iron abundance is over-estimated. Especially

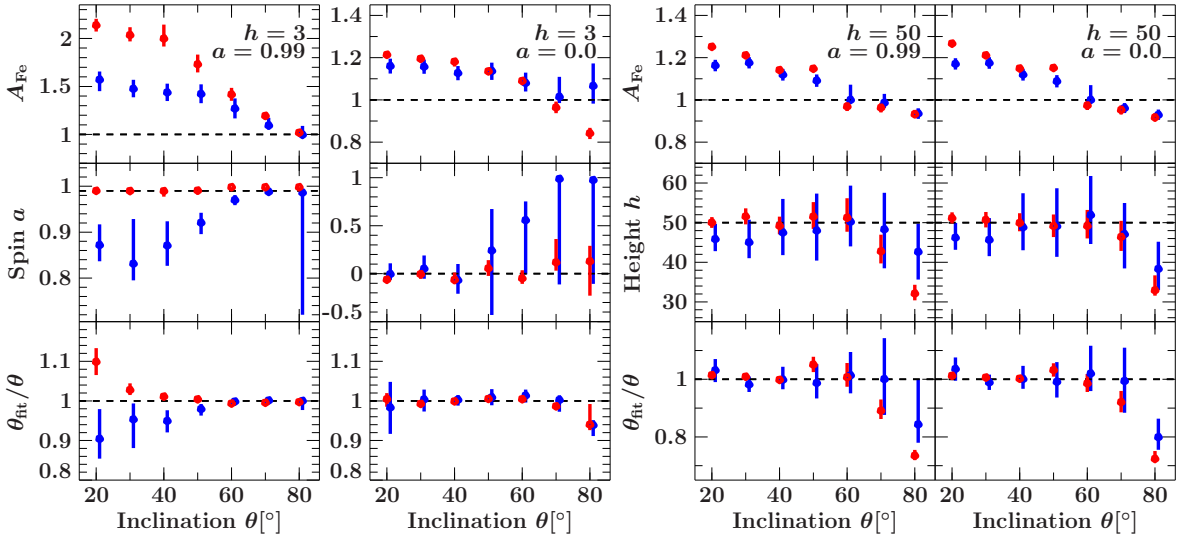

Fig. 4.7.: *Results from simulating a 100 ksec XMM-Newton observation of a relativistic reflection spectrum assuming the angle-dependent model* `relxilllp`*. The data are fitted using the angle averaged model* `relconv_lp` × `xillver`*. Simulations are performed for low ionization* ($\log\xi = 0$, *red) and high ionization* ($\log\xi = 3$, *blue) of the accretion disk, and for different inclinations. The angle-averaged model is then fitted to the simulated data. Note that all fit parameters are allowed to vary freely (i.e.,* ξ, a, θ, A_{Fe}, *and* h*). The plots shows how much the iron abundance, the spin, and the inclination angle deviates from the initial values. Left: Low source height* ($h = 3\,r_g$)*, i.e., a strong focusing of the radiation at the innermost parts of the disc. Right: Large source height* ($h = 50\,r_g$)*. As shown in Chapter 2, the spin cannot be well constrained for such a large height and therefore the height* h *of the primary source is plotted rather than the spin. The dashed line indicates the initial value of the simulation. Figure taken from García et al. (2014).*

for high spin ($a = 0.99$) and an almost neutral disk ($\log\xi = 1$), the bias can be more than a factor of two. Increasing the ionization and lowering the spin reduces the bias. Note that for a non-spinning black hole ($a = 0$), no large differences due to the ionization are evident. Moreover, the bias in this case is significantly lower, being at most 20%. Interestingly, for large inclinations this turns into the opposite trend in the case of a neutral disk. Despite the large bias in some cases, the actual value of the iron abundance is mainly not of larger interest to further interpretation. A bias on the spin on the other hand, would have crucial implications for the previously analyzed data. However, looking at the simulated deviations for the cases generally found in AGN (high spin, low ionization), only very slight deviations are evident. For a higher ionization parameter ($\log\xi = 3$) the bias increases for decreasing inclination angle. While for large spin ($a = 0.99$) and low inclination angles ($\theta < 50°$) a slight underestimation is expected, a non-spinning black hole may even be detected as rapidly rotating when seen under a large inclination angle ($\theta > 60°$). Note that in these cases the uncertainties increase, and actually no significant bias can be seen in this simulation for $a = 0$. The inclination angle itself is mainly unaffected. Only slight deviations (<10%) for the lowest angle at high spin are observed.

In order to study a more uniformly distributed irradiation with the same modeling setup, an irradiating source at $h = 50\,r_g$ is simulated (Fig. 4.7, right panel). Note that for this particular setup, it was explicitly shown (Chapter 2 and Dauser et al., 2013) that the spin can not be well constrained from observations. Therefore the bias on the inferred height of the primary source is analyzed instead, which means analyzing the steepness of the emissivity profile. In general, the bias for a

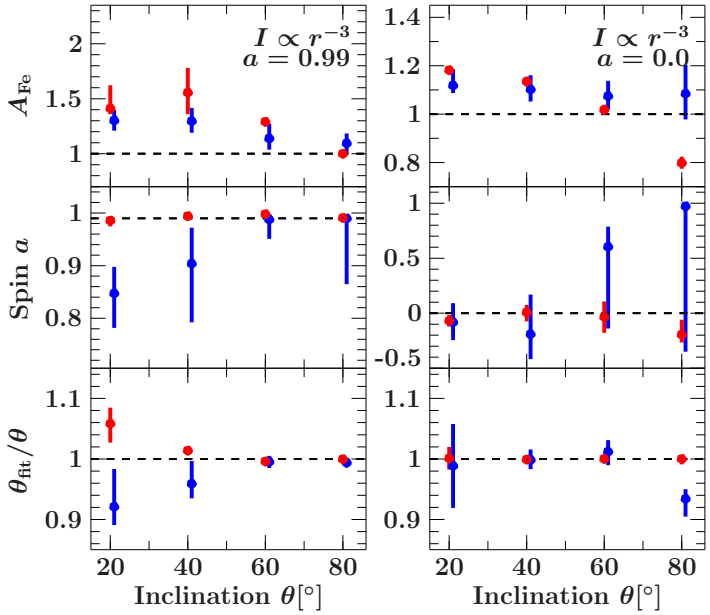

Fig. 4.8: *Simulation equal to Fig. 4.7, with the only difference being the irradiation of the disk: Instead of an irradiation by a lamp post source, an irradiation by a standard corona is simulated ($I \propto r^{-3}$). Again, the dashed line indicates the initial value used to simulate the data.*

more uniformly distributed irradiation is much lower (at most 30 %) compared to the case where most emission comes from the innermost regions of the disk. The strongest deviations are again seen in the iron abundance, being again largest for a low inclination, while vanishing for large inclinations. Interestingly, no significant differences depending on the ionization or the spin arise in this case. Especially for the spin, this is readily explained: The spectrum is mainly unaffected by the spin for such a flat irradiation, as was shown explicitly in Chapter 2. The fitted inclination, as well as the height, do not exhibit any bias for $\theta < 60°$. For larger inclinations, both quantities are underestimated by the angle-averaged treatment. For the height of the primary source, this trend actually means that angle-averaged models will overestimated the steepness of the irradiation profile. Note, however, while the actual deviations do not depend on the ionization of the disk for a flat irradiation, a lower ionization also leads to significantly lower uncertainties and therefore a more significant bias of the parameter values.

For completeness, the canonical case with the standard emissivity ($I \propto r^{-3}$) was also investigated to provide results that were not obtained by assuming an irradiation profile from the lamp post geometry. Except for the irradiation, all other details of the simulation are equal to Fig. 4.7. The resulting bias on the parameter values is visualized in Fig. 4.8. In general, the deviations are very similar to the ones for a low source height (Fig. 4.7, left panel). Especially for a low spin ($a = 0$), no significant differences are apparent. Looking at the irradiation profile of a source at $h = 3\,r_g$ (Fig. 2.8), this behavior does indeed make sense: Beyond the inner radius of the disk for a non-spinning black hole ($r_{in} > 6\,r_g$), the emissivity profile almost resembles the canonical $I \propto r^{-3}$. However, for larger spin a primary source at low height has a much more focused irradiation. Hence, the canonical corona produces a less relativistic profile and therefore the deviations are less than for the low height lamp post source. For example, the iron abundance is over-estimated at maximum by 50% instead of over 100% and does not depend as much on the ionization of the disk. Still, similar to the lamp post case at lower angles the iron abundance is over-estimated, and the spin might be slightly under-estimated in case of a highly ionized disk. But again, for a neutral disk and large spin, which is generally observed and also the most relevant case, no actual deviations in the spin parameter are observed. In summary, the approximation of using an angle-averaged convolution of the reflection spectrum in previous work does probably not alter

Tab. 4.1.: *Fractional bias of the parameters spin, iron abundance and height when using the angle-averaged approximation for the reflected radiation. The difference between the original value and the one recovered after the fit is shown for each parameter. All uncertainties are given at 90% confidence. Note that the values depicted in this table are estimated from simulating a typical but specific observation. These values should not be taken literally, but taken as an indication of how angle-averaging effects a spectrum with a certain parameter combination. Table taken from García et al. (2014).*

			— $\log\xi = 0.0$ —				— $\log\xi = 3.0$ —			
	a	h	$\theta = 20°$	$\theta = 40°$	$\theta = 60°$	$\theta = 80°$	$\theta = 20°$	$\theta = 40°$	$\theta = 60°$	$\theta = 80°$
$A_{\rm Fe}$	0.99	3	1.14 ± 0.07	$1.00^{+0.15}_{-0.09}$	0.42 ± 0.07	0.02 ± 0.03	$0.57^{+0.09}_{-0.12}$	$0.44^{+0.10}_{-0.09}$	0.27 ± 0.11	$-0.00^{+0.10}_{-0.02}$
a	0.99	3	0.00 ± 0.01	$-0.00^{+0.01}_{-0.02}$	$0.01^{+0.00}_{-0.01}$	$0.01^{+0.00}_{-0.01}$	$-0.12^{+0.05}_{-0.04}$	$-0.12^{+0.06}_{-0.05}$	-0.02 ± 0.02	$-0.00^{+0.01}_{-0.27}$
θ	0.99	3	$1.97^{+0.69}_{-0.67}$	$0.44^{+0.31}_{-0.36}$	$-0.39^{+0.18}_{-0.20}$	$-0.23^{+0.20}_{-0.16}$	$-1.92^{+1.51}_{-1.00}$	$-2.03^{+1.08}_{-1.16}$	$-0.09^{+0.43}_{-0.48}$	$0.00^{+0.00}_{-1.86}$
$A_{\rm Fe}$	0.00	3	0.21 ± 0.02	$0.18^{+0.02}_{-0.03}$	0.09 ± 0.02	-0.16 ± 0.03	0.16 ± 0.04	0.13 ± 0.04	0.08 ± 0.05	$0.07^{+0.11}_{-0.09}$
a	0.00	3	$-0.06^{+0.04}_{-0.03}$	$-0.06^{+0.08}_{-0.05}$	$-0.05^{+0.09}_{-0.06}$	$0.13^{+0.17}_{-0.36}$	$-0.00^{+0.12}_{-0.07}$	$-0.07^{+0.17}_{-0.15}$	$0.56^{+0.20}_{-0.57}$	$0.97^{+0.03}_{-1.09}$
θ	0.00	3	$0.09^{+0.31}_{-0.39}$	$-0.04^{+0.14}_{-0.20}$	$0.27^{+0.20}_{-0.19}$	$-4.79^{+4.16}_{-1.13}$	$-0.34^{+1.30}_{-1.34}$	$0.11^{+0.49}_{-0.59}$	$0.81^{+0.91}_{-1.06}$	$-4.91^{+1.03}_{-2.20}$
$A_{\rm Fe}$	0.99	50	0.25 ± 0.02	0.14 ± 0.02	-0.03 ± 0.03	$-0.07^{+0.03}_{-0.02}$	0.16 ± 0.03	0.12 ± 0.03	$-0.00^{+0.08}_{-0.01}$	-0.06 ± 0.03
a	0.99	50	$-1.99^{+0.37}_{-0.01}$	$-1.99^{+1.01}_{-0.00}$	$0.01^{+0.00}_{-1.76}$	$0.01^{+0.00}_{-0.03}$	$-1.99^{+2.00}_{-0.01}$	$-1.98^{+1.99}_{-0.01}$	$0.01^{+0.00}_{-2.00}$	$0.00^{+0.01}_{-2.00}$
θ	0.99	50	0.29 ± 0.20	$-0.07^{+0.44}_{-0.42}$	$0.43^{+2.95}_{-1.99}$	$-21.22^{+1.60}_{-1.23}$	$0.62^{+0.79}_{-0.82}$	$-0.06^{+1.81}_{-1.33}$	$0.80^{+4.90}_{-3.74}$	$-12.55^{+12.55}_{-5.09}$
$A_{\rm Fe}$	0.00	50	0.27 ± 0.02	0.15 ± 0.02	-0.03 ± 0.03	$-0.08^{+0.03}_{-0.02}$	0.17 ± 0.03	0.12 ± 0.03	$0.00^{+0.07}_{-0.02}$	-0.07 ± 0.03
a	0.00	50	$-1.00^{+0.49}_{-0.00}$	$-1.00^{+0.90}_{-0.00}$	$1.00^{+0.01}_{-1.55}$	$1.00^{+0.00}_{-0.04}$	$-1.00^{+2.00}_{-0.00}$	$-1.00^{+2.00}_{-0.01}$	$0.77^{+0.23}_{-1.78}$	$0.99^{+0.01}_{-1.99}$
θ	0.00	50	0.25 ± 0.20	$0.10^{+0.46}_{-0.41}$	$-0.86^{+1.95}_{-1.78}$	$-22.10^{+2.19}_{-0.86}$	$0.72^{+0.80}_{-0.82}$	$0.03^{+1.84}_{-1.35}$	$1.20^{+5.80}_{-3.65}$	$-16.09^{+5.17}_{-3.49}$

any of the obtained results. The most interesting parameters such as the spin or the inclination of the system were found to be mainly unaffected by this simplification. The simulation suggests that the iron abundance might have been over-estimated by a significant amount in some of the observed source.

The presented results might shed a new light on results for sources where a high iron abundance was determined. The most extreme example probably being 1H0707−495 (Sect. 3.3). Having a large spin and low source height, the results of this simulation suggest that at least part of the extremely high iron abundance needed to explain the data of 1H0707−495 might be due to the usage of the simplified angle-averaged model. In order to provide the possibility to look up the actual value of the bias, Tab. 4.1 shows the fractional deviation for all values plotted in Fig. 4.7. It can be directly compared to older observations in order to get a feeling for the order and direction of the bias. In the previous Chapter, this table has been applied to 1H0707−495, leading to the suggestion that the iron abundance might have been over-estimated by 50–70% in the observations presented in Sect. 3.3.

4.2.5. Application to observational data

In order to illustrate the improvements of the `relxill` model also a thorough comparison was made in García et al. (2014), by analyzing real observational data. Therefore the AGN Ark 120 was analyzed. This specific source was chosen, as it is a known "bare" Seyfert 1 galaxy, which implies that only very weak intrinsic absorption is present, which greatly simplifies the data analysis (see, e.g., Patrick et al., 2011). A 100 ksec *Suzaku* observation taken in April 2007 (Obs-ID: 702014010) was used for this purpose. In the end, the co-added spectrum of the two front-illuminated CCDs and the PIN data was used for the analysis (see García et al., 2014, for more information on the data extraction). Following Nardini et al. (2011) and Walton et al. (2013), Ark 120 is well described by relativistic reflection and an additional cold reflector. At first, the cold reflection is modeled by `xillver` (ionization fixed to $\log\xi = 0$). Clearly, the relativistic reflection is analyzed with `relxill`, using `angleon=0` in order to simulate the previous, angle-averaged approach. A good fit is ob-

Tab. 4.2.: *The best fit parameters for Ark 120 data, using the* relxill *model. For the angle-averaged model it was simply set* angleon=0*. The inner radius was fixed at the ISCO, and the outer at* $r_{\rm out} = 400\,r_{\rm g}$*. The redshift of the source set to* $z = 0.0327$ *(Theureau et al., 2005). In general, the parameter values are in good agreement between the two models. Table taken from García et al. (2014).*

Component	Parameter	angle-averaged	angle-dependent
relxill	ϵ	$4.4^{+2.0}_{-1.2}$	$4.8^{+1.8}_{-1.1}$
relxill	a	$0.67^{+0.12}_{-0.21}$	0.66 ± 0.13
relxill	θ (deg)	$45.0^{+5.3}_{-2.7}$	$45.3^{+4.8}_{-2.4}$
relxill	Γ	$2.17^{+0.02}_{-0.01}$	$2.17^{+0.02}_{-0.01}$
relxill	$\log\xi$	$1.03^{+0.16}_{-0.26}$	$0.84^{+0.24}_{-0.10}$
relxill	$A_{\rm Fe}$	$1.54^{+0.44}_{-0.45}$	$1.78^{+0.39}_{-0.40}$
relxill	$N(10^{-4})$	$1.81^{+0.32}_{-0.29}$	2.07 ± 0.2
xillver	$N(10^{-4})$	$1.55^{+0.42}_{-0.40}$	$0.14^{+0.07}_{-0.04}$

tained (see Tab. 4.2 for the explicit values), which is in agreement with the results obtained by Walton et al. (2013). In detail, the spin is constrained to $a = 0.67^{+0.12}_{-0.21}$ and the inclination to $\theta = 45.0^{+5.3}_{-2.7}$ deg.

Now the same fit is conducted, but using the angle-dependent xillver for the cold reflector and relxill with the proper angle treatment (angleon=1). Again, the model describes the data very well. The detailed parameter values can be found in Tab. 4.2. Considering the two crucial parameters, the spin ($a = 0.66 \pm 0.13$) and the inclination ($\theta = 45.3^{+4.8}_{-2.4}$ deg), their value stays constant. The impact of the new relxill model can be seen as the uncertainties on both parameters are significantly reduced. As predicted from the simulations (see Fig. 4.8), no bias in the parameters was found. In order to illustrate this behavior better, a contour map for the spin and the inclination angle was calculated. The contours for both cases are displayed in Fig. 4.9. As already mentioned above, both fits recover approximately the same best fit values (black crosses). The contours show even more clear that the new relxill model with the proper angular treatment leads to significantly smaller uncertainties. Namely, the spin as well as the inclination are determined better at 90% confidence compared to the angle-averaged model at 69%. Although this spectrum of Ark 120 is only one example, the capabilities of better constraining the relativistic parameters by the more physically motivated relxill model are evident.

In summary, it was shown that the relxill model is a direct improvement of any approach used previously for fitting relativistic reflection. With a simulation and directly applying this model to data suggests that the previous approach did not create systematic bias for the relativistic parameters, except in the iron abundance. Without any restrictions or additional caveats, the relxill model can and should be used in the future for fitting relativistic reflection in an improved way.[5]

4.3. The Reflection Fraction

Besides the improved angular treatment, the relxill model has additional features improving the modeling of relativistic reflection. Most importantly, this model is the first relativistic reflec-

[5] Clearly, any model similar to relxill could also be used. However, when writing this thesis no other model, which directly combines the reflection and relativity, was available.

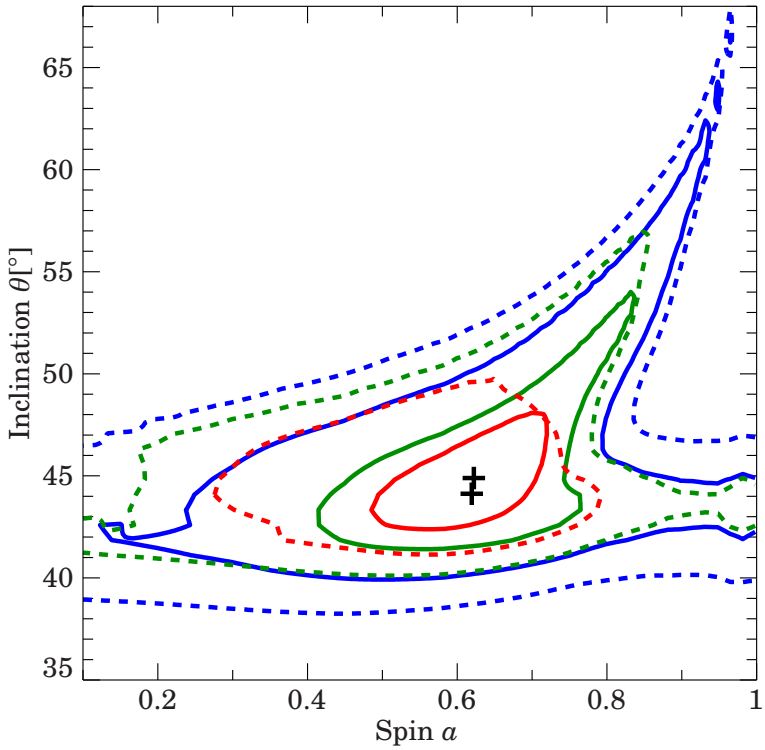

Fig. 4.9: *Contour plot for the Suzaku observation of Ark 120. Contour lines are given at 69%, 90%, and 99% percent confidence. The solid lines depict the new* `relxill` *model, taking the angular effects completely into account. Dashed lines show the common, angular-averaged approach (simulated by setting* `angleon=0` *in the* `relxill` *model). The crosses indicate the best fit parameters for both models. Figure adapted from García et al. (2014).*

tion model incorporating the *reflection fraction R* as a parameter. This reflection fraction is defined as the ratio between the reflected and the direct radiation. In order to implement this, `relxill` automatically allows to model the continuum along with the relativistically smeared reflection component. Following its definition, the relative normalization between these two components is adjusted by the reflection fraction. The effects connected to the reflection fraction, relevant for fitting relativistic reflection are thoroughly analyzed and presented in a manuscript, which was recently submitted (Dauser et al., 2014). Therefore, the following section is strongly based on Dauser et al. (2014) and follows it in large parts in verbatim.

In absence of opaque material that obstructs the central emission, an observer will always see the sum of direct radiation from the primary source of X-rays and the reflected component. In the classical limit, the flux in the reflected component is equal to the flux directly seen from the primary source. The ratio of these two components, referred to as the *Reflection Fraction*, *R*, can be significantly enhanced when the source height is reduced due to the light bending effects near the black hole (Miniutti & Fabian, 2004). In addition, the dependency of the location of the inner edge of the accretion disk from the black hole's spin, a, also modifies the area of the reflector and thus the amount of reflection. The reflection fraction therefore encodes important information about the geometry of the reflector. While the spin is routinely determined through spectral fitting of reflection models, most models neglected the dependence of R on a, leaving R as a free parameter in previous studies.[6] The `relxill` model presented in García et al. (2014) and in the previous section is the first model which allows to directly fit the reflection fraction of a relativistically smeared reflection spectrum.

If the geometry and location of the primary source are known, then *R* can be directly calculated, given the angular dependence of the emission pattern. In practice, however, except for a rough

[6] Note that although the `pexrav` model (Magdziarz & Zdziarski, 1995) includes *R* as a fitting parameter, it is only suitable to to describe distant neutral reflection.

compactness criterion (source inside $< 10\,r_g$, Fabian et al., 2014), the exact geometry of the illumination has not been unambiguously determined for any source yet. In the following, calculations of the reflection fraction R are presented, as predicted in a lamp post geometry for different configurations of the source height h and black hole spin a. A maximum value of R is then determined for a given value of spin, which can be used to exclude unphysical solutions of low spin and large reflection fractions. In the following section it is demonstrated that this constraint has a dramatic effect in improving the constraints on the spin determinations, which in turn provides insights on the nature of the geometry of the illumination source.

4.3.1. Determination of the Reflection Fraction

As previously mentioned, the reflection fraction is defined as the ratio between the reflected and direct radiation. In detail, this leads to

$$R := \frac{f_{\rm AD}}{f_{\rm INF}} = \frac{\cos\delta_{\rm in} - \cos\delta_{\rm out}}{1 + \cos\delta_{\rm out}} \quad , \tag{4.2}$$

where the fraction has been determined for the case of the lamp post geometry, assuming a stationary, isotropic primary source. Here, $f_{\rm AD}$ and $f_{\rm INF}$ denote the fraction of the photons hitting the accretion disk or escaping to infinity, respectively. $\delta_{\rm in}$ and $\delta_{\rm out}$ are the angles under which photons hit the inner and outer edge of the disk, respectively (Fukumura & Kazanas, 2007). Using simple geometry, the exact formulas are

$$\begin{aligned} f_{\rm BH} &= \frac{1}{2}(1 - \cos\delta_{\rm in}) \\ f_{\rm AD} &= \frac{1}{2}(\cos\delta_{\rm in} - \cos\delta_{\rm out}) \\ f_{\rm INF} &= \frac{1}{2}(1 + \cos\delta_{\rm out}) \end{aligned} \tag{4.3}$$

for the lamp post geometry. See Fig. 4.10 for a visualization for different combinations of spin and height of the primary source.

In the non-relativistic case $R = 1$, i.e., half of the photons reach infinity while the other half are reflected from the accretion disk (see Fig. 4.10 for large heights). This definition of R is identical to the *covering fraction* used in most reflection models such as `pexrav` (Magdziarz & Zdziarski, 1995), where it is used to describe distant neutral reflection. It is defined via the solid angle Ω covered by the reflected radiation according to

$$R = \frac{\Omega}{2\pi} \quad , \tag{4.4}$$

such that again for an infinitely extended accretion disk its value is $R = 1$ in the non-relativistic limit. However, as relativistic reflection originates from an ionized disk very close to the black hole, the values of R obtained with `pexrav` can not be compared with our results presented in the following. In the case of the lamp post model, as already noticed previously (Miniutti & Fabian, 2004), when the source height decreases, strong gravitational beaming reduces the number of photons that reach infinity while $f_{\rm AD}$ increases, thus enhancing the reflection features (see Fig. 4.10). As a consequence of these effects, the maximum possible reflection fraction depends on the spin. Figure 4.10 also shows that while the fraction of photons hitting the disk or disappear in the black hole strongly depend on the spin, the fraction of photons reaching infinity is mainly unaffected by the spin. This behavior is due to the fact that a lower spin leads to a larger inner radius of the accretion disk and therefore more photons will fall into the black hole. Note that many of these photons will

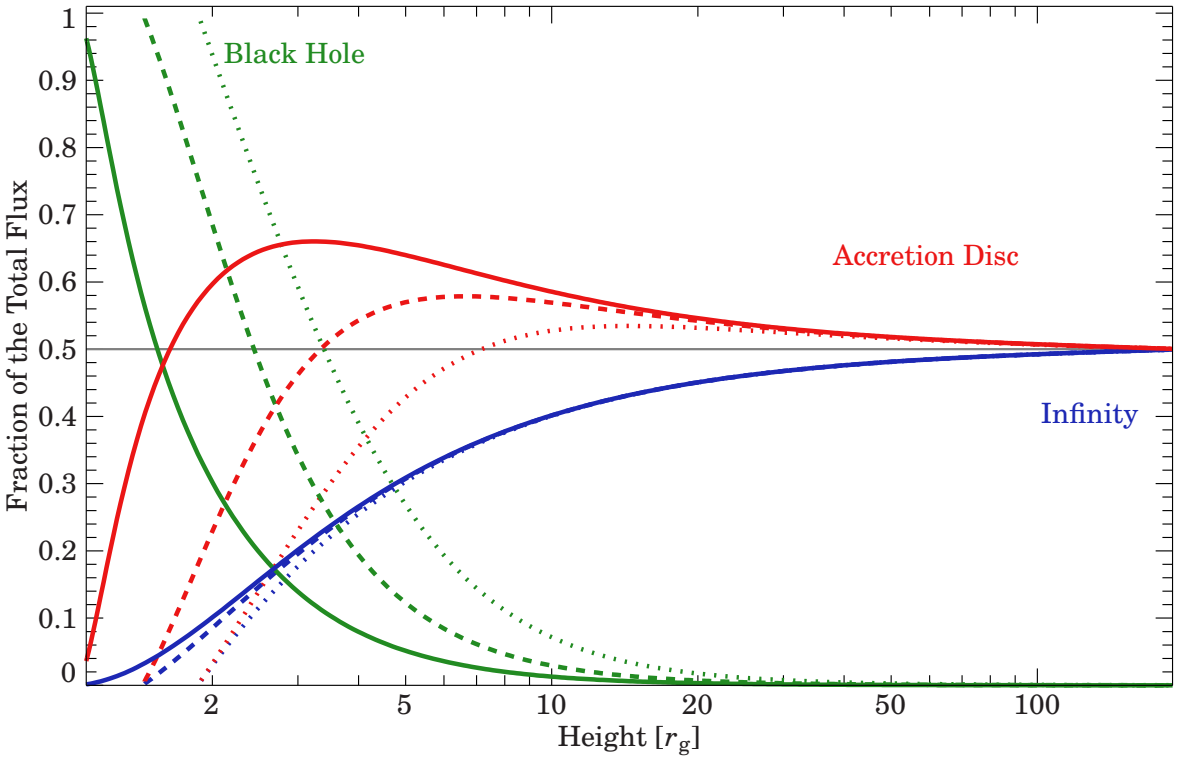

Fig. 4.10.: *Fraction of the total flux ending up in the black hole (green), hitting the accretion disc (red), or leaving the system (blue). The calculation assumes a non-moving, isotropic radiating source on the axis of symmetry of the accretion flow, fractions are shown as a function of height of the primary source and for* $a = 0.998$ *(solid),* $a = 0.9$ *(dashed), and* $a = 0.5$ *(dotted lines). Figure taken from Dauser et al. (2014).*

now cross the plane of the disk between its inner edge and the black hole. As a simplification of the model, it is assumed that all of those photons will then fall onto the black hole due to the very strong light-bending effects in its vicinity. Note that this assumption holds true for many but not all photon trajectories.

For the purpose of finding an upper limit to R, the simplified lamp post geometry, discussed in length in Chapter 2, is used. The reflection spectrum is again determined by using the `relline` code for the lamp post geometry. Due to its special position on the rotational axis of the black hole, this geometry already maximizes the reflection fraction due to the strong focusing. Figure 4.11 shows the reflection fraction for different heights of the primary source. First calculations of the reflection fraction for a lamp-post like geometry were performed by Miniutti et al. (2003) for a ring-like primary source around an extreme Kerr black hole, while Fukumura & Kazanas (2007) analyzed a point-like lamp post for different spin configurations of the black hole. The maximum reflection fraction is obtained for the case of the accretion disk extending from the innermost stable circular orbit (ISCO) out to infinity. For the cases covered by Miniutti et al. (2003) and Fukumura & Kazanas (2007), the obtained results agree very well with the earlier calculations. Additionally, for increasing source height, which generally represents a less relativistic case (see Chapter. 2), the reflection fraction converges towards its non-relativistic value of $R = 1$. As expected this behavior is independent of the spin of the black hole.

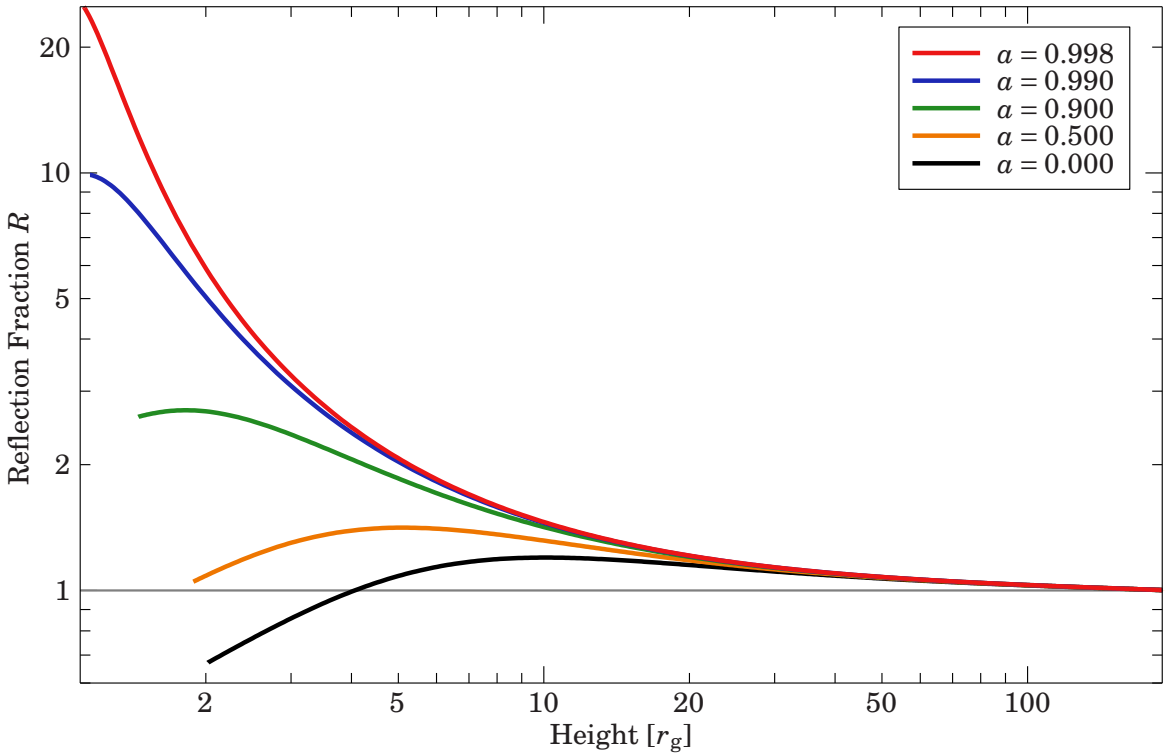

Fig. 4.11.: *Reflection fraction R as defined in Eq. 4.2 for a point-like lamp post source as a function of height. Different colors are for different values of black hole spin as indicated in the figure. Figure adapted from Dauser et al. (2014).*

4.3.2. The Maximum Reflection Fraction

Figure 4.11 shows how the reflection fraction varies with the height of the source above the black hole and with black hole spin. Except for the case of extreme spin (i.e., $a < 0.9$), if the source is close to the black hole the severe beaming of photons combined with the larger inner disk radius reduces the flux that reaches the accretion disk and the reflection fraction is small. On the other hand, if the primary source is too far away from the black hole, $R > 10r_g$, relativistic effects diminish in importance and R converges towards its non-relativistic limit. There is therefore a spin-dependent maximum reflection fraction, R_{max}. As shown in Fig. 4.12, for low values of a, this maximum is only slightly higher than its non-relativistic value, while for higher spin R_{max} increases steeply.

A different way to illustrate the behavior is shown in the right panel of Fig. 4.12, which shows that a very similar relation is obtained when fixing the spin, but allowing the inner edge of the accretion disc to vary. Again, for a growing inner radius the maximal reflection fraction quickly declines. This similarity between changing the inner radius or changing the spin of the black is not surprising: As shown, e.g., by Dauser et al. (2010), the main effect of the spin on the observed spectrum is to define the location of the ISCO. Hence, decreasing the spin or increasing the inner edge of the disk can be considered to be almost equivalent for current available data.

Figure 4.13 shows how the height of the point above the black hole from which the maximum reflection is reached changes with spin. Surprisingly, this location follows an almost linear trend which is is well fitted by the empirical relationship

$$h_{R_{max}}(a) = (1.89a^2 - 10.86a + 10.07) \cdot \left(1 + \frac{9.41 \times 10^{-4}}{\log(a)}\right) \quad . \tag{4.5}$$

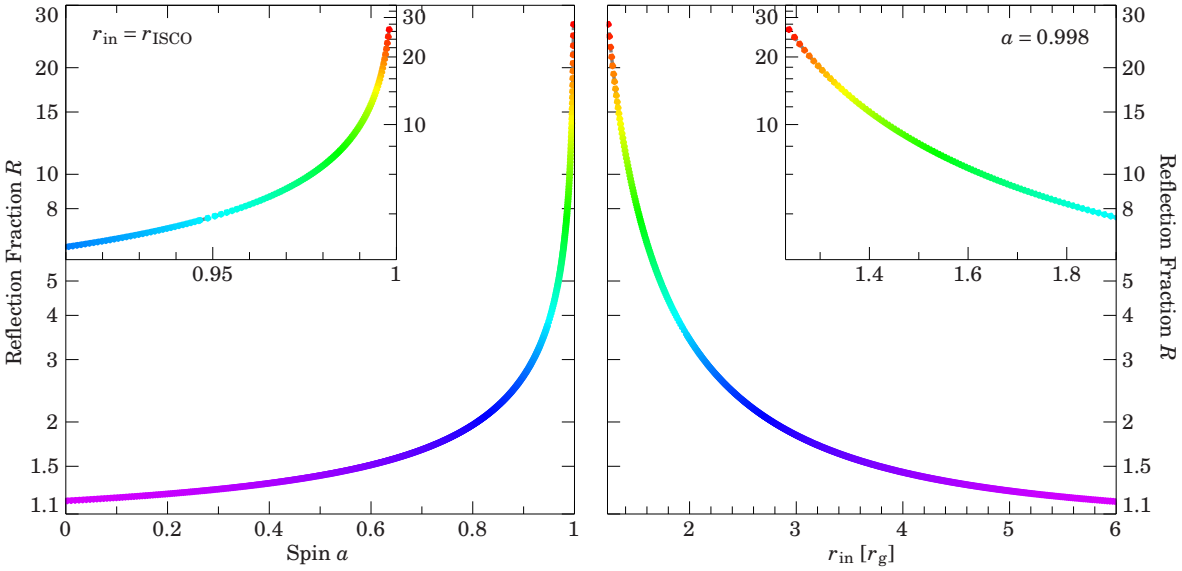

Fig. 4.12.: *Left: Maximum possible reflection fraction R_{max} as a function of spin, assuming that the accretion disc extends down to the ISCO. Right: Maximum possible reflection fraction for a maximally spinning black hole ($a = 0.998$) as a function of the location of the inner edge of the accretion disc r_{in}. The color scale of the points is identical to Fig. 4.13. Figure taken from Dauser et al. (2014).*

For $a < 0.975$, Eq. 4.5 has a precision $< 0.1\%$. Above this value of spin, the irradiating source is located directly on the event horizon of the black hole and thus $h(R_{max}) = 1 + \sqrt{1 - a^2}$.

Note that a point-like primary source as assumed above is only a first-order description of the real physical system, which is likely extended in size. However, only compact sources that are close to the black hole will lead to a strong broadening of the Fe Kα lines (Dauser et al., 2013; Fabian et al., 2014), which is essential for reliable spin estimates (e.g., 1H0707−495 or NGC 1365). Furthermore, since an extended source can be treated as the superposition of point sources (e.g., Dauser et al., 2010, 2013; Wilkins & Fabian, 2012), it is easy to see that the broadening of the reflection spectrum will be dominated by the emission from the point where the flux intercepted by the disk is at a maximum (Fig. 4.10, see also Eq. 4.5 and Fig. 4.13 below). On the other hand, if the primary source is off axis and point like X-rays will be less focused towards the disc, and therefore the maximum reflection fraction will be less than or equal to that from a source that is on axis. It is only in the special cases of irradiating sources which are extended parallel to the disk surface (e.g., the "disk like" primary source inferred by Wilkins & Fabian, 2011) or in the case of an inflowing corona which is beamed towards the disk that slightly higher reflection fractions than the ones presented in Fig. 4.12a could be reached.

Note, however, that the observer might not measure the actual reflection fraction: While the reflection fraction is defined as the total reflected flux, the observer only sees the system under a certain inclination angle. Hence, for a non-isotropic reflection the measured value might differ. These differences arise mainly for very shallow angles to the disk, where strong beaming of the radiation along the equatorial plane is expected (see, e.g., Sun & Malkan, 1989; Miniutti & Fabian, 2004). Moreover, also limb-brightening for these shallow emission angles is expected (García et al., 2014). Combining these effects in a Monte Carlo simulation, Suebsuwong et al. (2006) has shown that larger values will only be measured for very high inclination angles (i.e., $\theta > 85°$). However, these high inclinations are not relevant for modeling relativistic reflection, as the reflection fea-

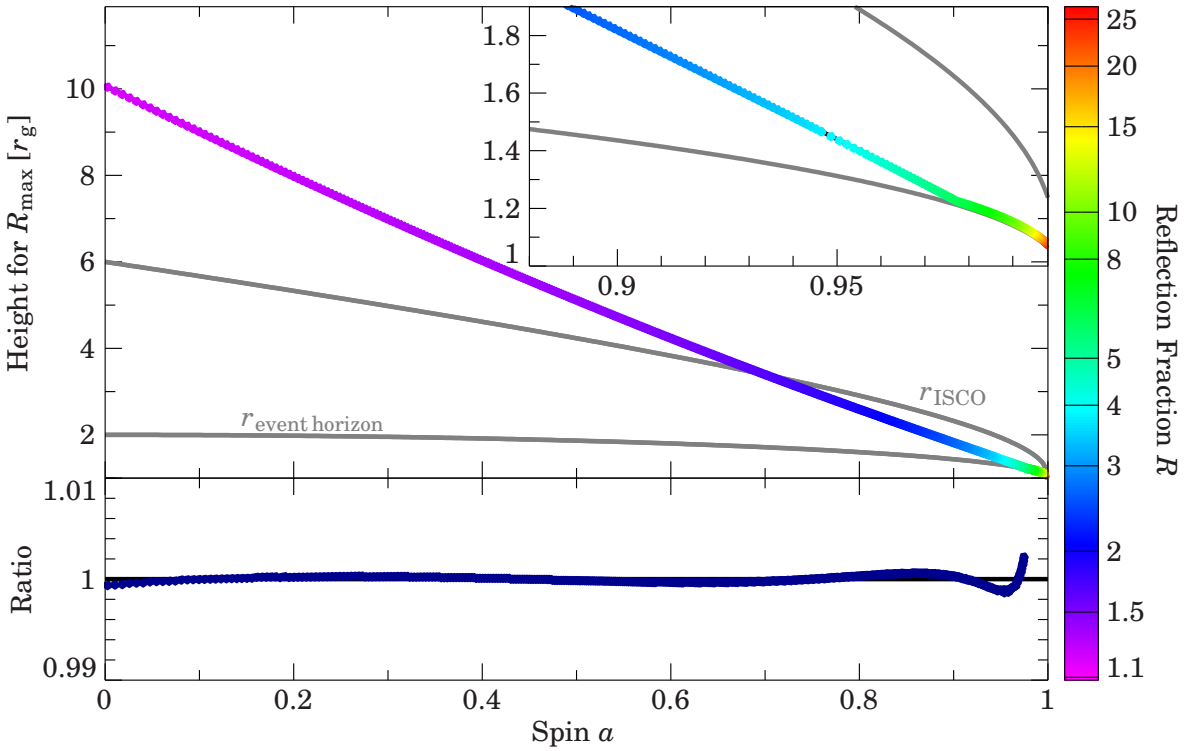

Fig. 4.13.: *The height at which the maximum reflection fraction $R_{\rm max}$ is reached as a function of a follows approximately a linear trend (Eq. 4.5). Figure taken from Dauser et al. (2014).*

tures would be completely smeared out and moreover, the SMBH would be hidden behind the torus in this case as well.

4.3.3. Constraints for Spin Measurements

The fact that there is a maximum reflection fraction can be used to constrain the parameter space when modeling observational data by excluding unphysical solutions for the spin parameter. For example, for low spins, $a < 0.5$, $R_{\rm max} < 1.5$. Hence, any solution requiring a significantly higher reflection fraction at the same time with requiring a low spin poses difficulties for interpreting the data. In many cases a different combination of parameters with a high value of the spin might be a more realistic description of the system. Note that in a recent work (Parker et al., submitted to MNRAS) this method is already successfully applied to exclude the unphysical low spin solution.

The reflection fraction also puts constraints on truncated discs: An inner radius larger than a few gravitational radii will at maximum lead to values slightly larger than $R = 1$ (Fig. 4.12b). Fits with truncated discs are therefore incompatible with larger reflection fractions.

In order to illustrate the large potential of the presented constraint on spin measurements, a typical observation of a low state AGN with *XMM-Newton* is simulated. Compared to broad-band measurements which include the reflection hump in the 20–50 keV band and provide a stronger constraint on R, measurements in the soft X-rays are especially prone to systematic errors due to foreground emission and absorption processes. These systematic errors tend to affect the continuum in the iron band, and therefore the major spectral component sensitive to a. Additional constraints such as that for $R_{\rm max}$ are therefore especially valuable for modeling soft X-ray data.

Figure 4.14 shows χ^2-contours obtained from fitting the continuum model to the simulated

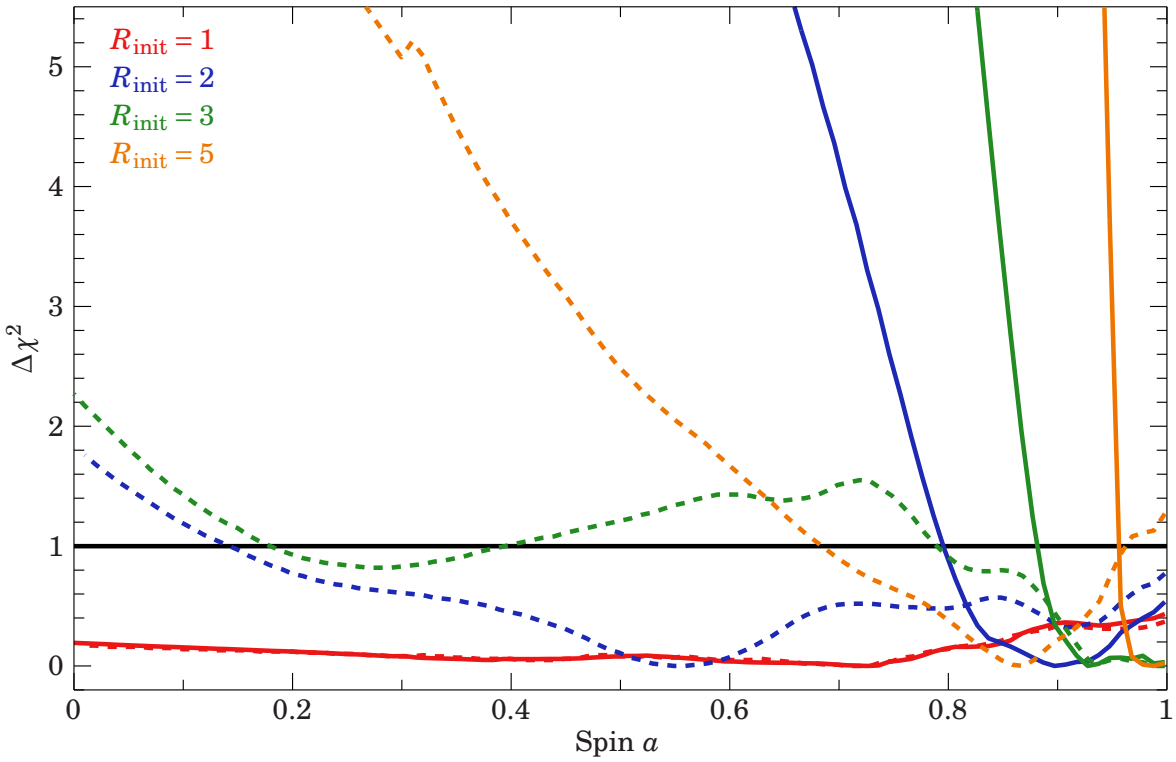

Fig. 4.14.: *A typical 100 ks observation of a low state AGN with XMM-Newton EPIC-pn is simulated, based on the low state of 1H 0707−495. The model consists of a simple absorbed power law plus reflection model,* `tbabs×relxill`*, with the 0.3–10 keV flux fixed at* $10^{-12}\,\mathrm{erg\,s^{-1}\,cm^{-2}}$*, which is a typical value for AGNs. The absorption is fixed to* $N_{\rm H} = 10^{20}\,\mathrm{cm^{-2}}$*, the emissivity index to 3,* $a = 0.97$*, the inclination to* $30°$*, the photon index to* $\Gamma = 2$*, the iron abundance to 3 times solar, and the ionization parameter* $\xi = 100\,\mathrm{erg\,cm\,s^{-1}}$*. The plot shows* χ^2 *as a function of spin a for the same model fitted to this data, but using different constraints on the reflection fraction: R allowed to be free (dashed lines) and R constrained to be less than* $R_{\rm max}(a)$ *(solid lines). The simulation is conducted for four different initial values* $R_{\rm init}$ *as indicated in the figure. Figure adapted from Dauser et al. (2014).*

spectra, with all the parameters free to vary, both with and without the $R_{\rm max}$ constraint. It is immediately evident that this constraint yields not only a better spin estimate, but also that the unconstrained fit would yield an incorrect value of the spin parameter ($a \sim 0.55$) in the case where $R = 2$. Also for a very strong reflection ($R = 5$), the best fit value without the constraint ($a \sim 0.85$) is more than one sigma away from the original value of $a = 0.99$. Generally, the constraint leads to very steep χ^2 functions in dependence of the spin: Without the new constraint, only the strongest reflection ($R = 5$) would actually be slightly constrained to $a > 0.5$ at 90 % confidence[7], i.e., $\Delta\chi^2 = 2.71$. Using the maximal reflection fraction as a constraint in the same spectrum (i.e., for $R = 5$) the spin is significantly better constrained to $a > 0.95$. And even for a weak reflection ($R = 2$), a solid constraint of ($a > 0.75$) can be given. Note that due to the weak flux in combination with the exposure, the spin is not at all constrained for $R = 1$. And as such a low value of the reflection fraction does not interfere with the maximal reflection fraction, the new approach does not give any improvement in this case. This can be seen in the plot, as both red lines are almost completely

[7] This value is common in X-ray data analysis.

identical. In summary, taking the maximum reflection fraction into account therefore avoids possible unphysical solutions, while also significantly reducing the uncertainties on the spin parameter directly.

4.3.4. Conclusions from the Reflection Fraction

In this section, a determination of the reflection fraction in the lamp post geometry was presented, following largely Dauser et al. (2014). The aim was to derive a relation for the maximum possible reflection fraction depending on the spin of the black hole. It could be shown that this relation approaches the non-relativistic value of $R = 1$ quickly and therefore strongly limits the effective parameter space of R for lower values of spin. A very similar behavior is found for constant spin and a growing inner radius of the accretion disk. Simulating observations and applying the additional constraint that R is at the maximum value possible for a given spin revealed that in this way unphysical solutions can be excluded and better constraints on a could be obtained. To allow observers to take into account these additional constraints, the reflection fraction and this constrained is also included in the new `relxill` model (see Sect. 4.1 and Appendix A). In the model, the reflection fraction can either be fixed to the theoretical prediction of the lamp post model or fitted independently.

Measurements of the reflection fractions are usually scarce and inconsistent. However, some spectral surveys of local AGN have made estimates of R by fitting the reflection signatures (e.g. Nandra et al., 2007; Brenneman & Reynolds, 2009; Patrick et al., 2012). Recently, Walton et al. (2013) presented a study of 25 "bare AGN" (with no evidence for warm absorbers or any other intervening material), providing perhaps the first consistent estimate for the strength of the ionized reflection (rather than the distant, neutral reflection) in a large sample of AGN. Although their values of R are approximate, they find a strong preference for reflection fractions near unity, which agrees well with our theoretical predictions. There is only one case, 1H 0707−495, for which the reflection fraction is extremely high ($R = 275$) despite its extreme spin ($a > 0.994$), but the source was in a particularly low state when direct power law is difficult to measure. It is particularly interesting to note that our simulation for $R = 2$ (Fig. 4.14) resembles in many cases the χ^2 confidence contours shown by Walton et al. (2013, their Fig. 2), in particular the tendency of finding two different solutions for the spin. Good examples are Mkr 841, 1H 0323+342, NGC 6728, Mrk 359, and Mrk 1018. This behavior can be interpreted as a consequence of certain degeneracy between the amount of reflection and the spin. This degeneracy can be removed by implementing the constraint on the maximum value of R presented in this letter. Note that in certain cases measuring the reflection component of the spectrum can be challenging, as overlying absorption and emission processes complicate the flux determination of the reflected radiation. Therefore the best measure is to use the flux of the featureless Compton hump (roughly between 20 and 40 keV). However, note that distant reflection might complicate this determination.[8]

[8] The `relxill` model uses the flux between 20–40 keV to calculate the reflection fraction.

CHAPTER 5

CONCLUSIONS AND OUTLOOK

5.1. A PHYSICAL APPROACH TO RELATIVISTIC REFLECTION

The main aim of this thesis was to build a more advanced and physical model for relativistic reflection and investigate it in detail. First of all, extending the reflection model for the lamp post geometry allows to model the actual geometry, instead of fitting an artificial emissivity described by a broken power law. In this case additional information is gained in terms of the height of the irradiating source. Moreover, extended, moving, and accelerating primary sources were investigated. Applying this model to actual data it was shown that the lamp post geometry is capable of describing X-ray data of GBHs and SMBHs equally well as the artificial power law (Chapter 3, Duro et al., 2011; Dauser et al., 2012; Duro et al., 2014). Regarding its suggested interpretation as the base of a jet (see Sect. 2.1), the compatibility of this geometry is of great importance: Instead of being only a theoretical description of the data, it can be directly interpreted as an approximation of the accretion geometry. This interpretation of the primary X-ray source as the base of a jet has already been suggested by different observations, such as the correlation between radio and X-ray radiation (Corbel et al., 2000; Wilms et al., 2007) or the ability of physical jet models to properly predict and fit the over-all X-ray spectra of black holes equally well then standard coronal models (e.g., Nowak et al., 2011). However, also from the side of the relativistic reflection no conclusive statement about the primary source could be made within this thesis (Chapter 3). While the shape and steepness of the emissivity profile, which is generally observed, strongly suggest a very compact geometry similar to the lamp post geometry, an artificial broken power law emissivity always described the data equally well. Nevertheless, important conclusions can be drawn from these observations, which are generally applicable to measurements of relativistic reflection. A detailed investigation led to the important conclusion that the observed broad emission lines can only be explained by a compact irradiating source (see Sect. 2.7.3, Dauser et al., 2013). Further analysis in Sect. 2.7.3 revealed that a compact primary source is necessary to obtain a reliable spin estimate. With more specific simulations, we conclude in Fabian et al. (2014) that this results implies that the source has to be closer than $10 r_{\mathrm{g}}$ to the black hole. Note that although this investigation started with the very specific and theoretical lamp post geometry, the gained conclusions regarding the source compactness are valid for any geometry.

The great success of the combination of relativistic smearing and a proper ionized reflection model lead to the development of a combined model providing a more self-consistent description of relativistic reflection. It was designed to be easily applicable by observers, without introducing any further assumptions, while still satisfying the requirements of a more physical approach. The ideal goal of this model would be to act as spectral analysis standard tool for modeling relativistic reflection in the next years, similar as has been the Laor (1991) line model in the beginning of the

era of fitting "broad iron lines". With the new `relxill` model presented in this work, a huge step forwards was made in this direction. First of all, `relxill` is applicable to a large range of different black hole and neutron star reflection spectra, due to many different parameters and flavors of the model. For example, it also includes for the first time a variable high energy cutoff and the modeling package also includes a non-relativistic model to be able to fit distant, ionized reflection as well. Even more important, combining reflection and relativistic smearing with `relxill` yields improved results: As was shown in Sect. 4.2, this direct combination allows for the first time to properly treat the angular dependency of the reflection in combination with general relativistic line broadening. Compared to previous models, which all assumed an angle averaged reflection, this approach leads to much tighter constraints on the relativistic parameters, such as the spin or the inclination. Moreover, the new model revealed that for certain parameter combinations the angle averaged approach may significantly overestimate the iron abundance. The other parameters, e.g., the spin or the inclination, were found to be mainly unaffected by the old, averaging approach. Concluding, the new `relxill` model provides an improved way to fit relativistic reflection. It does not introduce any new assumption or additional caveats and can therefore be absolutely recommended to be used in the future. Although the results obtained in this thesis strongly favor the usage of the lamp post geometry, note that `relxill` also contains a setup to fit the empirical broken power law emissivity.

5.2. Consequences for Interpreting Samples of Spin Measurements

The obtained results in this thesis have several consequences for constructing a sample of spin measurements (similar to Tab. 1.1), which can be used to draw conclusions about AGN jets or galaxy evolution, as motivated in the introduction. First of all, Brenneman et al. (2011) discuss a general observational bias towards detecting higher spin for any flux limited sample. As the authors describe, it comes from the fact that in standard accretion disk theory black holes with a higher spin exhibit a larger radiative efficiency and are therefore easier to detect. In general, there are methods to be able to correct for this selection bias, allowing us to draw conclusions about the actual spin distribution nevertheless (Brenneman et al., 2011). However, there are more caveats, which are directly related to measuring the spin of the black holes by fitting relativistic reflection features. Investigations in the lamp post geometry suggest that extended primary sources, actually irradiating the accretion disk around a black hole with maximum spin, yield such a relativistic reflection spectrum that the black hole might be very easily confused to be non- or negatively spinning (see Fig. 2.17). Hence, it is essential to constrain the location of the irradiating source by an independent method in order to reliably measure lower spinning sources. As already discussed in Sect. 2.8, reverberation mapping is capable of doing so and has already been successfully applied to a few sources. With future missions, such as the planned *Athena* satellite (see, e.g., Nandra et al., 2013), these measurements can be extended to a larger sample. However, even assuming the geometry of the irradiation source is known, slowly rotating black holes are much harder to detect. Generally, a lower spin leads mainly to a less pronounced relativistic smearing (see, e.g., Dauser et al., 2010). Hence, the effects on the intrinsically non-relativistic reflection spectrum are much less than in the high spin case making it harder to distinguish from distant reflection. Moreover, the results obtained by analyzing the reflection fraction (see Sect. 4.3 and Dauser et al., 2014) reveal that strong reflection features can only occur for a large spin of the black hole. Due to a generally weaker reflection, slowly spinning black holes are therefore even harder to detect. Still,

note if we measure the accretion geometry (e.g., with reverberation mapping), there is no apparent degeneracy of the spin value when fitting the reflection spectrum. Therefore, despite all caveats discussed in this thesis, we might be able to measure a reliable sample of black hole spins with the superior data quality in the new era of X-ray facilities such as *Athena*, which can be used draw conclusions about galaxy evolution and jet formation.

5.3. Outlook: The future of spin measurements

5.3.1. The future X-ray observatory: The *Athena* mission

The recently approved "Advanced Telescope for High Energy Astrophysics" (*Athena*) will carry two instruments on board, improving the studies of relativistic reflection features significantly. Its Wide Field Imager (WFI, using DEPFET active pixel technology) will make AGN spin surveys out to significant redshifts ($z \sim 1$) possible, due to a large effective area in the Fe Kα region (0.25 m^2 @ 6 keV). The cryogenic X-ray spectrometer, called X-ray Integral Field Unit (X-IFU, based on a large array of Transition Edge Sensors), was shown to easily allow one to separate the narrow emission and absorption features superposed on the broad, relativistic reflection features that are analyzed to obtain spin estimates (Nandra et al., 2013; Barret et al., 2013). Especially the WFI detector will improve the determination of a larger number of black hole spins significantly. In order to quantify this improvement, a study estimating how many counts are necessary to measure the spin at a certain precision was conducted. Data were simulated for increasing exposure times of the detector, assuming a standard relativistic reflection spectrum. Figure 5.1 shows the results of the simulation.

As a bright source was used for this simulation (100 mCrab), even the lowest exposures (< 100 sec) lead to reliable spin estimates of ~10% precision. For an exposure of only a little more than 10 sec, the WFI will detect around 10^6 events. However, note that this plot is also valid for fainter sources, as the exposure can be simply scaled according to the number of total counts. That means a 1 mCrab source would need around 1 ksec of exposure instead of 10 sec in order to estimate its spin to a precision of < 10%. These results suggest that with the *Athena* satellite short snapshot observations are sufficient to obtain a spin estimate with an acceptable precision. For an increasing number of counts, the value can be determined significantly better. Above approximately 10^9 events, no further improvement is apparent. Note that this simulation, as well as spin estimates usually as well, do not take any systematic effects into account. Therefore it is questionable if it makes sense to determine the value of the spin to a very high precision, as these uncertainties only specify the statistical error.

5.3.2. A self-consistent model: An ionization gradient in the accretion disk

The largest simplification of the current `relxill` model is the assumed constancy of the ionization over the complete accretion disk. As has been shown in Chapter 2, however, the irradiation is strongly focused on the inner parts of the accretion disk. Hence, already from basic principles a constant ionization of the disk seems to be a very crude approximation. Therefore the obvious next step forward in terms of physical modeling is to allow an ionization gradient in the accretion disk. The left panel of Fig. 5.2 shows the resulting spectrum for an ionization gradient of $\xi(r) \propto r^{-0.5}$, as well as the resulting spectra of the single zones of constant ionization. Starting with an ionization parameter of $\log\xi_{\rm ISCO} = 3.1$ at the inner edge of the disk, the ionization quickly decreases simi-

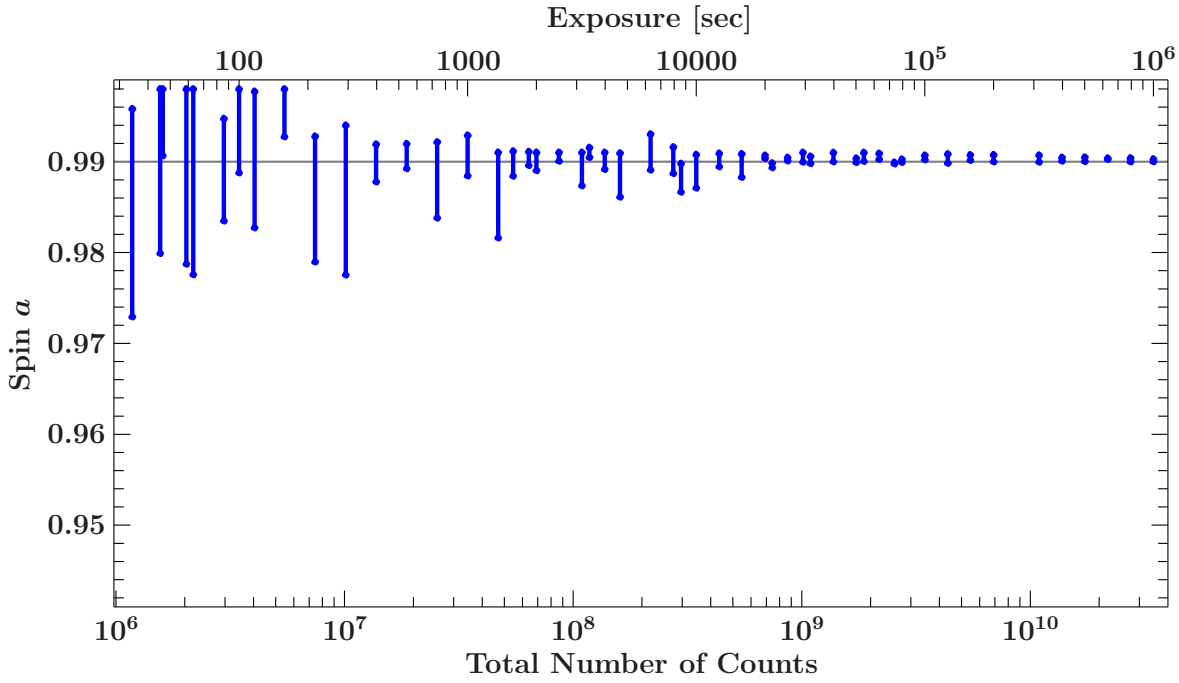

Fig. 5.1.: *Simulation of the spin determination with the WFI, which will fly on board of the planned Athena X-ray satellite. A standard relativistic reflection spectrum was assumed: spin* $a = 0.99$*, height* $3\,r_g$*,* $\log\xi = 1$*,* $A_{Fe} = 1$*,* $\Gamma = 1.9$*, and the reflection fraction fixed according to the prediction of the lamp post geometry (i.e.,* `fixReflFrac`$= 1$ *in the* `relxilllp` *model). A bright source of 100 mCrab was used. The simulation was conducted for a different number of total observed counts and then fitted with the same model while allowing all of the above parameters to vary. The plotted lines depict the 90% confidence intervals of the uncertainties in the spin value.*

larly fast as the relativistic broadening. While the innermost region is highly redshifted, blurred, and ionized (dark blue line), the over all spectrum is also influenced by the less ionized and less relativistically blurred spectra from the outer, more neutral parts of the disk. Note also that the ionization gradient seems to influence the Compton hump as well: For the innermost ionization zone (dark blue) the spectrum largely differs in the 20–50 keV region from the spectra emitted from the outer parts.

Additionally, we can finally close the last gap in self-consistency and directly calculate this ionization gradient from the irradiation as predicted from the lamp post geometry. A schematic drawing can be found in the right panel of Fig. 5.2. The disk is parametrized in discrete zones of constant ionization. In order to determine the ionization parameter from the irradiating intensity in each zone we additionally need to know the density profile of the disk. The relationship between ionization and density is simply given by the definition of the ionization parameter, being the irradiating flux divided by the density (see Eq. 1.1). As a first estimate, the density profile of a thin α-disk can be taken (Shakura & Sunyaev, 1973). Using these assumptions, specifying the height of the primary source and the accretion rate $\dot{m}$ completely fixes the ionization gradient of the disk. Figure 5.3 exemplary displays these ionization gradients for different values of the accretion rate. Note that the accretion rate simply determines the ionization at the inner edge of the disk, as it does not affect the shape of the density profile in the α-disk model. Generally, the density of the disk is expected to increase outwards, which would then lead to a decreasing ionization gradient even in the case of a constant irradiation of the disk. Hence, knowing from Chapter 2 that the emissivity profile is

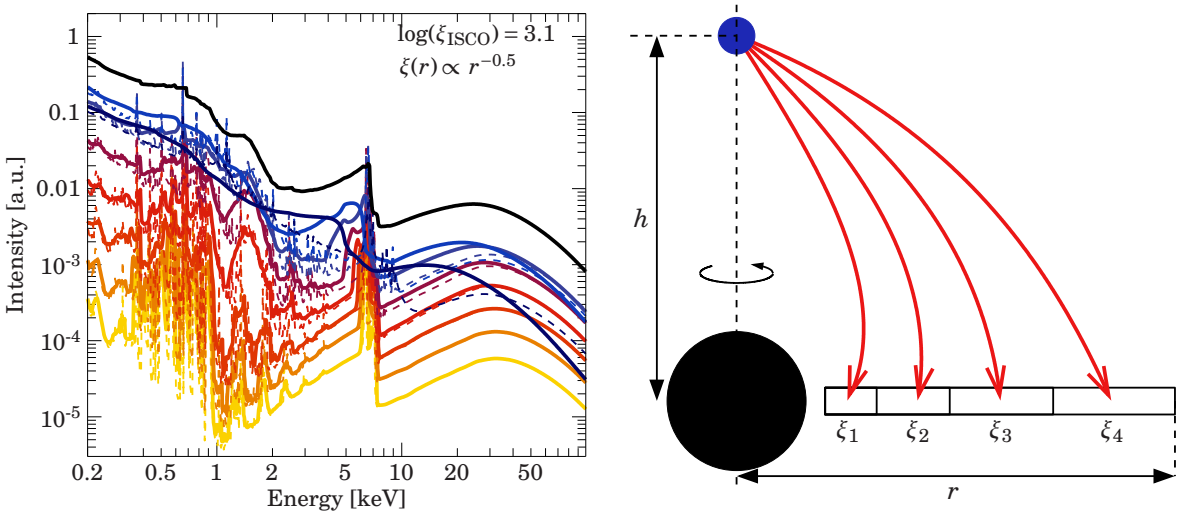

Fig. 5.2.: *Left: Spectra for the different regions of the accretion disk, assuming a radial ionization gradient of* $\xi(r) \propto r^{-0.5}$*, with an ionization of* $\log\xi_{\mathrm{ISCO}} = 3.1$ *at the inner edge of the disk. From blue over red to yellow, the distance of these regions to the central black hole increases. Dashed lines indicate the non-relativistic reflection spectra. The summed spectrum is plotted in black. Right: Scheme of the lamp post geometry, where the ionization of the disk is determined from the irradiating intensity. Similar to the situation in the left panel, the accretion disk is parametrized in single zones of constant ionization* ($\xi_{1,2,3,4}$).

expected to be very steep already suggests a very steep ionization gradient for irradiating sources at low height. Additionally, we can also drop the assumption about the density profile and fit the ionization gradient directly. As either the ionization or the density needs to be given, this means that instead of the ionization gradient one can also directly fit the density profile of the accretion disk. A sketch of relativistic fitting models implementing these features, including this function to fit for the density profile of the disk, is given in Appendix A. The density profile is approximated in this model to be a power law. Except for minor deviations at the innermost regions, the α-disk density (see Fig. 5.3) also follows a power law shape.

Figure 5.4 shows spectra and ionization gradients for different heights of the primary source. For these calculations the density profile of an α-disk was assumed (Shakura & Sunyaev, 1973). With increasing source height the ionization gradient gets flatter, as expected from the direct dependence of the ionization on the irradiating flux. A steep gradient for a very low source height is evident (upper panel). It leads to a completely ionized disk at the inner edge, while the disk is almost neutral again for radii larger than 10 r_{g}. On the other hand, a large source height ($h \geq 25\,r_{\mathrm{g}}$) only yields a mildly ionized inner edge, however, the ionization of the disk then stretches out to several tens of gravitational radii. These large differences in the ionization gradient are also reflected in the output spectra. As described in Chapter 2, the larger height of the primary source leads to narrower reflection features. This can be seen by the fact that the inner regions become less important (i.e., are lower in flux) for increasing source height. However, in all cases the neutral outer parts of the disk produce a distinct and strong iron line feature. Generally, a spectrum from a more ionized zone generally suffers from less absorption in the lower energetic part (see, Fig. 1.4 and García et al., 2013), which raises the importance of the highly ionized parts of the disk below energies of around 1 keV. This behavior can be directly seen in Fig. 5.4: While for large source heights ($h \geq 25\,r_{\mathrm{g}}$) the inner and highly ionized regions are unimportant for the iron Kα line

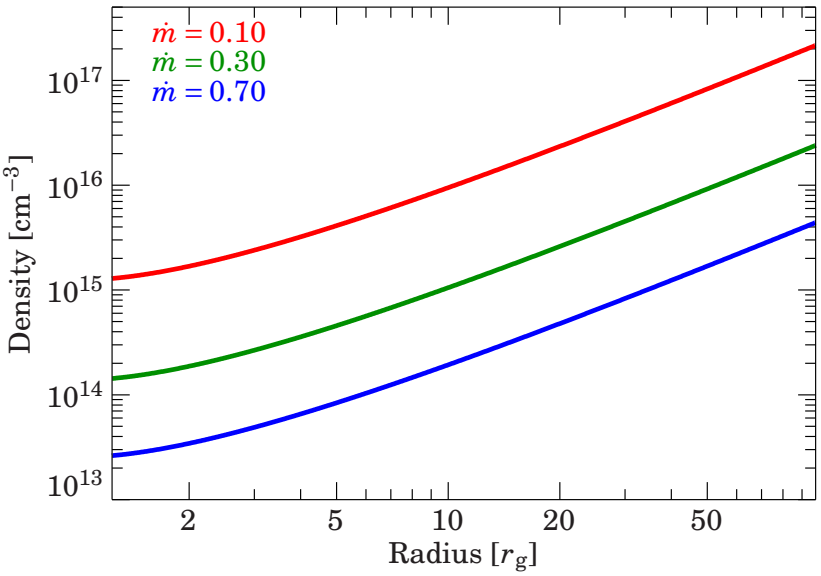

Fig. 5.3: *Density profiles for an α-disk for different mass accretion rates $\dot{m}$, as described by (Shakura & Sunyaev, 1973).*

(6.4 keV), their importance for the lower energies is significant. Interestingly, such a behavior looks roughly similar to the best fit model obtained for 1H0707−495 (Sect. 3.3), where the highly ionized component dominates the low energy part of the spectrum and the neutral reflection component is prominent around the iron Kα line. This AGN would therefore be a perfect candidate to apply the model with the ionization gradient and to try to fit the density profile of the accretion disk.

From the irradiation of the accretion disk a strong ionization gradient is expected. Despite of strong ionization of the inner parts of the accretion disk, the outer parts will remain almost neutral and still significantly influence the resulting spectrum. From those results one would expect a significant difference to single zone ionization models. However, so far such models were able to describe even the best and most recent data very well (see, e.g., Risaliti et al., 2013). Therefore the next step is to test whether the more physically motivated model including the ionization gradient is also capable of describing the data and if results for the spin or the inclination can be recovered. Moreover, we can also drop the assumption of the standard α-disk, meaning the model would not predict the ionization gradient any more, but determine it by fitting. Due to the direct connection of the ionization and the density, we are therefore able to determine the density profile directly from relativistic reflection measurements. This approach would be a unique method to test how well the accretion disk in the hard state, where generally relativistic reflection is detected, can be described by the simplified α-disk model. And finally, if the ionization gradient predicted from the lamp post geometry does not at all allow to describe the data of most sources, this result would have significant consequences for the lamp post accretion geometry and its interpretation as a jet base. Providing a computationally fast and reliable model including the ionization gradient and fitting it to the most prominent sources showing relativistic reflection is therefore the next step in order to understand the accretion black holes.

In summary, this thesis has shown a fruitful approach to improve the modeling and the interpretation of relativistic reflection features. By introducing the lamp post geometry in a fitting model, it is possible describe the irradiation by an actual primary source instead of an empirical emissivity profile consisting of a broken power law. Besides being able to describe the data equally well as the empirical model (see Cygnus X-1, Sect. 3.2 and 1H0707−495, Sect. 3.3), it was shown that the theoretical model of the lamp post geometry can be interpreted as “base of a jet”. Moreover, the case of Cygnus X-1 revealed that the physical modeling of the emissivity profile excludes unphys-

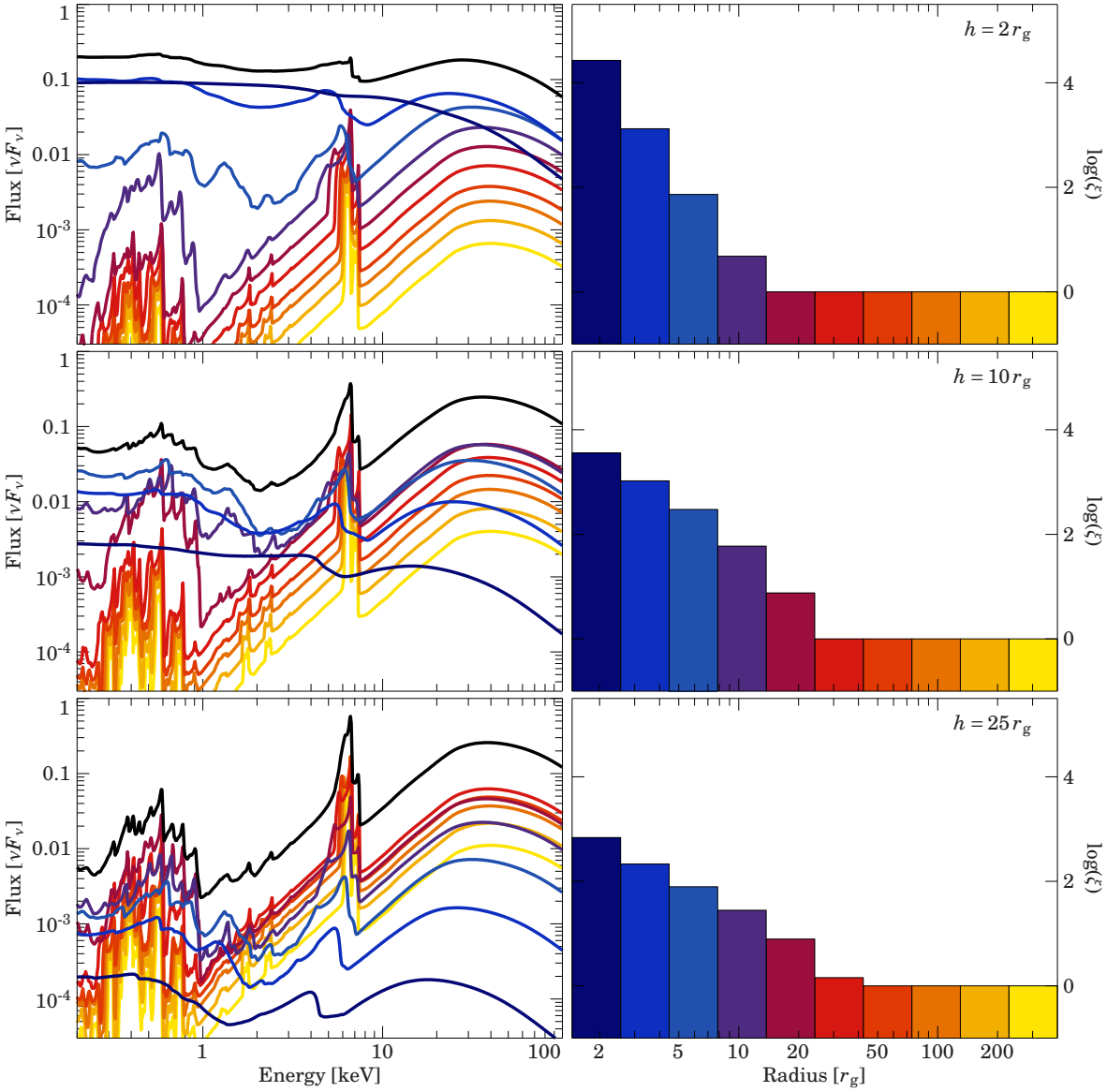

Fig. 5.4.: *Left: Reflection spectra for the different ionization zones, with colors as indicated in the right panel. The value of ionization parameter is directly calculated from the irradiation in the lamp post geometry. The black line depicts the complete reflected spectrum from all zones. Right: The radial dependence of the ionization parameter. The width of the bars corresponds to the width of the single zones. In all plots the power law index was chosen to be* $\Gamma = 2$*, and the iron abundance* $A_{\rm Fe} = 5$*. For the density profile the Shakura & Sunyaev (1973) description of the* α*-disk was used, additionally assuming a mass accretion rate of* $\dot{m} = 0.7\dot{m}_{\rm Edd}$*.*

ical solutions, such as solutions exhibiting at the same time a low spin and a very steep emissivity profile, whose origin would be very hard to explain theoretically. The observations of Cygnus X-1 and 1H0707−495 also showed that analyzing broad band X-ray spectra with a complete relativistic reflection spectrum, and not only a single line, yields solid and reliable spin estimates. However, there is still large room for improvement: In a major step, the `xillver` reflection and the relativistic `relline` code were combined in the `relxill` model. The properly treated angular dependency

and the introduced reflection fraction lead to significantly reduced uncertainties when estimating parameters such as the spin or the inclination from measured data. With thorough comparisons, simulations, and applications of the new `relxill` mode, these major improvements were evidently shown. Due to the positive results and no real[1] disadvantages compared to previous models, this model is suitable to become the standard tool for analyzing relativistic reflection of modern and future X-ray data.

[1] Only known disadvantage: The model uses more disk and memory space than previous models (~ 600 MByte compared to a few tens of MByte).

REFERENCES

Abramowicz M.A., Fragile P.C., 2013, Living Reviews in Relativity 16, 1

Arnaud K.A., 1996, In: G. H. Jacoby & J. Barnes (ed.) Astronomical Data Analysis Software and Systems V. Astron. Soc. Pacific Conf. Ser. 101, p.17

Bardeen J.M., 1970, Nat 226, 64

Bardeen J.M., Press W.H., Teukolsky S.A., 1972, ApJ 178, 347

Barr P., White N.E., Page C.G., 1985, MNRAS 216, 65P

Barret D., Nandra K., Barcons X., et al., 2013, In: Cambresy L., Martins F., Nuss E., Palacios A. (eds.) SF2A-2013: Proceedings of the Annual meeting of the French Society of Astronomy and Astrophysics., p.447

Bartelmann M., 2010, Classical and Quantum Gravity 27, 233001

Bautista M.A., Kallman T.R., 2001, ApJS 134, 139

Beloborodov A.M., 1999, ApJ 510, L123

Blandford R.D., 1990, In: Blandford R.D., Netzer H., Woltjer L., Courvoisier T.J.L., Mayor M. (eds.) Active Galactic Nuclei., p.161

Blandford R.D., Znajek R.L., 1977, MNRAS 179, 433

Bluck A.F.L., Conselice C.J., Almaini O., et al., 2011, MNRAS 410, 1174

Blustin A.J., Fabian A.C., 2009, MNRAS 399, L169

Blustin A.J., Page M.J., Fuerst S.V., et al., 2005, A&A 431, 111

Böck M., 2012, Ph.D. thesis, University of Erlangen-Nuremberg, available online at `http://www.sternwarte.uni-erlangen.de/Arbeiten/2012-10_Boeck.pdf`

Böck M., Grinberg V., Pottschmidt K., et al., 2011, A&A 533

Boller T., Fabian A.C., Sunyaev R., et al., 2002, MNRAS 329, L1

Boller T., Tanaka Y., Fabian A., et al., 2003, MNRAS 343, L89

Boyer R.H., Lindquist R.W., 1967, J. Math. Phys. 8, 265

Bradt H.V., Swank J.H., Rothschild R.E., 1990, Advances in Space Research 10, 297

Brenneman L.W., Reynolds C.S., 2006, ApJ 652, 1028

Brenneman L.W., Reynolds C.S., 2009, ApJ 702, 1367

Brenneman L.W., Reynolds C.S., Nowak M.A., et al., 2011, ApJ 736, 103

Canizares C.R., Davis J.E., Dewey D., et al., 2005, PASP 117, 1144

Cappi M., Tombesi F., Bianchi S., et al., 2009, A&A 504, 401

Carroll S.M., 2004, Spacetime and geometry. An introduction to general relativity, Addison Wesley

Carter B., 1968, Phys. Rev. 174, 1559

Chandrasekhar S., 1983, The Mathematical Theory of Black Holes, Clarendon Press and Oxford Univ. Press, Oxford

Chartas G., Brandt W.N., Gallagher S.C., Garmire G.P., 2002, ApJ 579, 169

Chiang C.Y., Reis R.C., Walton D.J., Fabian A.C., 2012, MNRAS 425, 2436

Cohen M.H., Lister M.L., Homan D.C., et al., 2007, ApJ 658, 232

Corbel S., Fender R.P., Tzioumis A.K., et al., 2000, A&A 359, 251

Cunningham J.M., Bardeen C.T., 1973, ApJ 183, 237

Dauser T., 2010, Diploma Thesis, University Erlangen-Nürnberg

Dauser T., García J., Parker M., et al., 2014, MNRAS in prep.

Dauser T., García J., Wilms J., et al., 2013, MNRAS 687

Dauser T., Svoboda J., Schartel N., et al., 2012, MNRAS 422, 1914

Dauser T., Wilms J., Reynolds C.S., Brenneman L.W., 2010, MNRAS 409, 1534

Davis S.W., Blaes O.M., Hubeny I., Turner N.J., 2005, ApJ 621, 372

de Marco B., Ponti G., Uttley P., et al., 2011, MNRAS 417, L98

den Herder J.W., Brinkman A.C., Kahn S.M., et al., 2001, A&A 365, L7

Dexter J., Quataert E., 2012, MNRAS L512

Done C., Sobolewska M.A., Gierliński M., Schurch N.J., 2007, MNRAS 374, L15

Dove J.B., Wilms J., Maisack M., Begelman M.C., 1997, ApJ 487, 759

Dovčiak M., Karas V., Yaqoob T., 2004, ApJ Suppl. 153, 205

Duro R., 2014, Ph.D. thesis, University of Erlangen-Nuremberg, available online at `http://www.sternwarte.uni-erlangen.de/Arbeiten/index.cgi`

Duro R., Dauser T., Grinberg V., et al., 2014, A&A submitted

Duro R., Dauser T., Wilms J., et al., 2011, A&A 533, L3

Einstein A., 1905, Annalen der Physik 322, 891

Einstein A., 1916, Annalen der Physik 354, 769
Elvis M., 2000, ApJ 545, 63
Emmanoulopoulos D., McHardy I.M., Papadakis I.E., 2011, MNRAS 416, L94
Esin A.A., McClintock J.E., Narayan R., 1997, ApJ 489, 865
Fabian A.C., Kunieda H., Inoue S., et al., 1994, PASJ 46, L59
Fabian A.C., Miniutti G., Gallo L., et al., 2004, MNRAS 353, 1071
Fabian A.C., Miniutti G., Iwasawa K., Ross R.R., 2005, MNRAS 361, 795
Fabian A.C., Parker M.L., Wilkins D.R., et al., 2014, MNRAS 439, 2307
Fabian A.C., Rees M.J., Stella L., White N.E., 1989, MNRAS 238, 729
Fabian A.C., Sanders J.S., Allen S.W., et al., 2003, MNRAS 344, L43
Fabian A.C., Vaughan S., 2003, MNRAS 340, L28
Fabian A.C., Vaughan S., Nandra K., et al., 2002, MNRAS 335, L1
Fabian A.C., Wilkins D.R., Miller J.M., et al., 2012a, MNRAS 424, 217
Fabian A.C., Zoghbi A., Ross R.R., et al., 2009, Nat 459, 540
Fabian A.C., Zoghbi A., Wilkins D., et al., 2012b, MNRAS 419, 116
Fender R.P., Belloni T.M., Gallo E., 2004, MNRAS 355, 1105
Fender R.P., Stirling A.M., Spencer R.E., et al., 2006, MNRAS 369, 603
Fragile P.C., 2009, ApJ 706, L246
Fukumura K., Kazanas D., 2007, ApJ 664, 14
Fürst F., 2011, Ph.D. thesis, University of Erlangen-Nuremberg, available online at `http://www.sternwarte.uni-erlangen.de/Arbeiten/2011-12_Fuerst.pdf`
Gallo L.C., Miniutti G., Miller J.M., et al., 2011, MNRAS 411, 607
Gallo L.C., Tanaka Y., Boller T., et al., 2004, MNRAS 353, 1064
García J., Dauser T., Lohfink A., et al., 2014, ApJ 782, 76
García J., Dauser T., Reynolds C.S., et al., 2013, ApJ 768, 146
García J., Kallman T.R., 2010, ApJ 718, 695
García J., Kallman T.R., Mushotzky R.F., 2011, ApJ 731, 131
Garofalo D., 2009, ApJ 699, 400
Garofalo D., Evans D.A., Sambruna R.M., 2010, MNRAS 406, 975
Ghisellini G., Haardt F., Matt G., 1994, MNRAS 267, 743
Ghisellini G., Haardt F., Matt G., 2004, A&A 413, 535
Gierliński M., Done C., 2004, MNRAS 349, L7
Giles A.B., Jahoda K., Swank J.H., Zhang W., 1995, Publ. Astron. Soc. of Australia 12, 219
Gou L., McClintock J.E., Reid M.J., et al., 2011, ApJ 742, 85
Grinberg V., Hell N., Pottschmidt K., et al., 2013, A&A 554, A88
Guainazzi M., Bianchi S., Dovčiak M., 2006, Astron. Nachr. 327, 1032
Haardt F., 1993, ApJ 413, 680
Hanke M., 2011, Ph.D. thesis, University of Erlangen-Nuremberg, available online at `http://www.sternwarte.uni-erlangen.de/Arbeiten/2011-04_Hanke.pdf`
Hanke M., Wilms J., Nowak M.A., et al., 2009, ApJ 690, 330
Houck J.C., 2002, In: Branduardi-Raymont G. (ed.) High Resolution X-ray Spectroscopy with XMM-Newton and Chandra.
Houck J.C., Denicola L.A., 2000, In: Manset N., Veillet C., Crabtree D. (eds.) Astronomical Data Analysis Software and Systems IX. ASP Conf. Ser. 216, p. 591
Hubeny I., Blaes O., Krolik J.H., Agol E., 2001, ApJ 559, 680
Hughes S.A., Blandford R.D., 2003, Astrophys. J., Lett. 585, L101
Jahoda K., Markwardt C.B., Radeva Y., et al., 2006, apjs 163, 401
Jansen F., Lumb D., Altieri B., et al., 2001, A&A 365, L1
Jones D.H., Read M.A., Saunders W., et al., 2009, MNRAS 399, 683
Kalberla P.M.W., Burton W.B., Hartmann D., et al., 2005, A&A 440, 775
Kara E., Fabian A.C., Cackett E.M., et al., 2013, MNRAS 428, 2795
Kendziorra E., Wilms J., Haberl F., et al., 2004, In: G. Hasinger & M. J. L. Turner (ed.) Society of Photo-Optical Instrumentation Engineers (SPIE) Conference Series, Vol. 5488., p.613
Kerr R.P., 1963, Phys. Rev. Lett. 11, 237
King A.R., Pringle J.E., Hofmann J.A., 2008, MNRAS 385, 1621
Kolehmainen M., Done C., Díaz Trigo M., 2011, MNRAS 416, 311
Kormendy J., Ho L.C., 2013, ARA&A 51, 511
Krolik J.H., 1999, Active Galactic Nuclei: From the Central Black Hole to the Galactic Environment, Princeton Univ. Press, Princeton, NJ
Krolik J.H., McKee C.F., Tarter C.B., 1981, ApJ 249, 422
Kurosawa R., Proga D., 2009, MNRAS 397, 1791
La Mura G., Ciroi S., Cracco V., et al., 2011, In: Foschini L., Colpi M., Gallo L., Grupe D., Komossa S., Leighly K., Mathur S. (eds.) Narrow-Line Seyfert 1

Galaxies and their Place in the Universe. Proceedings of Science (NLS1), p. 056
Laor A., 1991, ApJ 376, 90
Lebrun F., Leray J.P., Lavocat P., et al., 2003, A&A 411, L141
Leighly K.M., 1999, ApJS 125, 297
Li L.X., Zimmerman E.R., Narayan R., McClintock J.E., 2005, ApJS 157, 335
Lightman A.P., Lamb D.Q., Rybicki G.B., 1981, ApJ 248, 738
Lightman A.P., Rybicki G.B., 1980, ApJ 236, 928
Longinotti A.L., de La Calle I., Bianchi S., et al., 2008, Mem. Soc. Astron. Ital. 79, 259
Magdziarz P., Zdziarski A.A., 1995, MNRAS 273, 837
Magnani L., Blitz L., Mundy L., 1985, ApJ 295, 402
Maitra D., Markoff S., Brocksopp C., et al., 2009, MNRAS 398, 1638
Makishima K., Maejima Y., Mitsuda K., et al., 1986, ApJ 308, 635
Marconi A., Hunt L.K., 2003, Astrophys. J., Lett. 589, L21
Marinucci A., Matt G., Miniutti G., et al., 2014, ApJ in press (arXiv:1404.3561)
Markoff S., Nowak M.A., 2004, ApJ 609, 972
Markoff S., Nowak M.A., Wilms J., 2005, ApJ 635, 1203
Markowitz A.G., Reeves J.N., 2009, ApJ 705, 496
Marscher A.P., Jorstad S.G., Gómez J.L., et al., 2002, Nat 417, 625
Martocchia A., Karas V., Matt G., 2000, MNRAS 312, 817
Martocchia A., Matt G., 1996, MNRAS 282, L53
Martocchia A., Matt G., Karas V., 2002, A&A 383, L23
Matt G., Perola G.C., 1992, MNRAS 259, 433
Matt G., Perola G.C., Piro L., 1991, A&A 247, 25
Matt G., Perola G.C., Piro L., Stella L., 1992, A&A 257, 63
McClintock J., Remillard R.A., 2006, Black Hole Binaries. In: Lewin W.H.G., van der Klis M. (eds.) Compact Stellar X-ray Sources. Cambridge Univ. Press, Cambridge, p.157
McClintock J.E., Narayan R., Gou L., et al., 2010, In: Comastri A., Angelini L., Cappi M. (eds.) X-Ray Astronomy 2009: Present Status, Multi-Wavelength Approach and Future Perspectives, AIP Conf. Ser. 1248., Melville, NY: AIP, p.101
McKinney J.C., 2006, MNRAS 368, 1561
Miller J.M., Fabian A.C., Wijnands R., et al., 2002, ApJ 570, L69
Miller J.M., Parker M.L., Fuerst F., et al., 2013a, Astrophys. J., Lett. 779, L2
Miller J.M., Parker M.L., Fuerst F., et al., 2013b, Astrophys. J., Lett. 775, L45
Miller J.M., Pooley G.G., Fabian A.C., et al., 2012, ApJ 757, 11
Miller J.M., Reynolds C.S., Fabian A.C., et al., 2008, ApJ 679, L113
Miniutti G., 2006, Astron. Nachr. 327, 969
Miniutti G., Fabian A.C., 2004, MNRAS 349, 1435
Miniutti G., Fabian A.C., Anabuki N., et al., 2007, PASJ 59, 315
Miniutti G., Fabian A.C., Goyder R., Lasenby A.N., 2003, MNRAS 344, L22
Mirabel I.F., Rodríguez L.F., 1994, Nat 371, 46
Mitsuda K., Inoue H., Koyama K., et al., 1984, PASJ 36, 741
Miškovičová I., Hell N., Hanke M., et al., 2014, A&A submitted
Moderski R., Sikora M., Lasota J.P., 1998, MNRAS 301, 142
Müller C., 2014, Ph.D. thesis, University of Erlangen-Nuremberg, available online at `http://www.sternwarte.uni-erlangen.de/Arbeiten/index.cgi`
Murdin P., Webster B.L., 1971, Nat 233
Mushotzky R.F., Done C., Pounds K.A., 1993, ARA&A 31, 717
Mushotzky R.F., Fabian A.C., Iwasawa K., et al., 1995, MNRAS 272, L9
Nandra K., Barret D., Barcons X., et al., 2013, ArXiv arXiv:1306.2307
Nandra K., O'Neill P.M., George I.M., Reeves J.N., 2007, MNRAS 382, 194
Nandra K., Pounds K.A., Stewart G.C., et al., 1989, MNRAS 236, 39P
Narayan R., McClintock J.E., 2012, MNRAS 419, L69
Nardini E., Fabian A.C., Reis R.C., Walton D.J., 2011, MNRAS 410
Nowak M.A., Hanke M., Trowbridge S.N., et al., 2011, ApJ 728, 13
Nowak M.A., Wilms J., Dove J.B., 2002, MNRAS 332, 856
Orito S., Yoshimura M., 1985, Physical Review Letters 54, 2457
Orosz J.A., McClintock J.E., Aufdenberg J.P., et al., 2011, ApJ 742, 84
Patrick A.R., Reeves J.N., Porquet D., et al., 2012, MNRAS 426, 2522
Patrick A.R., Reeves J.N., Porquet D., et al., 2011, MNRAS 411, 2353
Perley R.A., Dreher J.W., Cowan J.J., 1984, Astrophys. J., Lett. 285, L35
Piconcelli E., Jimenez-Bailón E., Guainazzi M., et al., 2005, A&A 432, 15
Ponti G., Gallo L.C., Fabian A.C., et al., 2010, MNRAS 406, 2591
Pounds K.A., King A.R., Page K.L., O'Brien P.T., 2003, MNRAS 346, 1025
Pounds K.A., Nandra K., Stewart G.C., et al., 1990,

Nat 344, 132
Poutanen J., 2002, MNRAS 332, 257
Pringle J.E., 1996, MNRAS 281, 357
Proga D., Stone J.M., Kallman T.R., 2000, ApJ 543, 686
Reis R.C., Fabian A.C., Ross R.R., et al., 2008, MNRAS 387, 1489
Reynolds C.S., 2013, Classical and Quantum Gravity 30, 244004
Reynolds C.S., Fabian A.C., 1997, MNRAS 290, L1
Reynolds C.S., Fabian A.C., Nandra K., et al., 1995, MNRAS 277, 901
Reynolds C.S., Nowak M.A., 2003, Phys. Rep. 377, 389
Reynolds C.S., Young A.J., Begelman M.C., Fabian A.C., 1999, ApJ 514, 164
Risaliti G., Harrison F.A., Madsen K.K., et al., 2013, Nat 494, 449
Ross R.R., Fabian A.C., 2005, MNRAS 358, 211
Ross R.R., Fabian A.C., 2007, MNRAS 381, 1697
Ross R.R., Fabian A.C., Young A.J., 1999, MNRAS 306, 461
Rothschild R.E., Blanco P.R., Gruber D.E., et al., 1998, ApJ 496, 538
Russell D.M., Fender R.P., Gallo E., Kaiser C.R., 2007, MNRAS 376, 1341
Ruszkowski M., 2000, MNRAS 315, 1
Sani E., Lutz D., Risaliti G., et al., 2010, MNRAS 403, 1246
Schartel N., Rodríguez-Pascual P.M., Santos-Lleó M., et al., 2007, A&A 474, 431
Schurch N.J., Done C., Proga D., 2009, ApJ 694, 1
Schwarzschild K., 1916, Abh. Konigl. Preuss. Akad. Wissenschaften Jahre 1906,92, Berlin,1907 189–196
Shakura N.I., Sunyaev R.A., 1973, A&A 24, 337
Shemmer O., Netzer H., 2002, Astrophys. J., Lett. 567, L19
Sim S.A., Proga D., Miller L., et al., 2010, MNRAS 408, 1396
Speith R., Riffert H., Ruder H., 1995, Comp. Phys. Commun. 88, 109
Stella L., 1990, Nat 344, 747
Strüder L., Briel U., Dennerl K., et al., 2001, A&A 365, L18
Suebsuwong T., Malzac J., Jourdain E., Marcowith A., 2006, A&A 453, 773
Sun W.H., Malkan M.A., 1989, ApJ 346, 68
Svoboda J., Dovčiak M., Goosmann R., Karas V., 2009, A&A 507, 1
Svoboda J., Dovčiak M., Goosmann R.W., et al., 2012, A&A 545, A106
Svoboda J., Guainazzi M., Karas V., 2010, A&A 512, A62
Tanaka Y., Boller T., Gallo L., et al., 2004, PASJ 56, L9
Tanaka Y., Nandra K., Fabian A.C., et al., 1995, Nat 375, 659
Tarter C.B., Tucker W.H., Salpeter E.E., 1969, ApJ 156, 943
Theureau G., Coudreau N., Hallet N., et al., 2005, A&A 430, 373
Thorne K.S., 1974, ApJ 191, 507
Tombesi F., Cappi M., Reeves J.N., et al., 2010, A&A 521, A57
Tombesi F., Sambruna R.M., Marscher A.P., et al., 2012, MNRAS 424, 754
Tomsick J.A., Kalemci E., Kaaret P., et al., 2008, ApJ 680, 593
Tomsick J.A., Nowak M.A., Parker M., et al., 2014, ApJ 780, 78
Torres Del Castillo G.F., Pérez Sánchez C.I., 2006, Revista Mexicana de Fisica 52, 70
Turner T.J., George I.M., Nandra K., Turcan D., 1999, ApJ 524, 667
Turner T.J., Kraemer S.B., Reeves J.N., 2004, ApJ 603, 62
Uttley P., Wilkinson T., Cassatella P., et al., 2011, MNRAS 414, L60
Vaughan S., Fabian A.C., 2004, MNRAS 348, 1415
Vaughan S., Fabian A.C., Ballantyne D.R., et al., 2004, MNRAS 351, 193
Vaughan S., Reeves J., Warwick R., Edelson R., 1999, MNRAS 309, 113
Volonteri M., Madau P., Quataert E., Rees M.J., 2005, ApJ 620, 69
Walton D.J., Nardini E., Fabian A.C., et al., 2013, MNRAS 428, 2901
Wang J.M., Chen Y.M., Ho L.C., McLure R.J., 2006, Astrophys. J., Lett. 642, L111
Weaver K.A., Mushotzky R.F., Arnaud K.A., et al., 1992, Astrophys. J., Lett. 401, L11
Webster B.L., Murdin P., 1972, Nat 235, 37
Wilkins D.R., Fabian A.C., 2011, MNRAS 414, 1269
Wilkins D.R., Fabian A.C., 2012, MNRAS 424, 1284
Wilms J., Allen A., McCray R., 2000, ApJ 542, 914
Wilms J., Pottschmidt K., Pooley G.G., et al., 2007, ApJ 663, L97
Wilms J., Reynolds C.S., Begelman M.C., et al., 2001, MNRAS 328, L27
Wilson A.S., Colbert E.J.M., 1995, ApJ 438, 62
Winkler C., Courvoisier T.J.L., Di Cocco G., et al., 2003, A&A 411, L1
Zdziarski A.A., Skinner G.K., Pooley G.G., Lubiński P., 2011, MNRAS 416, 1324
Zhang S.N., Cui W., Chen W., 1997, Astrophys. J., Lett. 482, L155
Zoghbi A., Fabian A.C., 2011, MNRAS 418, 2642
Zoghbi A., Fabian A.C., Reynolds C.S., Cackett E.M., 2012, MNRAS 422, 129
Zoghbi A., Fabian A.C., Uttley P., et al., 2010, MNRAS 401, 2419

APPENDIX A

THE RELLINE MODEL FAMILY

All models of the `relline` family (Dauser et al., 2010, 2013) are available as "Line Models" and "Convolution Models". Line models produce the relativistically smeared profile of a delta function line at the given energy. The convolution models is capable in applying the relativistic smearing to a complete spectrum. Generally, line models have the word "line" in their names, while the name of convolution type models contains "conv". Moreover there is a third class of models, called `relxill`, which directly combines the relativistics with an intrinsic reflection spectrum (see Chapter 4). This reflection is calculated by the `xillver` code (García & Kallman, 2010; García et al., 2011, 2013). The meaning of the different model parameters can be found in Table A.1. The code of all the models described in the following can be downloaded at `http://www.sternwarte.uni-erlangen.de/research/relxill/`.

The new `relxill` model depicts the most advanced model in this family. As has been extensively discussed in this thesis, using the `relxill` only has advantages over the previous approach of relativistically convolving a reflection model. In the data analysis section (Chapter 3) the strong requirement of fitting a complete reflection spectrum instead of only a single broad lines was also shown. Therefore, the standard approach should be to use the `relxill` or `relxilllp` model for analyzing relativistic reflection. Additionally, models including an ionization gradient in the accretion disk are presented as well.

LINE MODELS

`relline` The most basic form of the model. The emissivity is modeled by an empirical power law.

`relline_lp` Instead of using an empirical emissivity law, the emissivity is calculated directly in the lamp post geometry (see Dauser et al., 2013). This geometry assumes an irradiation of the accretion disk by isotropically radiating source at height h above the black hole, situated on its rotational axis.

`relline_lp_ext` The "extended" version of the lamp post geometry allows to model an extended emission region, a moving primary source and even a (constantly) accelerating jet (see Dauser et al., 2013, for more information).

CONVOLUTION MODELS

`relconv` Convolution Model for `relline` (see Sect. A).

relconv_lp Convolution Model for relline_lp (see Sect. A).

relconv_lp_ext Convolution Model for relline_lp_ext (see Sect. A).

COMBINED MODELS

relxill Combining the relline and the xillver model: In principle this implementation is a simple convolution of relconv*xillver. However, the emission angle dependent spectrum for each emitting point on the accretion disk is properly taken into account, which makes any empirical limb-darkening/-brightening obsolete.

relxilllp Similar to relxill, but now for the lamp post geometry, i.e., relconv_lp is used for the convolution in this case.

relxill_ion This model works similar to relxill. However, it simulates reflection from the disk with several zones of different ionization. The number of the zones and the ionization gradient can be specified directly in the model.

relxilllp_alpha Similar to relxill, however, for the lamp post geometry. This implies that besides the relativistic smearing, also the ionization gradient is now calculated self-consistently from the irradiation of the disk (using a certain mass accretion rate $\dot{m}$), assuming the density profile of an α accretion disk (see Shakura & Sunyaev, 1973)

relxilllp_ion Like relxill_alpha, but not using a specific density profile. Instead, the density index κ of the power law shaped density profile ($\rho(r) \propto r^{-\kappa}$) can be directly fitted to the data.

The combined models including an ionization gradient include the parameter nzones (see Table A.1), which specifies the number of zones used for the calculations. As can be easily seen from the plotted spectra (Fig. 5.4), usually the spectra for different zones largely differ. Therefore a sufficient number of zones is necessary to reliably predict. However, also the computing time increases linearly with the number of zones as well. A recommended approach is therefore to start modeling with a lower number of zones and then increase this number when the best fit is found.

NON-RELATIVISTIC REFLECTION MODEL

xillver In order to also allow non-relativistic and provide an identical interface, the xillver table model (see http://hea-www.cfa.harvard.edu/~javier/xillver/) is included in the relline modeling package. Besides the normal parameters of the table, the reflection fraction is also included as a fitting parameter (similar to the pexrav reflection model).

Tab. A.1.: *Table of all parameters used in the different implementations of the* `relline` *model, as explained in the text.*

Name	Description
linieE	line energy in the rest frame of the disk
Index1	emissivity index for r < Rbr, where emissivity is $r^{-\mathrm{Index1}}$
Index2	emissivity index for r > Rbr, where emissivity is $r^{-\mathrm{Index2}}$
Rbr	radius where emissivity changes from Index1 to Index2
a	Spin of the Object
Incl	inclination angle measured with respect to the normal of the disk
Rin	inner radius of the disk
Rout	outer radius of the disk
z	redshift to the source
limb	limb-darkening/-brightening law for $\mu = \cos(\delta)$:
	0 = isotropic, 1 = darkening $(1 + 2.06\mu)$, 2 = brightening $(\ln(1 + 1/\mu))$
gamma	Power Law Index of the primary source $(E^{-\mathrm{gamma}})$
h	height of the primary source
hbase	lower height of a radially extended primary source
htop	upper height of a radially extended primary source
vbase	velocity of the source at hbase
v100	velocity of the source at 100 r_g above hbase
logxi	logarithmic value of the ionization parameter at the inner edge of the disk
Afe	Iron Abundance in Solar Units
ion_index	ionization gradient index of the accretion disk $(\log\xi \propto r^{-\mathrm{ion\_index}})$
mdot	mass accretion rate (lamp post irradiation)
nzones	number of zones of different ionization
refl_frac	reflection fraction as defined in Eq. 4.2; calculated between 20 and 40 keV
fixReflFrac	0: free reflection fraction (determined by the refl_frac parameter)
	1: fix reflection fraction to the lamp post value
	2: free, (same as 0:), but now the reflection fraction is displayed on the screen

ACKNOWLEDGMENTS

ACKNOWLEDGMENTS

First of all I would like to thank my adviser and "Doktorvater" Jörn Wilms for providing me with the topic of this thesis and therefore giving me the possibility to contribute scientifically to the field of X-ray astronomy and black holes. His frequent and excellent advise made the numerous results and publications possible. Moreover I would like to thank him for his large effort to get funding that allowed me to travel to various international conferences and meetings to present my results and start new collaborations. As head of the X-ray group of the Remeis observatory in Bamberg he also managed to create a fruitful and pleasant working atmosphere.

The Dr. Karl Remeis observatory in Bamberg has a very pleasant and joyful working atmosphere due to all the people working there. I would therefore generally like to thank everybody for this ambiance, which always greatly supported me in my work. All my office mates, Manfred Hanke and Moritz Böck in the early times and later Maria Hirsch and Sebastian Falkner, created always a very nice atmosphere and I would like to thank them for countless useful and also funny conversations. Manfred and Moritz always gave general advise, asked critical questions, and helped in solving programming related issues, even long after they left the observatory. I also want to thank Sebastian Falkner for his work on ray tracing around neutron stars under my supervision. The discussions with him about the application of the ray tracing techniques for neutron stars also greatly improved my own knowledge. Special thanks go to Refiz Duro, as the complete analysis of Cygnus X-1 was done together in a very pleasant and productive atmosphere with him. I would also like to thank Tobias Beuchert, Cornelia Müller, Alex Markowitz, and Felicia Krauß for the collaborative work on AGN and multi-wavelength astronomy. Great thanks also to my system administrator colleagues, Fritz Schwarm and Ingo Kreykenbohm, for helping with any computer problems and keeping the local cluster running properly. I also want to thank the astronomy institute in Würzburg for providing me with an office and also a very friendly working atmosphere whenever I needed to work there. I would also like to thank Moritz Böck and Rosamunde Pare for reading parts of this thesis and therefore improving it.

I would like to thank all my co-authors of my publications for the fruitful collaboration and their numerous comments and ideas. Being my main collaborator over the last years, I would especially like to Javier García for the endless amount of very fruitful discussions by mail, phone, and in person. This interaction led to a significant amount of scientific output in from of several publications and the successful fitting model `relxill`. Most of the presented results in this thesis were obtained in this collaboration. Moreover I am really thankful that he realized my very productive and pleasant stay for two weeks in Boston at the CfA Harvard.

Besides my main collaborator, there are many people who greatly contributed to the results presented in this thesis. First of all, I would like to thank Christopher Reynolds, for his initial ideas that led to the topic of this thesis and his valuable ideas on various issues during the last years. I am also grateful for the fruitful collaboration with Andrew Fabian and his valuable scientific advise. Also great thanks to Michael Parker for his great ideas and data analysis simulations regarding the reflection fraction. Moreover I want to thank Guido Risaliti for various discussions about relativistic reflection and data analysis, also regarding newest *NuSTAR* results. Concerning the work on `relxill` and the reflection fraction, Anne Lohfink was always present with advise regarding ob-

servational facts and simulating and analyzing X-ray data. Many thanks go to Norbert Schartel, who greatly helped by extracting and analyzing the *XMM-Newton* data of 1H0707−495 and Jiří Svoboda for the collaboration on the 1H0707−495 data analysis. Moreover I would like to thank him, Michal Dovčiak, and Vladimir Karas for making my stay at the Prague institute for Astronomy possible and the excellent discussions on modeling relativistic reflection. I also greatly appreciate the collaboration with Maurizio Falanga and his great advice concerning general relativistic light-bending. Moreover I want to thank him for making the productive stays at ISSI in Bern possible and I also acknowledge direct support from ISSI. Last but not least, I would like to thank all users of the `relline` and `relxill` model for applying the model and I am grateful for all the feedback and suggestions I received concerning these models.

I acknowledge support by a fellowship from the Elitenetzwerk Bayern, by the Deutsches Zentrum für Luft- und Raumfahrt under contract number 50 OR 1113, and for partial support from the European Commission under contract ITN 215212 "Black Hole Universe". I would like to thank John E. Davis for the development of the SLXFIG module used to prepare all figures in this thesis. This research has made use of ISIS functions provided by ECAP/Remeis observatory and MIT (`http://www.sternwarte.uni-erlangen.de/isis/`). This work is based on observations obtained with *XMM-Newton*, an ESA science mission with instruments and contributions directly funded by ESA Member States and NASA. Also the Astrophysics Data System (ADS) of SAO/NASA was used often for this thesis.